NASA/TM-2001-210935

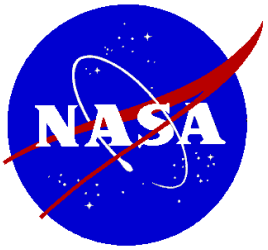

Mars Transportation Environment Definition Document

M. Alexander, Editor
Marshall Space Flight Center, Marshall Space Flight Center, Alabama

March 2001

NASA/TM-2001-210935

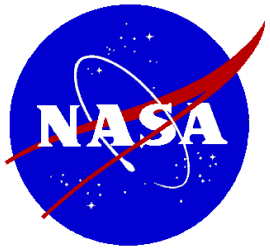

Mars Transportation Environment Definition Document

M. Alexander, Editor
Marshall Space Flight Center, Marshall Space Flight Center, Alabama

National Aeronautics and Space Administration

Marshall Space Flight Center · Marshall Space Flight Center, Alabama

March 2001

Preface

"A day on Mars is a little longer than a day on Earth: 24 hours and 40 minutes. A year on Mars is less than two Earth years: 686 Earth days, or 668 Martian days. Mars is 6,787 kilometers in diameter, compared to Earth's 12,756 kilometers. Its gravitational acceleration is 3.71 meters per second squared, or just over one-third of Earth's. The atmospheric pressure at the surface of Mars averages 5.6 millibars, about one-half of one percent of Earth's. The atmosphere is largely composed of carbon dioxide. Temperatures at "datum" or reference surface level (there is no "sea level", as there are presently no seas) vary from -130° to +27° Celsius. An unprotected human on the surface of Mars would very likely freeze within minutes, but first would die of exposure to the near-vacuum. If this unfortunate human survived freezing and low pressure, and found a supply of oxygen to breathe" [and water to drink], "she would still be endangered by high levels of radiation from the sun and elsewhere.

"After Earth, Mars is the most hospitable planet in the Solar System."

- Greg Bear, Moving Mars, Tom Doherty Associates, New York, 1993

Acknowledgments

The compilers of this technical memorandum wish to thank Mr. William L. Eoff, of the NASA Marshall Space Flight Center, Space Transportation Directorate, Advanced Concepts Department, Exploration Transportation Team, for his support and encouragement in the preparation of the document. The compilers also wish to thank Mr. William J. Kauffman, Jr. of the NASA Space Environments and Effects Program for partial support to develop sections 2 and 4.

Contributors

NASA Jet Propulsion Laboratory

Robin Evans (MS 183-900)	robin.evans@jpl.nasa.gov
Dr. Henry B. Garrett (MS 301-456)	henry.garrett@jpl.nasa.gov
Dr. Matthew P. Golombek (MS 183-501)	matt.golombek@jpl.nasa.gov

NASA Langley Research Center

Dr. John Wilson (MS 188B)	john.w.wilson@larc.nasa.gov

NASA Marshall Space Flight Center

Margaret Alexander (ED44)	margaret.alexander@msfc.nasa.gov
Dr. William Cooke (ED44/CSC)	bill.cooke@msfc.nasa.gov
Belinda Hardin (ED44/CSC)	belinda.hardin@msfc.nasa.gov
Bonnie James (TD15)	bonnie.james@msfc.nasa.gov
Dale Johnson (ED44)	dale.johnson@msfc.nasa.gov
Dr. C. G. Justus (ED44/CSC)	jere.justus@msfc.nasa.gov
Dr. Rob Suggs (ED44)	rob.suggs@msfc.nasa.gov
Lisa Tyree (ED44/CSC)	lisa.tyree@msfc.nasa.gov

Table of Contents

Table of Contents (continued)

Table of Contents (concluded)

List of Illustrations

List of Illustrations (continued)

List of Illustrations (concluded)

List of Tables

List of Tables (concluded)

Acronyms

ASI	Atmospheric Structure Investigation
AU	Astronomical Unit
CME	Coronal Mass Ejection
CRC	Chemical Rubber Company
EUV	Extreme Ultraviolet
GCR	Galactic Cosmic Rays
IRTM	Infrared Thermal Mapper
JPL	Jet Propulsion Laboratory
LET	Linear Energy Transfer
LMT	Local Mars Time
MAE	Materials Adherence Experiment
Mars-GRAM	Mars Global Reference Atmospheric Model
MGS	Mars Global Surveyor
MIEL	Man-Ionizing Energy Loss
MOLA	Mars Orbiter Laser Altimeter
MPF	Mars Pathfinder
MSFC	Marshall Space Flight Center
NASA	National Aeronautics and Space Administration
PDF	portable data format
RDM	Radiation Design Margin
SEE	Single Event Effects
SMM/ACRIM	Solar Maximum Mission/Active Cavity Radiometer Irradiance Monitor
SNC	Shergottite, nakhlite and chassignite
SPE	Solar Proton Events
TEPC	Tissue Equivalent Proportional Counter
TES	Thermal Emission Spectrometer
TID	Total Ionizing Dose
UAMS	Upper Atmosphere Mass Spectrometer
US	United States
UV	Ultraviolet
VL	Viking Lander

MARS TRANSPORTATION ENVIRONMENT DEFINITION DOCUMENT

1.0 INTRODUCTION

1.1 Background

This document, prepared for the NASA Marshall Space Flight Center (MSFC) Transportation Directorate, Exploration Transportation Office, is an engineering reference for applications in both robotic and human Mars missions. It provides the current state of knowledge of environmental factors important to engineering design, development, and operations. The information updates earlier work[1-1] and incorporates results from recent Mars robotic missions. Development of this document, coordinated by the NASA Marshall Space Flight Center Environments Group, is a collaborative effort of scientists and engineers within MSFC, other NASA Centers, aerospace industry, and academia.

1.2 Purpose

The purpose of this document is to provide in one reference source discussions of (and values for) many of the parameters of Mars environments important in systems design, mission planning, and spacecraft operations. This report is not intended to replace detailed environmental specifications in environments requirements documents for specific Mars missions. Any engineer or designer who needs more detailed information, is encouraged to contact one or more of the contributors listed previously. This document is a supplement to the Human Exploration of Mars Reference Mission document,[1-2] [1-3] which provides the technical community with baseline reference Mars mission architectures.

1.3 Mars-Earth Comparisons

1.3.1 Introduction

The environment of Mars has both similarities to and contrasts with Earth's environment. Comparisons of some environmental values between Earth and Mars are given in table 1-1. More detailed Mars environmental data values are also given in appendices A and B.

1.3.2 Orbit and Climate

Mars' day length, 24 hours 37 minutes, is only slightly longer than Earth's. Mars' obliquity angle is 25.2 degrees, thus, sub-solar latitudes on Mars vary over almost the same range as on Earth and (in relative terms) the range of seasonal variations are about the same as Earth's. Like Earth, Mars is closer to the Sun in its Southern Hemisphere summer, with perihelion coming shortly before southern summer solstice. Because of the larger orbital eccentricity of Mars, however, its southern summer is warmer relative to its northern summer than Earth's. With a year length of 687 Earth days (669 Mars solar days, or sols) the seasons on Mars are about twice as long as on Earth. Seasons on Mars are measured by an angle (usually denoted L_s) that measures celestial longitude of the Sun as seen from Mars. Northern Hemisphere seasons on Mars begin at L_s=0º (spring), 90º (summer), 180º (fall), and 270º (winter). Because of orbital eccentricity, seasons on Mars are not an equal number of days (sols) (see section 3.1.1). Its low concentration of atmospheric water vapor (about 300 parts per million) makes Mars a desert

planet. With no liquid water presently on its surface, Mars has about the same land area as Earth, despite its small size (planetary radius 3390 km, about half that of Earth). Since Mars' distance from the Sun averages over 1.5 times that of Earth, Mars receives only about 43 percent as much direct sunlight as Earth. With Mars' larger orbital eccentricity the sunlight it receives varies more during the course of its year (493 to 716 W/m^2 for Mars; compared to 1322 to 1414 W/m^2 for Earth).

1.3.3 Dust Storms

A frequent feature of the Mars surface and atmospheric environment is the presence of dust storms. These clouds of dust, sometimes raised to 80-km levels in the atmosphere (see section 3.5.1), may be local (up to 100 km or so), regional (up to 1000 km or so), or fully global in size and area affected. One measure of the intensity of a Martian dust storm is its optical depth (frequently referred to as τ, or tau), which is a measure of the attenuation of a beam of sunlight as it passes through the entire (dust-obscured) atmosphere. If a dust storm tau value exceeds about one, the surface would still receive daytime sunlight through the hazy dust layer(s), but a surface-based observer would be unable to see a clearly-defined edge to the apparent disk of the Sun though the "overcast". Clouds of ice (frozen particles of water or carbon dioxide) can also obscure sunlight and contribute to the atmospheric optical depth.

Table 1-1. Comparison of Mars with Earth

Parameter	Mars	Earth
Distance from Sun	1.52 AU	1.00 AU
Length of Day	24 hr 37 min (1 sol)	24 hr
Axis Tilt w.r.t. Orbit	25.2 degrees	23.5 degrees
Length of Year	687 days (669 sols)	365 days
Mean Planetary Radius	3390 km	6378 km
Surface Gravity	3.7 m/s^2	9.8 m/s^2
Relative Surface Area	0.28	1.00
Relative Land Area	0.98	1.00
Average Solar Radiation (*)	589 W/m^2	1367 W/m^2
Atmospheric Pressure at Surface	5 to 10 (6.4 avg.) mb	1013 mb
Average Atmospheric Temperature at Surface	210 K (-80 °F)	288 K (60 °F)
Average Atmospheric Density at Surface	0.016 kg/m^3	1.2 kg/m^3
Atmos. Scale Height	10 km	8 km
Adiabatic Lapse Rate	4.5 K/km	9.8 K/km
Mean Obs. Lapse Rate	2.5 K/km	6.5 K/km
Mean Albedo	0.08 to 0.40 (0.25 avg.)	0.05 to 0.80 (0.30 avg.)
Atmos. Optical Depth	0.1 to 10	0.01 to 3
Atmospheric Species (dry atmosphere)	95% CO_2 3% N_2 2% Ar	78% N_2 21% O_2 1% Ar
Precipitable Water	1 to 80 μm	1 to 50 mm

(*) at top-of-atmosphere

1.3.4 Nominal Density Profiles

Figure 1-1 shows height variation of nominal atmospheric density for Earth and Mars. Because of its lower atmospheric mass (and surface pressure), surface atmospheric density on Mars is about a hundred-fold lower than that for surface atmospheric density on Earth. Because of differences in temperature and density scale height for Mars versus Earth, atmospheric density is roughly equal at about 100-km altitude on both planets. Thus, spacecraft using aerobraking near the 100-km level on Mars encounter roughly the same density as this altitude on Earth. As temperature and scale height differences continue to affect density toward higher altitudes, atmospheric density on Mars returns to about a hundred-fold lower than for Earth at heights of several hundred to 1000 km. By finding heights with equal density values in figure 1-1, it is easy to estimate equivalent-density orbital altitudes between Earth and Mars. For example, a satellite in an 800-km altitude orbit on Earth would experience comparable atmospheric density at about 420-km altitude on Mars.

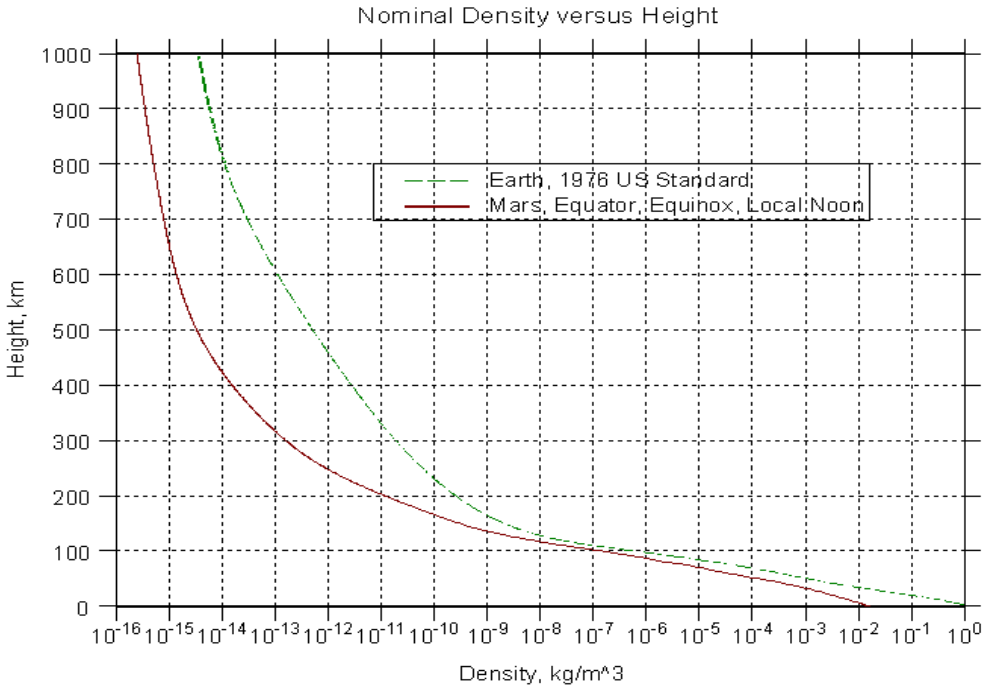

Figure 1-1. Comparison of nominal atmospheric density versus height for Earth and Mars. Earth values are from the 1976 US Standard Atmosphere. Mars values are from Mars-GRAM[1-4] at the Equator during equinox and local noon solar time.

1.4 Overview

Organization of the sections of this report is in the order of environments encountered by Mars mission spacecraft systems (after leaving the environment of Earth). This section provides an introduction and general overview. Section 2 gives details of the interplanetary environment, especially ionizing radiation and meteoroids, encountered on Mars-Earth (and Earth-Mars) transit. Section 3 provides information on the atmosphere of Mars, specifically relevant for aerocapture, aerobraking, precision landing, and/or surface operations. Details of the impact of dust storms on Mars' atmospheric environment are provided in this section. Section 4 details the

Mars surface environment, particularly as relevant to operation of surface systems such as landers and rovers and discusses ionizing radiation environment at the surface. References are provided at the end of each section.

1.5 References

1-1. Kaplan, D. L., compiler: “Environment of Mars, 1988”, NASA Technical Memorandum 100470, 1988.

1-2. Hoffman, S. J. and D. L. Kaplan, editors: "Human Exploration of Mars: The Reference Mission of the NASA Mars Exploration Study Team." NASA SP-6107, 1997.

1-3. Drake, B. G., editor: "Reference Mission Version 3.0 Addendum to the Human Exploration of Mars: The Reference Mission of the NASA Mars Exploration Study Team." NASA/SP-1998-6107/ADD, 1998.

1-4. Justus, C. G.: “Mars Global Reference Atmospheric Model for Mission Planning and Analysis.” *J. Spacecraft and Rockets*, Vol. 28, No. 2, pp. 216-221, 1991.

2.0 INTERPLANETARY SPACE ENVIRONMENT

2.1 Mission Trajectories

This section considers the potentially hazardous environments associated with transfer to and from Mars. This interplanetary space environment is characterized by high energy radiation, space plasmas, and high velocity meteoroids. Radiation is of most concern of the three with plasma interactions the least (and therefore is ignored). Trajectory through the interplanetary environment for a manned Mars mission is divided into four principal intervals: Earth-Mars Transit, Mars Orbit, Mars Surface, and Mars-Earth Return Transit. Although not covered herein because of the many possible Earth launch trajectories, the Earth's trapped radiation belts also contribute to the total radiation background. While debris and charging environments pose a brief threat during departure from the Earth's immediate environment, these environments need to be defined for each particular mission. In this section, the interplanetary radiation and meteoroid environments are defined for Earth-Mars transit, Mars orbit, and Mars-Earth return with surface environments being treated in Section 4.5. A "typical" two-year mission profile with approximately 16 months on Mars has been selected for this analysis. The mission trajectory studied is illustrated in figure 2-1 and key mission dates are listed in table 2-1. The intent is to provide sample engineering environments for design engineers and mission planners and to illustrate the process necessary for defining the mission environmental requirements. In all cases, the final design environments and design margins need to be determined for the specific mission trajectory when known.

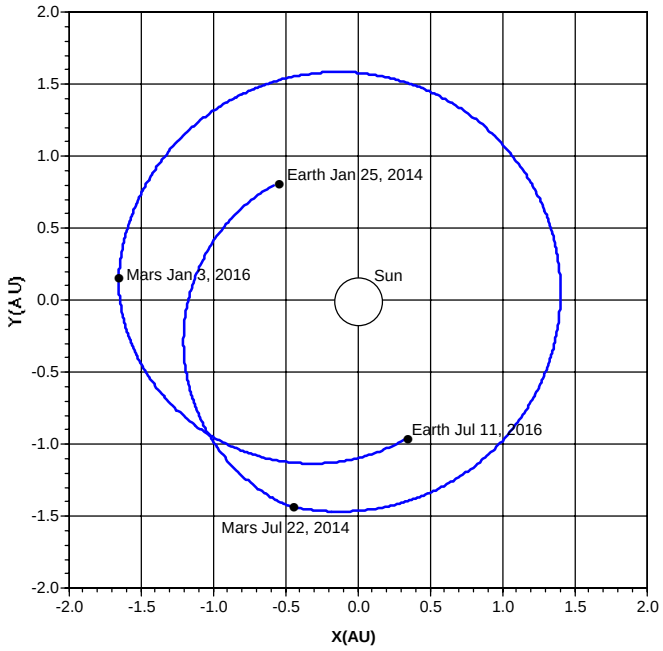

Figure 2-1. Orbits assumed for a Manned Mars Mission starting on 25 January 2014, reaching Mars on 22 July 2014, leaving Mars on 3 January 2016, and arriving back at Earth on 11 July 2016.

Table 2-1. Orbit segments considered for Mars mission study

Orbit Segment	Timeline	Rmin(AU)	Rmax(AU)
1) Earth to Mars Transfer	179 Days	0.984	1.499
Earth Depart Jan 25, 2014			
Mars Arrive Jul 22, 2014			
2) Mars Mission	530 Days	1.384	1.663
Mars Arrive Jul 22, 2014			
Mars Depart Jan 03, 2016			
3) Mars to Earth Transfer	189 Days	1.015	1.653
Mars Depart Jan 03, 2016			
Earth Arrive Jul 11, 2016			
4) Complete mission Earth-Mars-Earth	898 Days	0.984	1.663

2.2 Ionizing Radiation Environment

Aside from on-board nuclear power sources, the major contributors to the Mars radiation environment are the Galactic Cosmic Rays (GCR) and Solar Proton Events (SPE; also commonly referred to as solar flares). These two environments are responsible for radiation damage to electronic systems and are a threat to astronaut health. They include Total Ionizing Dose (TID) effects, Single Event Effects (SEE), Displacement Damage, and Non-Ionizing Energy Loss (NIEL) effects. The environments causing these effects are typically characterized in terms of fluxes as functions of either energy or Linear Energy Transfer (LET) or as TID versus energy. This section presents the appropriate environmental descriptions in these terms. Keep in mind, however, that the environments are highly variable and that it is common for a project or designer to assign a Radiation Design Margin (RDM) to account for uncertainties. Typically, at least a factor of two through factors of four or higher may be appropriate for manned missions.

2.2.1 Solar Proton Event Environment

The primary radiation environment of concern to a Mars mission is solar activity. The principle source of radiation damage is the so-called Solar Proton Event. An SPE is believed to be caused by intense activity at the Sun (currently assumed to be a Coronal Mass Ejection or CME) which results in the acceleration of solar plasma up to 10's to 100's of MeV in energy. These events usually last only a few days but can raise the solar energetic particle flux to many orders of magnitude over background. An event is characterized by proton and heavy ion fluxes as a function of energy over the duration of the event. Recent models[2-2] refine the method for estimating the occurrence of SPE's. A mission estimates the likelihood of a given flux level being observed as a function of the mission's duration versus the solar cycle. The JPL-SPE model breaks up the 11-year solar cycle into 4 inactive and 7 active years. The model in this respect is a step function. The Sun is assumed to be "off" for 4 years and "on" for 7 for producing SPE's. The assumed active period of the Sun in the 11-year solar cycle for the proposed Mars mission presented here is 2010.4 to 2017.4. A manned Mars mission launched Jan. 25, 2014 and returned to Earth July 11, 2016 is completely within this window (note: this is a conservative estimate, thus more appropriate for a manned mission). The sample Mars mission trajectory considered here is broken into the four sub-mission intervals presented earlier. Solar proton fluence and dose are then estimated[2-1 2-2] for the Earth to Mars, Mars orbit, and Mars return portions (radiation on the Martian surface is described in section 4.5). As a conservative estimate, the mission fluence and dose are estimated for a 95 percent case (i.e., 95 percent of the

time the fluence and dose will be less than the values tabulated and 5 percent of the time the fluences may be equal to or larger). The fluences and doses are listed in tables 2-2 and 2-3 for the orbital segments presented in table 2-1. The doses (4π steradians; spherical aluminum shield) are plotted as a function of aluminum shielding thickness in figure 2-2. Note that the JPL-SPE model is statistically based so the segments can not be directly added to give the total mission fluences or doses. Each of these has to be independently estimated because the JPL-SPE model does not give fluences at energies above 60 MeV directly; these are based on a simple extrapolation from lower energies. Again, for a manned mission, an appropriate RDM should be established by the project. Protons are the primary source of dose due to SPEs (electrons and heavy ions ignored). Heavy ions, important in the single event environment (SEE), are discussed in section 2.2.2.

Table 2-2. 95 percent probability SPE fluences for the 3 segments and total mission. Fluences and doses are not additive (i.e., Earth-Mars transfer plus Mars Mission plus Mars-Earth transfer ≠ Complete Mission). NOTE: the JPL-SPE model does not estimate fluences above 60 MeV—these values are extrapolated.

	MISSION SEGMENT			
Proton Energy (MeV)	Earth to Mars Transfer Fluence(cm^{-2})	Mars Mission Fluence(cm^{-2})	Mars to Earth Transfer Fluence(cm^{-2})	Complete mission Fluence(cm^{-2})
9.E-04	2.04E+15	4.05E+15	1.83E+15	7.91E+15
1.E-03	1.74E+15	3.46E+15	1.56E+15	6.74E+15
2.E-03	6.12E+14	1.22E+15	5.51E+14	2.35E+15
5.E-03	1.54E+14	3.07E+14	1.39E+14	5.82E+14
1.E-02	5.43E+13	1.08E+14	4.88E+13	2.03E+14
2.E-02	1.91E+13	3.80E+13	1.72E+13	7.06E+13
5.E-02	4.81E+12	9.58E+12	4.33E+12	1.75E+13
1.E-01	1.70E+12	3.37E+12	1.53E+12	6.09E+12
2.E-01	5.97E+11	1.19E+12	5.38E+11	2.12E+12
5.E-01	1.50E+11	2.99E+11	1.35E+11	5.26E+11
1.E+00	5.30E+10	1.05E+11	4.77E+10	1.83E+11
4.E+00	1.77E+10	3.53E+10	1.60E+10	5.99E+10
1.E+01	6.85E+09	1.36E+10	6.16E+09	2.38E+10
3.E+01	1.88E+09	3.73E+09	1.69E+09	7.09E+09
6.E+01	8.43E+08	1.68E+09	7.59E+08	3.09E+09
5.E+02	7.25E+07	1.46E+08	6.56E+07	2.44E+08
1.E+03	3.25E+07	6.60E+07	2.95E+07	1.06E+08
2.E+03	1.46E+07	2.97E+07	1.32E+07	4.63E+07

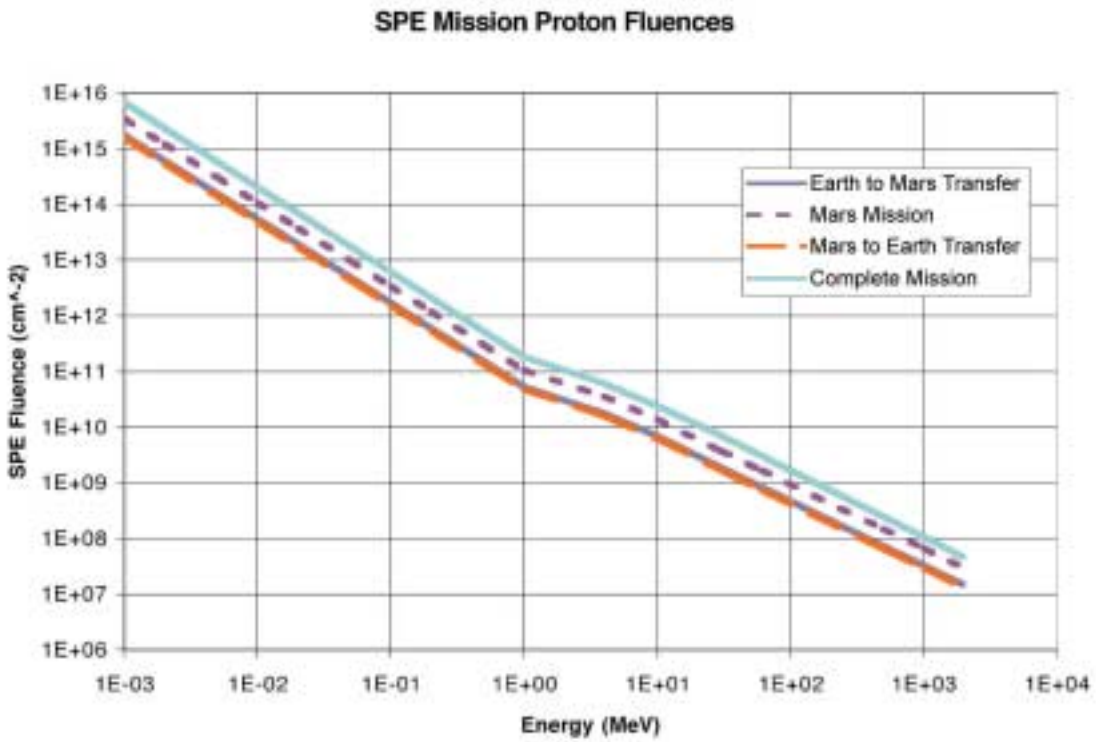

Figure 2-2. 95 percent probability SPE fluences for the 3 segments and total mission. Fluences and doses are not additive (i.e., Earth-Mars transfer + Mars Mission + Mars-Earth transfer ≠ Complete Mission). NOTE: the JPL-SPE model does not estimate fluences above 60 MeV—these values are extrapolated.

Table 2-3. 95 percent probability SPE doses for 3 segments and total mission based on the fluences in Table 2-2. A 4π spherical shield of Aluminum is assumed. Fluences and doses are not additive (i.e., Earth-Mars transfer + Mars Mission + Mars-Earth transfer ≠ Complete Mission).

			MISSION SEGMENT (DOSE IN SPHERE, RADS(Si))			
g/cm^2 (Al)	mils (Al)	mm (Al)	Earth to Mars Transfer	Mars Mission	Mars to Earth Transfer	Complete mission
6.86E-03	1.00E+00	0.0254	7.31E+04	1.45E+05	6.58E+04	2.53E+05
2.06E-02	3.00E+00	0.0762	2.84E+04	5.64E+04	2.56E+04	9.64E+04
5.49E-02	8.00E+00	0.127	1.23E+04	2.46E+04	1.12E+04	4.12E+04
6.86E-02	1.00E+01	0.254	9.70E+03	1.93E+04	8.77E+03	3.26E+04
2.06E-01	3.00E+01	0.762	3.30E+03	6.55E+03	2.97E+03	1.12E+04
5.49E-01	8.00E+01	1.27	1.13E+03	2.24E+03	1.02E+03	4.02E+03
6.86E-01	1.00E+02	2.54	8.82E+02	1.75E+03	7.93E+02	3.18E+03
2.06E+00	3.00E+02	7.62	2.64E+02	5.23E+02	2.37E+02	1.00E+03
3.43E+00	5.00E+02	12.7	1.52E+02	3.01E+02	1.37E+02	5.70E+02
5.49E+00	8.00E+02	20.3	9.47E+01	1.88E+02	8.52E+01	3.52E+02
6.86E+00	1.00E+03	25.4	7.22E+01	1.44E+02	6.50E+01	2.66E+02
1.03E+01	1.50E+03	38.1	4.72E+01	9.42E+01	4.25E+01	1.73E+02
1.37E+01	2.00E+03	50.8	3.56E+01	7.11E+01	3.21E+01	1.29E+02
2.06E+01	3.00E+03	76.2	2.33E+01	4.65E+01	2.10E+01	8.36E+01

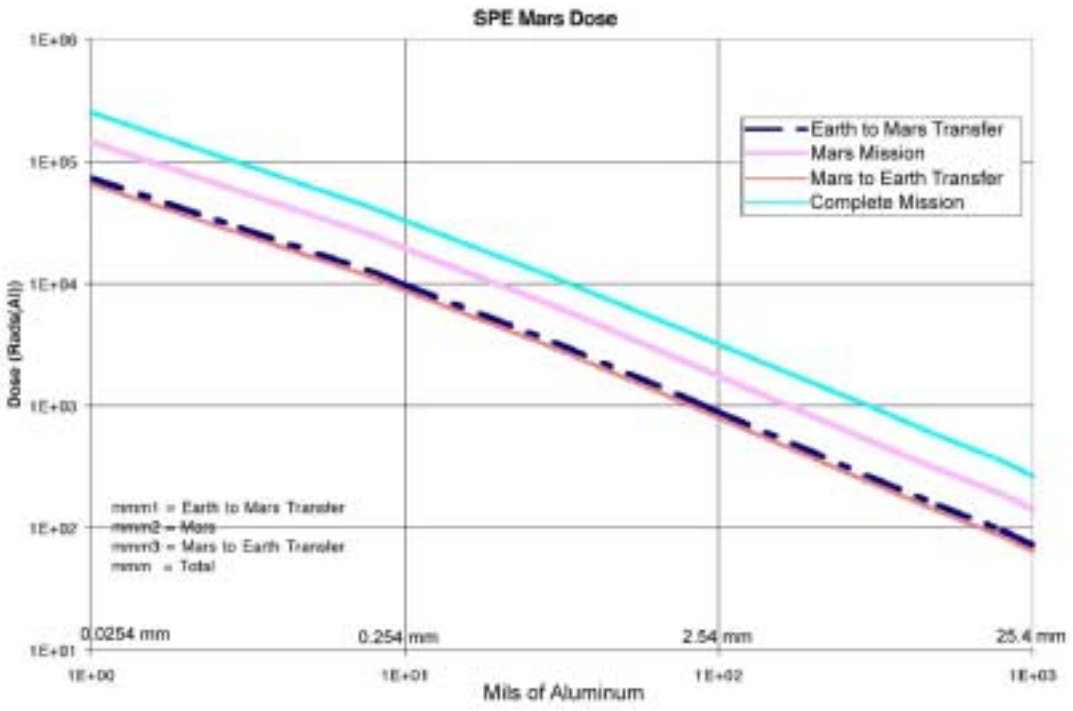

Figure 2-3. Plot of Table 2-3. 95 percent probability SPE doses for 3 segments and total mission. A 4π spherical shield of Aluminum is assumed.

2.2.2 Solar Proton Event Heavy Ion Model

In addition to dose, the single event environment (SEE) is critical to determining effects of the radiation environment on a space mission. Table 2-4 gives the LET spectra behind several spherical shield thickness for heavy ions in a 99th percentile flare. These spectra are derived from the same type statistical model as the flare proton model above. Results of this model, description[2-3, 2-4, 2-5, 2-6, 2.7] and spectra,[2-8, 2-9, 2-10] are plotted in figure 2-3.

Table 2-4. Integral heavy ion flux versus LET at 1 AU for a single 99th percentile SPE behind a 4π spherical aluminum shield (1 mil = 10^{-3} inch = 10^{-3} x 2.54 cm)

LET (MeV cm^2/mg)	Flux (cm^{-2} day^{-1}) behind Al Spherical Shield of Thickness (mils):					
	Zero mils (0 mm)	60 mils (1.52 mm)	100 mils (2.54 mm)	250 mils (6.35 mm)	500 mils (12.7 mm)	1000 mils (25.4 mm)
1.00	1.352e+08	1.565e+06	2.01e+05	4.71e+04	4.40e+03	2.57e+02
1.26	1.323e+08	8.589e+05	1.00e+05	2.17e+04	1.96e+03	1.13e+02
1.58	1.302e+08	2.682e+05	1.89e+04	1.68e+03	5.64e+01	8.10e-01
2.00	1.289e+08	2.031e+05	1.38e+04	1.14e+03	3.79e+01	5.40e-01
2.51	1.136e+08	1.457e+05	9.66e+03	7.46e+02	2.43e+01	3.28e-01
3.13	1.109e+08	8.966e+04	5.70e+03	4.25e+02	1.32e+01	1.69e-01
3.98	9.149e+07	6.002e+04	3.73e+03	2.75e+02	8.46e+00	1.08e-01
5.01	7.947e+07	5.597e+04	2.03e+03	1.36e+02	3.78e+00	4.11e-02
6.31	7.087e+07	1.750e+04	9.73e+02	5.82e+01	1.51e+00	1.53e-02
7.94	3.319e+07	7.067e+03	3.43e+02	1.36e+01	2.29e-01	1.66e-03
10.00	2.537e+07	3.976e+03	1.76e+02	6.09e+00	9.42e-02	4.97e-04
12.59	1.783e+07	2.008e+03	7.85e+01	2.04e+00	2.09e-02	8.13e-05
15.85	9.761e+06	5.856e+02	2.08e+01	4.49e-01	3.04e-03	7.34e-06
19.95	8.908e+06	3.079e+02	1.04e+01	2.17e-01	1.32e-03	2.82e-06
25.12	5.550e+06	1.057e+02	3.57e+00	7.38e-02	4.38e-04	9.04e-07
31.62	1.149e+03	2.518e-02	7.44e-04	7.91e-06	3.90e-08	6.02e-11
39.81	1.291e+02	1.923e-03	4.08e-05	3.00e-07	8.48e-10	6.42e-13
50.12	5.055e+01	6.429e-04	1.17e-05	6.74e-08	1.37e-10	5.14e-14
63.10	2.036e+01	1.372e-04	2.21e-06	1.11e-08	1.86e-11	6.92e-15
79.43	1.130e+00	5.403e-06	6.57e-08	1.66e-10	1.67e-13	2.15e-17
100.00	4.332e-02	1.433e-07	1.58e-09	2.51e-12	1.75e-15	7.95e-20
110.00	1.000e-20	1.000e-20	1.00e-20	1.00e-20	1.00e-20	1.00e-20

2.2.3 Galactic Cosmic Ray Heavy Ions

In the absence of a SPE, the dominant Single Event Effects radiation source is the Galactic Cosmic Ray background. The GCR heavy ion fluxes for various shielding thicknesses are given in table 2-5. These spectra are for an "Adams' 90 percent worst-case" environment (M=3).[2-12] The results are plotted in figure 2-4.

Table 2-5. GCR heavy ion fluxes versus LET behind an Aluminum spherical shield (4π) for an Adams' 90 percent worst-case environment (M=3).[2-12]

LET (MeV cm^2/mg)	Flux (cm^{-2} day^{-1})						
	Zero mil (0 mm)	**25 mil (0.635 mm)**	**60 mils (1.52 mm)**	**100 mils (2.54 mm)**	**250 mils (6.35 mm)**	**500 mils (12.7 mm)**	**1000 mils (25.4 mm)**
1.0058	6.24e+02	3.34e+02	2.91e+02	2.72e+02	2.40e+02	2.05e+02	1.52e+02
2.0064	2.38e+02	7.42e+01	5.69e+01	5.08e+01	4.31e+01	3.53e+01	2.43e+01
2.5071	1.87e+02	4.70e+01	3.42e+01	3.02e+01	2.55e+01	2.08e+01	1.42e+01
2.9962	1.56e+02	3.26e+01	2.27e+01	1.98e+01	1.67e+01	1.36e+01	9.31e+00
3.5018	1.34e+02	2.38e+01	1.60e+01	1.38e+01	1.16e+01	9.48e+00	6.47e+00
4.0026	1.17e+02	1.82e+01	1.19e+01	1.02e+01	8.61e+00	7.02e+00	4.78e+00
5.0013	9.36e+01	1.15e+01	7.12e+00	6.02e+00	5.09e+00	4.16e+00	2.83e+00
5.5286	8.44e+01	9.35e+00	5.63e+00	4.75e+00	4.02e+00	3.29e+00	2.23e+00
6.0438	7.77e+01	7.79e+00	4.58e+00	3.85e+00	3.26e+00	2.67e+00	1.80e+00
6.5339	7.19e+01	6.59e+00	3.79e+00	3.18e+00	2.69e+00	2.21e+00	1.49e+00
7.0637	6.65e+01	5.54e+00	3.12e+00	2.62e+00	2.22e+00	1.82e+00	1.23e+00
7.5519	6.11e+01	4.65e+00	2.58e+00	2.17e+00	1.85e+00	1.51e+00	1.02e+00
10.088	4.80e+01	2.47e+00	1.27e+00	1.06e+00	9.01e-01	7.38e-01	4.95e-01
15.065	2.93e+01	8.30e-01	3.90e-01	3.28e-01	2.84e-01	2.33e-01	1.55e-01
20.124	1.49e+01	3.48e-01	1.58e-01	1.33e-01	1.15e-01	9.44e-02	6.28e-02
25.146	5.63e+00	1.21e-01	5.46e-02	4.63e-02	4.02e-02	3.28e-02	2.18e-02
30.051	1.18e-01	2.34e-03	1.18e-03	1.05e-03	9.13e-04	7.22e-04	4.63e-04
35.913	2.22e-03	7.87e-05	5.57e-05	5.40e-05	4.66e-05	3.33e-05	1.78e-05
40.145	1.41e-03	4.96e-05	3.59e-05	3.53e-05	3.04e-05	2.15e-05	1.13e-05
45.377	8.41e-04	2.96e-05	2.19e-05	2.17e-05	1.88e-05	1.31e-05	6.71e-06
50.162	5.91e-04	2.01e-05	1.48e-05	1.48e-05	1.28e-05	8.91e-06	4.49e-06
55.451	3.84e-04	1.28e-05	9.54e-06	9.63e-06	8.37e-06	5.76e-06	2.85e-06
60.618	2.34e-04	7.89e-06	5.93e-06	6.06e-06	5.30e-06	3.60e-06	1.75e-06
65.533	1.52e-04	5.09e-06	3.82e-06	3.95e-06	3.48e-06	2.35e-06	1.12e-06
70.063	1.17e-04	3.71e-06	2.73e-06	2.84e-06	2.52e-06	1.70e-06	8.03e-07
74.905	8.81e-05	2.61e-06	1.88e-06	1.96e-06	1.75e-06	1.18e-06	5.55e-07
80.081	6.15e-05	1.70e-06	1.19e-06	1.26e-06	1.13e-06	7.60e-07	3.55e-07
85.616	3.23e-05	8.50e-07	5.93e-07	6.28e-07	5.68e-07	3.79e-07	1.76e-07
90.519	1.30e-05	3.37e-07	2.38e-07	2.52e-07	2.27e-07	1.51e-07	6.93e-08
95.703	1.65e-06	4.25e-08	3.26e-08	3.50e-08	3.09e-08	2.00e-08	8.87e-09
100.060	1.01e-06	2.53e-08	1.92e-08	2.06e-08	1.83e-08	1.18e-08	5.23e-09
102.320	4.01e-07	1.00e-08	7.64e-09	8.20e-09	7.25e-09	4.67e-09	2.06e-09
104.620	6.88e-08	1.71e-09	1.30e-09	1.40e-09	1.24e-09	7.96e-10	3.51e-10

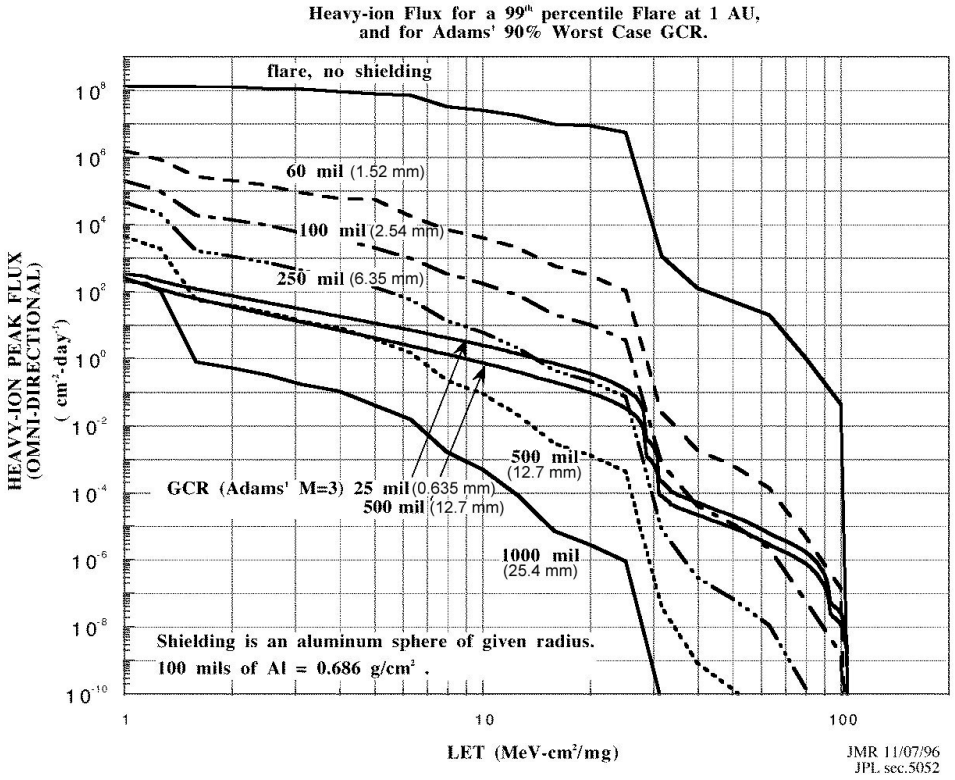

Figure 2-4. Heavy-ion flux for 99th percentile SPE and 90 percent worst case GCR background flux as functions of shielding and LET at 1 AU.[2-11]

2.3 Meteoroid Environment

2.3.1 Introduction

A growing concern for many missions is the possibility of a meteoroid impact. This section presents estimates of the meteoroid environment for the three segments presented in table 2-6. These estimates are based on the Divine model of interplanetary meteoroids.[2-13 2-14] The fluences as functions of mass and velocity bins (required for computing the critical penetrating fluence which is a function of both mass and impact velocity) are provided, with the assumption that the spacecraft is represented by a randomly tumbling surface. It may be desirable as the mission definition becomes more clearly defined to compute the fluence for oriented surfaces.[2-14] The effects of focusing and shielding by Mars on the meteoroid fluences were studied but, for Mars, these effects approximately cancel each other and are not presented here.

2.3.2 Model Limitations

In this description of the meteoroid environment, the reader is cautioned about the limitations of this (and other) meteoroid models, i.e.,

1) Very little good meteoroid data exist in the size regimes capable of damaging spacecraft for the near-Earth environment; data collected during the 1960's have recently shown severe biases. There are essentially no data for trans-Martian or near-Mars space.

2) Because of (1), ALL current meteoroid models[2-13 2-15 2-16] are in significant error with respect to fluxes at the high end of the mass range (area of most concern to spacecraft designers). These models vastly underestimate (by at least a factor of 100) the number of high velocity meteoroids, and inaccurately reflect the directionality of the meteoroid environment.

With these two caveats, table 2-6 gives the background meteoroid fluences for the segments of the proposed mission and table 2-7 presents the total mission fluences. Figures 2-5 and 2-6 represent these results graphically.

Table 2-6. Interplanetary meteoroid fluences (particles m^{-2}) for the 3-orbit segments presented in Fig. 2-1. The Mars Orbit segment is at an altitude of 200 km.

From Earth to Mars (25 Jan 2014—22 Jul 2014)

mass (g)	total	0-10 km/s	10-15 km/s	15-20 km/s	20-25 km/s	25-30 km/s	30-40 km/s	40-∞ km/s
1.00E-12	4.69E+02	1.31E+02	1.35E+02	9.55E+01	5.10E+01	2.64E+01	1.33E+01	1.71E+01
1.00E-11	2.25E+02	6.15E+01	6.40E+01	4.58E+01	2.53E+01	1.37E+01	6.92E+00	7.58E+00
1.00E-10	1.06E+02	2.79E+01	2.96E+01	2.16E+01	1.27E+01	7.41E+00	3.86E+00	3.37E+00
1.00E-09	4.73E+01	1.29E+01	1.35E+01	9.68E+00	5.43E+00	3.01E+00	1.48E+00	1.36E+00
1.00E-08	1.78E+01	5.10E+00	5.21E+00	3.66E+00	1.90E+00	9.42E-01	4.37E-01	5.45E-01
1.00E-07	4.30E+00	1.29E+00	1.31E+00	9.05E-01	4.53E-01	2.08E-01	7.38E-02	5.55E-02
1.00E-06	6.82E-01	2.14E-01	2.13E-01	1.43E-01	6.99E-02	3.10E-02	9.20E-03	2.40E-03
1.00E-05	8.61E-02	3.04E-02	2.81E-02	1.65E-02	7.40E-03	2.91E-03	7.66E-04	7.52E-05
1.00E-04	1.05E-02	4.23E-03	3.61E-03	1.76E-03	6.74E-04	1.97E-04	3.86E-05	2.19E-06
1.00E-03	8.43E-04	3.53E-04	2.94E-04	1.35E-04	4.81E-05	1.18E-05	1.71E-06	5.52E-08
1.00E-02	4.68E-05	1.98E-05	1.64E-05	7.38E-06	2.59E-06	5.98E-07	7.56E-08	1.40E-09
1.00E-01	2.21E-06	9.39E-07	7.77E-07	3.47E-07	1.21E-07	2.72E-08	3.22E-09	3.58E-11
1.00E+00	1.03E-07	4.37E-08	3.61E-08	1.61E-08	5.58E-09	1.24E-09	1.41E-10	9.25E-13
1.00E+01	4.79E-09	2.04E-09	1.68E-09	7.48E-10	2.59E-10	5.71E-11	6.36E-12	2.45E-14
1.00E+02	2.24E-10	9.51E-11	7.86E-11	3.49E-11	1.21E-11	2.65E-12	2.91E-13	6.72E-16
1.00E+03	1.04E-11	4.44E-12	3.67E-12	1.63E-12	5.64E-13	1.23E-13	1.35E-14	1.96E-17

Orbiting at Mars (22 Jul 2014—3 Jan 2016)

mass (g)	total	0-10 km/s	10-15 km/s	15-20 km/s	20-25 km/s	25-30 km/s	30-40 km/s	40-∞ km/s
1.00E-12	8.88E+02	3.29E+02	2.57E+02	1.56E+02	5.15E+01	1.77E+01	2.20E+01	5.41E+01
1.00E-11	4.14E+02	1.54E+02	1.21E+02	7.30E+01	2.40E+01	8.08E+00	9.77E+00	2.40E+01
1.00E-10	1.86E+02	6.94E+01	5.43E+01	3.30E+01	1.10E+01	3.73E+00	4.35E+00	1.07E+01
1.00E-09	8.52E+01	3.22E+01	2.51E+01	1.52E+01	4.97E+00	1.60E+00	1.76E+00	4.29E+00
1.00E-08	3.40E+01	1.29E+01	1.01E+01	6.04E+00	1.94E+00	6.15E-01	7.07E-01	1.73E+00
1.00E-07	8.20E+00	3.32E+00	2.55E+00	1.51E+00	4.59E-01	1.15E-01	7.74E-02	1.72E-01
1.00E-06	1.35E+00	5.86E-01	4.27E-01	2.43E-01	7.18E-02	1.51E-02	4.33E-03	6.87E-03
1.00E-05	2.10E-01	1.05E-01	6.36E-02	3.10E-02	8.89E-03	1.50E-03	2.11E-04	1.72E-04
1.00E-04	3.21E-02	1.77E-02	9.31E-03	3.83E-03	1.06E-03	1.32E-04	8.02E-06	4.33E-06
1.00E-03	2.74E-03	1.55E-03	7.86E-04	3.08E-04	8.48E-05	9.33E-06	2.62E-07	1.09E-07
1.00E-02	1.54E-04	8.76E-05	4.42E-05	1.72E-05	4.70E-06	5.00E-07	9.26E-09	2.73E-09
1.00E-01	7.33E-06	4.17E-06	2.10E-06	8.11E-07	2.22E-07	2.33E-08	3.41E-10	6.87E-11

1.00E+00	3.42E-07	1.95E-07	9.78E-08	3.77E-08	1.03E-08	1.08E-09	1.35E-11	1.73E-12
1.00E+01	1.59E-08	9.09E-09	4.56E-09	1.76E-09	4.80E-10	4.99E-11	5.70E-13	4.33E-14
1.00E+02	7.44E-10	4.25E-10	2.13E-10	8.19E-11	2.24E-11	2.32E-12	2.51E-14	1.09E-15
1.00E+03	3.48E-11	1.98E-11	9.96E-12	3.83E-12	1.05E-12	1.08E-13	1.13E-15	2.74E-17

From Mars to Earth (3 Jan 2016—11 Jul 2016)

mass (g)	total	0-10 km/s	10-15 km/s	15-20 km/s	20-25 km/s	25-30 km/s	30-40 km/s	40-∞ km/s
1.00E-12	4.45E+02	1.22E+02	1.33E+02	8.49E+01	4.89E+01	2.50E+01	1.34E+01	1.75E+01
1.00E-11	2.11E+02	5.73E+01	6.30E+01	4.03E+01	2.36E+01	1.23E+01	6.44E+00	7.79E+00
1.00E-10	9.75E+01	2.58E+01	2.87E+01	1.87E+01	1.13E+01	6.20E+00	3.24E+00	3.46E+00
1.00E-09	4.40E+01	1.20E+01	1.32E+01	8.47E+00	5.00E+00	2.63E+00	1.30E+00	1.39E+00
1.00E-08	1.70E+01	4.78E+00	5.19E+00	3.27E+00	1.85E+00	9.14E-01	4.47E-01	5.60E-01
1.00E-07	4.13E+00	1.22E+00	1.31E+00	8.14E-01	4.47E-01	2.08E-01	7.34E-02	5.70E-02
1.00E-06	6.72E-01	2.08E-01	2.20E-01	1.32E-01	6.97E-02	3.09E-02	8.61E-03	2.47E-03
1.00E-05	9.44E-02	3.31E-02	3.27E-02	1.70E-02	7.84E-03	2.94E-03	7.07E-04	7.77E-05
1.00E-04	1.31E-02	5.13E-03	4.78E-03	2.15E-03	8.03E-04	2.09E-04	3.67E-05	2.26E-06
1.00E-03	1.09E-03	4.40E-04	4.04E-04	1.74E-04	6.04E-05	1.29E-05	1.70E-06	5.74E-08
1.00E-02	6.12E-05	2.48E-05	2.27E-05	9.68E-06	3.30E-06	6.64E-07	7.73E-08	1.47E-09
1.00E-01	2.91E-06	1.18E-06	1.08E-06	4.58E-07	1.55E-07	3.04E-08	3.34E-09	3.78E-11
1.00E+00	1.35E-07	5.50E-08	5.02E-08	2.13E-08	7.18E-09	1.39E-09	1.47E-10	9.95E-13
1.00E+01	6.30E-09	2.57E-09	2.34E-09	9.92E-10	3.34E-10	6.41E-11	6.67E-12	2.71E-14
1.00E+02	2.94E-10	1.20E-10	1.09E-10	4.63E-11	1.56E-11	2.98E-12	3.07E-13	7.79E-16
1.00E+03	1.38E-11	5.60E-12	5.11E-12	2.16E-12	7.27E-13	1.39E-13	1.42E-14	2.41E-17

Table 2-7. Interplanetary meteoroid fluences (particles m^{-2}) for the complete mission in Fig. 2-1.

Total Mars Mission (25 Jan 2014—11 Jul 2016)

mass (g)	total	0-10 km/s	10-15 km/s	15-20 km/s	20-25 km/s	25-30 km/s	30-40 km/s	40-∞ km/s
1.00E-12	1.80E+03	5.82E+02	5.25E+02	3.36E+02	1.51E+02	6.91E+01	4.87E+01	8.87E+01
1.00E-11	8.50E+02	2.73E+02	2.48E+02	1.59E+02	7.29E+01	3.41E+01	2.31E+01	3.94E+01
1.00E-10	3.90E+02	1.23E+02	1.13E+02	7.33E+01	3.50E+01	1.73E+01	1.15E+01	1.75E+01
1.00E-09	1.77E+02	5.71E+01	5.18E+01	3.34E+01	1.54E+01	7.24E+00	4.54E+00	7.04E+00
1.00E-08	6.88E+01	2.28E+01	2.05E+01	1.30E+01	5.69E+00	2.47E+00	1.59E+00	2.84E+00
1.00E-07	1.66E+01	5.83E+00	5.17E+00	3.23E+00	1.36E+00	5.31E-01	2.25E-01	2.85E-01
1.00E-06	2.70E+00	1.01E+00	8.60E-01	5.18E-01	2.11E-01	7.70E-02	2.21E-02	1.17E-02
1.00E-05	3.91E-01	1.69E-01	1.24E-01	6.45E-02	2.41E-02	7.35E-03	1.68E-03	3.25E-04
1.00E-04	5.57E-02	2.71E-02	1.77E-02	7.74E-03	2.54E-03	5.38E-04	8.33E-05	8.78E-06
1.00E-03	4.67E-03	2.34E-03	1.48E-03	6.17E-04	1.93E-04	3.40E-05	3.67E-06	2.22E-07
1.00E-02	2.62E-04	1.32E-04	8.33E-05	3.43E-05	1.06E-05	1.76E-06	1.62E-07	5.60E-09
1.00E-01	1.25E-05	6.29E-06	3.96E-06	1.62E-06	4.98E-07	8.09E-08	6.90E-09	1.42E-10
1.00E+00	5.80E-07	2.94E-07	1.84E-07	7.51E-08	2.31E-08	3.71E-09	3.02E-10	3.65E-12
1.00E+01	2.70E-08	1.37E-08	8.58E-09	3.50E-09	1.07E-09	1.71E-10	1.36E-11	9.49E-14
1.00E+02	1.26E-09	6.40E-10	4.01E-10	1.63E-10	5.01E-11	7.95E-12	6.23E-13	2.54E-15
1.00E+03	5.90E-11	2.98E-11	1.87E-11	7.62E-12	2.34E-12	3.70E-13	2.88E-14	7.11E-17

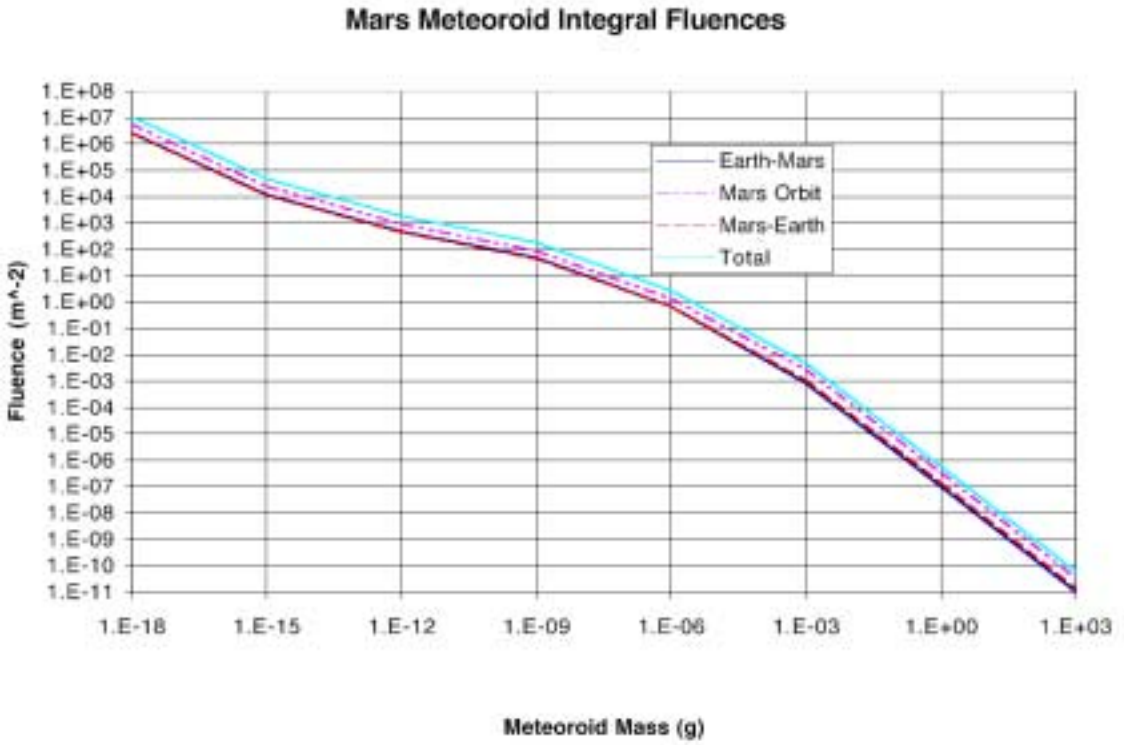

Figure 2-5. Integral Mars meteoroid fluences for the 3-mission segments and the total as functions of meteoroid mass. Units for fluence are number per square meter for the time interval of the segment.

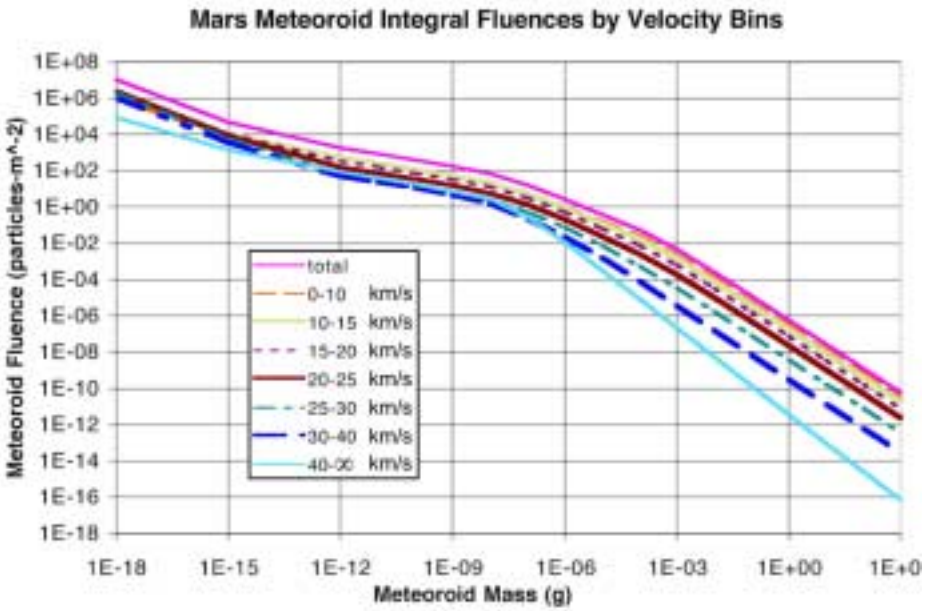

Figure 2-6. Integral Mars meteoroid fluences for the 3-mission segments and the total by velocity. Units for fluence are number per square meter for the time interval of the segment.

2.3.3 Fluence and Flux

While the fluence is a good measure of mission survivability, it is helpful to have an estimate of the flux (number of meteoroids of a given mass or size striking the spacecraft per unit area per unit time) that might be encountered in near-Mars space. This is integrated over any desired time interval to give number of impacts on the spacecraft. The model used in these calculations can also calculate the flux, which, for Mars orbit, is approximated by

$$\log F = -14.187 - 1.3164 \log m + 4.1347 x 10^{-3} (\log m)^2 - 1.3871 x 10^{-2} (\log m)^3 - 8.1004 x 10^{-3} (\log m)^4 - 7.9186 x 10^{-4} (\log m)^5, \quad (2\text{-}1)$$

where F is the flux in units of meteoroids m^{-2} s^{-1} and m is the mass in grams. The above expression is for Mars at perihelion. Because of the eccentricity of the Martian orbit, the meteoroid flux at Martian aphelion is about 25 percent less than the values given by this simple relation. The meteoroid speed relative to Mars is approximated by

$$v = 0.010775 e^{-0.866 \log m} + 9.63 \quad (2\text{-}2)$$

where v is the meteoroid speed in km s^{-1} and m is the mass in grams. This yields speeds about 67 percent smaller than that for meteoroids at Earth, not too surprising, given Mars' greater distance from the Sun. The meteoroid densities are assumed to be in the range 0.5 to 2 gm cm^{-3}.[2-16]

2.3.4 Meteor Streams Near Mars

The preceding paragraphs provide a description of the background (also called "sporadic") component of the meteoroid environment; however, it is also necessary to characterize a second component of the meteoroid environment – meteor streams. Consisting of particles (conglomerates of ice and dust, and possibly organics) ejected from comets as they pass through the inner Solar System, these streams cause meteor showers (or rarely more intense meteor storms) here on Earth. Since Mars is visited by about twice the number of comets as Earth, it is to be expected that Mars will encounter more meteor streams. Preliminary calculations indicate a fair number of Martian meteor showers (table 2-8). Note the clustering of encounters in December 1999, June 2000, and May 2001, which may indicate strong meteor activity. Mission planners should project these dates forward to the mission times and allow for an enhancement of the meteoroid flux during these periods. Fortunately (from a penetration and plasma generation viewpoint), the meteor speeds are rather low except for particles originating from Comet Olbers.

Table 2-8. Comet close passages to Mars in the near future. Additional meteor shower dates may be calculated by adding or subtracting multiples of 687 days from the dates given.

Comet name	Close approach distance (10^6 km)	Meteor speed (km s^{-1})	Date of peak of meteor shower	Date of Peak in 2014-2016
Jackson-Neujmin	1.7	9.9	1999 December 15	2015 November 18
Boethin	5.5	13.6	1999 December 16	2015 November 19
Shoemaker 2	1.2	12.7	2000 April 7	2016 February 12
Kushida	7.3	11.3	2000 April 22	2016 February 27
Haneda-Campos	1.9	9.6	2000 May 1	2016 March 7
Stephan-Oterma	3.9	11.8	2000 May 27	2016 April 2
West-Kohoutek-Ikemura	5.3	14.4	2000 June 4	2016 April 10
Olbers	3.4	26.9	2000 June 4	2016 April 10
Wiseman-Skiff	0.9	11.1	2000 June 6	2016 April 12
Howell	6.9	6.6	2001 May 24	2015 July 7
Tempel 1	1.0	7.5	2001 May 25	2015 July 8
D'Arrest	4.9	11.9	2001 September 25	2016 April 1

2.3.5 Spacecraft Strike Probability

Not only are planets subjected to meteor streams but so are spacecraft in interplanetary space. In mid-September 1967, Mariner IV encountered a meteor stream at a distance of 1.273 astronomical units (AU) from the Sun, about midway between the orbits of Mars and Earth. The onboard dust detector registered an increase in the meteor flux by a factor of 1000 over the background for some 45 minutes, during which the spacecraft was torqued about its roll axis and had thermal insulation torn away. Mariner IV continued on its way without further incident. This historical example illustrates very nicely the characteristics of meteor streams: particle densities three to four orders of magnitude greater than normal with widths on the order of a couple hundred thousand kilometers (about an hour's travel at normal interplanetary speeds). Unfortunately, there are insufficient dynamical studies or measurements to map the locations of these debris clouds between Earth and Mars. It is currently thought that the odds of a spacecraft encountering one are small (but probably not ignorable).

2.4 Solar Radiation and Thermal Environments

2.4.1 Near Earth

Direct solar irradiance at Earth averages about 1367 W/m^2 and varies during a year from about 1322 W/m^2 at aphelion (early July) to about 1414 W/m^2 at perihelion (early January). Planetary albedo (fractional reflected solar radiation) varies from about 0.06 to 0.54. Outgoing longwave radiation (infrared radiation thermally emitted by the Earth-atmosphere system) varies from about 150 W/m^2 to about 350 W/m^2. Anderson and Smith[2-16] give details of the variations of albedo and outgoing longwave radiation with averaging time and orbital inclination (latitude).

2.4.2 Interplanetary

Direct solar irradiance varies inversely with square of the distance from the Sun (1367 W/m^2 at a distance of 1 Astronomical Unit). The infrared radiative sink temperature for deep space away from the influence of planetary bodies is 3 K (5×10^{-6} W/m^2).

2.4.3 Mars Orbit

Direct solar irradiance at the top of the Mars atmosphere varies from about 493 W/m^2 at Mars aphelion to about 717 W/m^2 at Mars perihelion (average value 589 W/m^2). Planetary albedo for Mars averages about 0.25 and varies between about 0.1 and 0.4 (figure 4-10) except at the polar caps where it is about 0.6. Major dust storms cause some increase in planetary albedo. Because of the thin atmosphere, outgoing longwave radiation at the top of the Mars atmosphere is changed little from upwelling longwave radiation (controlled by surface temperature) at the surface. Top of atmosphere on Earth is considered to be 30 km, where the pressure is about 1 percent of its surface value, i.e., about 10 mb. The surface pressure on Mars is less than 10 mb. Although absorption and emission by carbon dioxide have some effect on radiative transfer, the radiative top of atmosphere on Mars is very near the surface. Since surface temperature varies between about 140 K at polar night to about 280 K in southern summer mid-day (figure 3-5), outgoing longwave radiation ranges between about 20 W/m^2 and about 350 W/m^2.

2.5 References

2-1 Jordan, Thomas: "A Radiation Transport Shielding Code, Experimental and Mathematical Physics Consultants." *NOVICE*, 1998.

2-2 IOM 5217-92-23 Feynman, J., Spitale, G., and Wang, J. to Murphy, G.: "Interplanetary Proton Fluence Model, JPL 1991." 1992.

2-3 Feynman, J., Spitale, G., Wang, J., and Gabriel, S.: "Interplanetary Proton Fluence Model: JPL 1991." *Journal of Geo. Res.*, Vol. 98 (A8), p. 13281, 1993.

2-4 IOM 5217-92-19 Croley, D. to Murphy, G.: "Construction of High Energy Ion Time Profiles During the October 1989 Solar Flares From Data Taken by the Galileo Heavy Ion Counter (HIC)." 1992.

2-5 IOM 5215-92-072 Croley, D.R. and Cherng, Michael to Murphy, G.B.: "Procedure for Specifying the Heavy Ion Environment at 1AU." 1992.

2-6 IOM 5215-92-075 Croley, D. R. to Murphy, G.B.: “Spectral Shape of Solar Flare Heavy Ions.” 1992.

2-7 IOM 5215-92-042 Croley, D. R. to Murphy, G. B.: “Solar Flare Heavy Ion Model.” 1992.

2-8 IOM 5217-92-60 Spitale, G., Feynman, J., and Wang, J. to Murphy, G.: “Solar Alpha Particle Model: Progress and Problems.” 1992.

2-9 IOM 5215-92-143 Ratliff, M. to Edmonds, L.: “1992 Model of Solar Flare Heavy Ions: Selected Spectra.” (Note that the 99th percentile flare is referred to as a 1% flare.)

2-10 IOM 5217-91-52 Cherng, M. to Albrecht, V.: “CRAF/Cassini CDU SEU / Latch-up Analyses.” 1991.

2-11 Adams, J.H. Jr.: “Cosmic Ray Effects on Microelectronics (CREME) - Part I: The Near-Earth Particle Environment.” NRL Memorandum Report 4506, pp. 14-15, 1981.

2-12 Adams, J.H. Jr.: “Cosmic Ray Effects on Microelectronics, (CREME) - Part IV.” NRL Memorandum Report 5901, 1986.

2-13 Divine, N.T.: “Five Populations of Interplanetary Meteoroids.” *J. Geophys. Res.*, Vol. 98, No. E9, pp. 17 029 - 17 048, September 1993.

2-14 Garrett, H. B., et al.: “Interplanetary Meteoroid Environment Model Update.” *J. Spacecraft*, Vol. 36, No. 1, pp. 124-132, January-February 1999.

2-15 Grün, E., Zook, H.A., Fechtig, H. and Giese, R.H.: “Collisional Balance of the Meteoritic Complex.” Icarus, Vol. 62, pp. 244-272, 1985.

2-16 Anderson, B. J. and Smith, R. E.: “Natural Orbital Environment Guidelines for Use in Aerospace Vehicle Development.” NASA Technical Manual 4527, pp. 7-1 to 7-4, 1994.

3.0 MARS ATMOSPHERIC ENVIRONMENT

3.1 Climatology

3.1.1 Orbit

The mean Mars orbit is approximately 227 900 000 km from the Sun (149 600 000 km for Earth). Compared to Earth's orbit, Mars' orbit is somewhat eccentric. As a consequence, the seasonal cycle is not symmetrical. The incoming solar flux at the top of the atmosphere is approximately 40 percent more at Southern Hemisphere summer solstice than at Northern Hemisphere summer solstice. In the Northern Hemisphere, autumn and winter are 143 and 154 sols, respectively, (Mars days), compared to 194 and 178 sols in the Southern Hemisphere. The surface of Mars is cold, dry, has a thin atmosphere, and is devoid of obvious life. Due to its highly eccentric orbit, the average Martian surface temperature ranges from as little as –133° C at the winter pole to almost 27° C on the dayside during summer, and averages –55° C.

3.1.2 Atmosphere

Mars has a very thin atmosphere composed mostly of carbon dioxide (95.3 percent), plus nitrogen (2.7 percent), argon (1.6 percent) and traces of oxygen (0.15 percent) and water (0.03 percent). The average pressure on the surface of Mars is only about seven millibars (less than 1 percent of Earth's), but it varies greatly with altitude from almost nine millibars in the deepest basins to about 1 millibar at the top of Olympus Mons. The atmosphere is thick enough to support very strong winds and vast dust storms that occasionally engulf the entire planet for months. Mars' thin atmosphere produces a weak greenhouse effect that raises the surface temperature by 5K; much less than on Venus (500K) and Earth (33K). Atmospheric variations have an impact on spacecraft entering the atmosphere as atmospheric uncertainties and entry body drag variations are major contributors to variations in entry trajectory and potential causes of navigation error.[3-1]

3.1.3 Thermal Conditions

Thermal conditions on Mars vary considerably, temporally and spatially, and depend on the latitude, season, and amount of suspended dust particles. The atmosphere is heated by absorption of solar radiation and cooled by infrared emission. Two components drive these processes: (1) CO_2 and (2) dust, which vary as a function of season and latitude. CO_2 absorbs the infrared solar flux. This has negligible impact on ground insolation, but it increases the temperature profile about 10°C at sunny latitudes above 50 km. CO_2 also creates a greenhouse effect up to 10 W/m^2 that may increase the local ground and atmosphere temperatures.[3-2]

3.1.4 Near Surface Climate

Compared to Earth the Martian ground has a low thermal inertia. The Martian ground surface is generally near radiative equilibrium due to low heat capacity of the atmosphere. The diurnal temperature cycle is very strong. Temperatures at the Martian surface depend on latitude, season, time of day, and properties of the surface itself, mainly its albedo and thermal inertia (see sections 4.3.2 through 4.3.4). This temperature cycle has been modeled[3-3] and results presented in figure 3-1.[3-4] Temperatures are at their lowest just before dawn, rise rapidly in the morning to a maximum just after noon, then fall rapidly in the afternoon and more slowly during the night to their predawn low. The temperature cycle measured by Mars Pathfinder[3-5] is presented in figure 3-2.

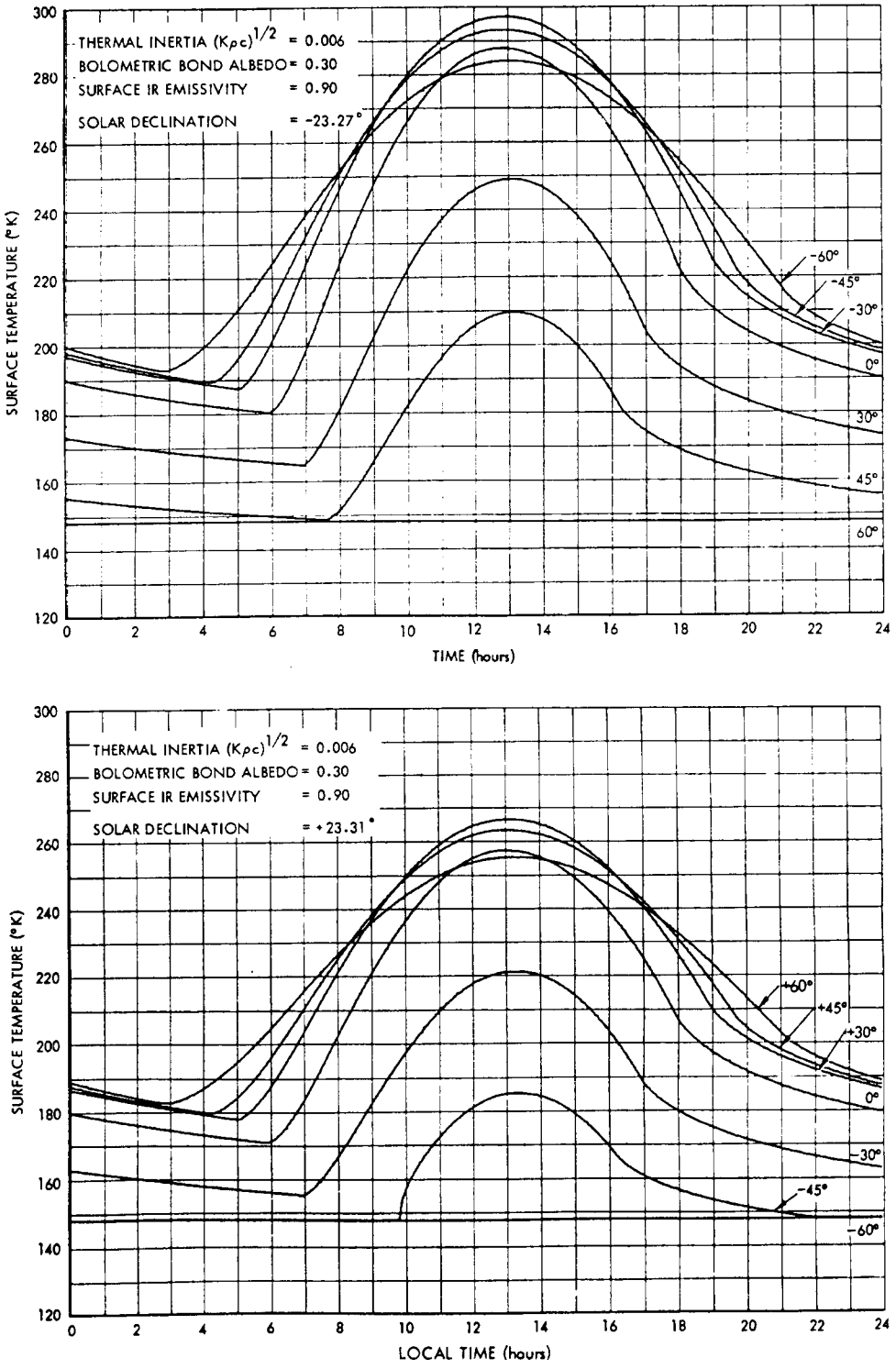

Figure 3-1. Models of the Daily Temperature Fluctuations of the Martian Surface as a Function of Latitude. The upper diagram shows the situation at perihelion, when it is summer in the south; the lower diagram is for aphelion, when it is winter in the south (after Michaux and Newburn, 1972[3-3] and given in Carr[3-4]).

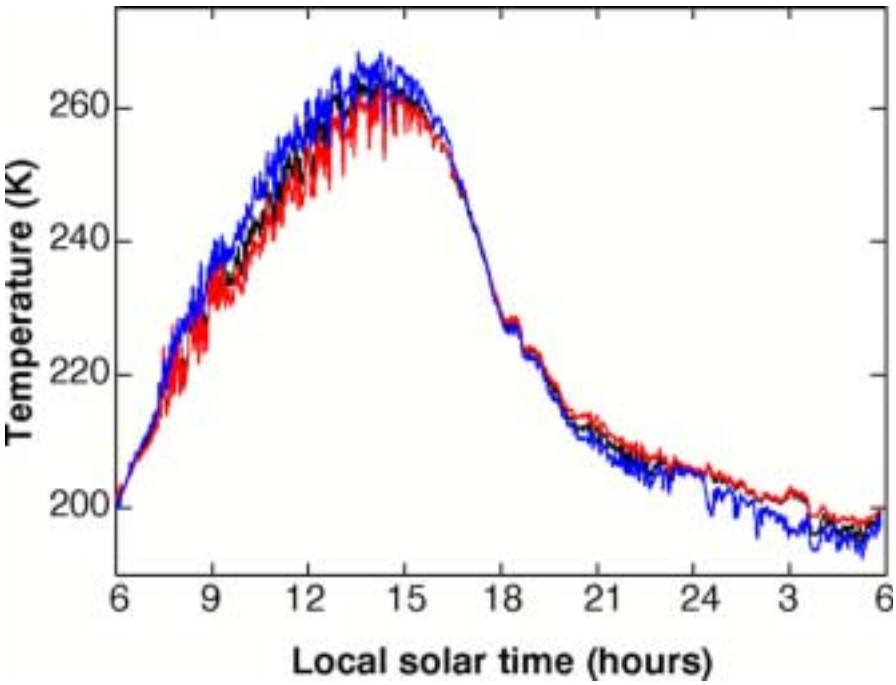

Figure 3-2. Diurnal Variation in Atmospheric Temperature Measured by Thermocouples on the Pathfinder Mast. Measurements correspond to thermocouples at 100, 50, and 25 cm above the lander solar panels.[3-5]

3.1.5 Density and Temperature Profiles

Figure 3-3 provides profiles measured by the Viking and Pathfinder missions[3-5] of atmospheric density and temperature as functions of altitude. Atmospheric density decreases roughly exponentially with altitude (figure 3-3a). Temperature (figure 3-3b) does not decrease smoothly between the surface and 40-km altitude. Furthermore, above 40 km there are pronounced gravity waves in the altitude vs. temperature profile.

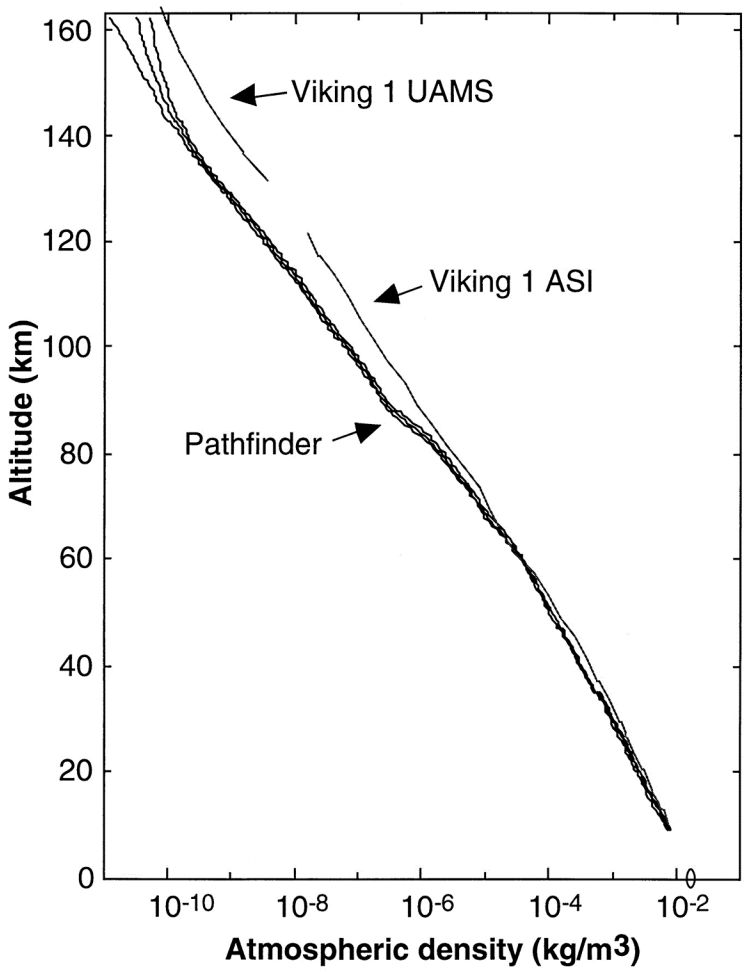

Figure 3-3a. Observed Density of the Mars Atmosphere Versus Altitude for the Viking and Pathfinder Missions.[3-5] ASI is atmospheric structure investigation; UAMS is upper atmosphere mass spectrometer.

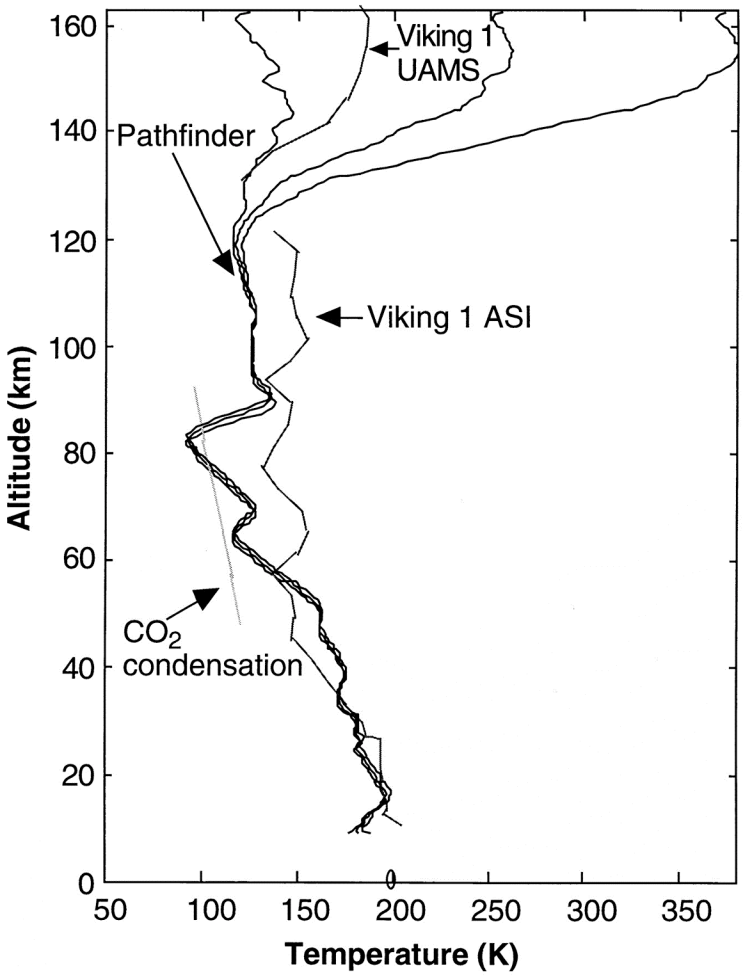

Figure 3-3b. Observed Temperature of the Mars Atmosphere Versus Altitude for the Viking and Pathfinder Missions.[3-5] ASI is atmospheric structure investigation; UAMS is upper atmosphere mass spectrometer.

3.2 Surface Air Temperature

3.2.1 Temperature Range

Like Earthly deserts, afternoon surface air temperatures on Mars are (in relative terms) high but plunge sharply at night. Figure 3-4 shows daily temperature variations observed by the Mars Pathfinder lander during its first few days of operation. The diurnal range seen here is about 60 °C. Figure 3-5 shows the range of maximum and minimum surface air temperatures with latitude and season. During southern summer, the diurnal temperature range on Mars can exceed 70 °C. This equals the diurnal temperature range of a hypothetical Earthly desert that reaches over 120 °F (49 °C) in daytime with temperature plunging below 0 °F (-18 °C) at night. Although such temperatures are found at various times in Earth's deserts, maximum temperature range during a given day would not exceed about 60 °F (33 °C). Although diurnal temperature range is large on Mars, daytime high temperatures rarely exceed 0 °C.

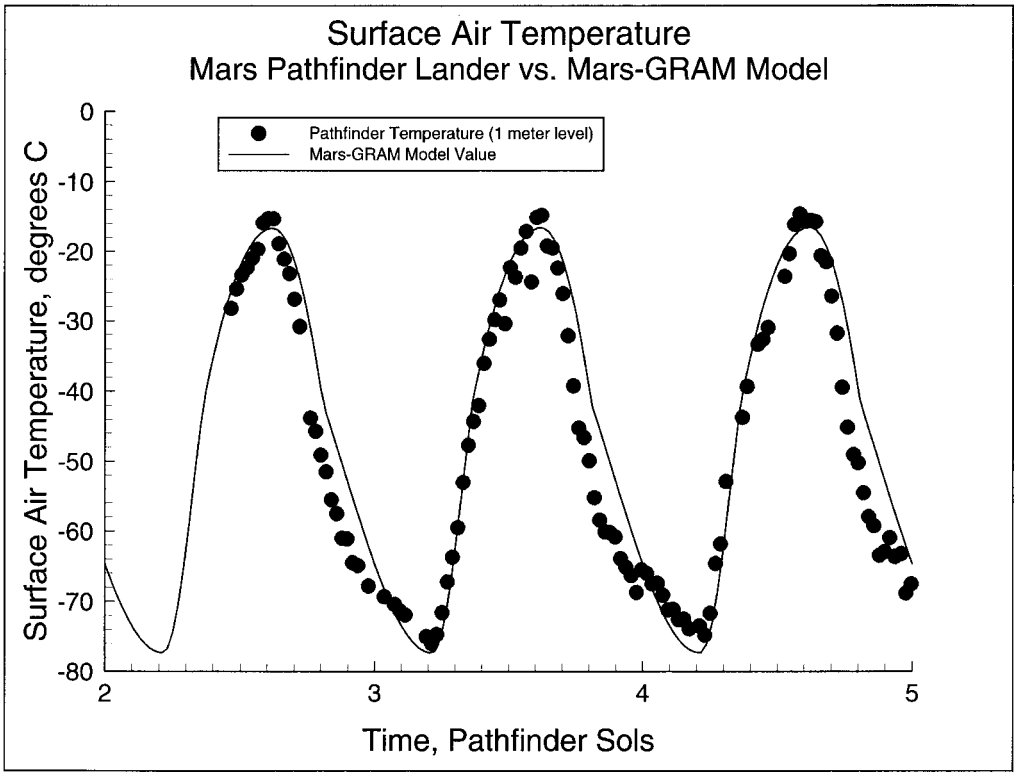

Figure 3-4. First few days of surface air temperature measured by Mars Pathfinder lander.[3-5] Solid curve is from Mars-Global Reference Atmospheric Model.[3-6]

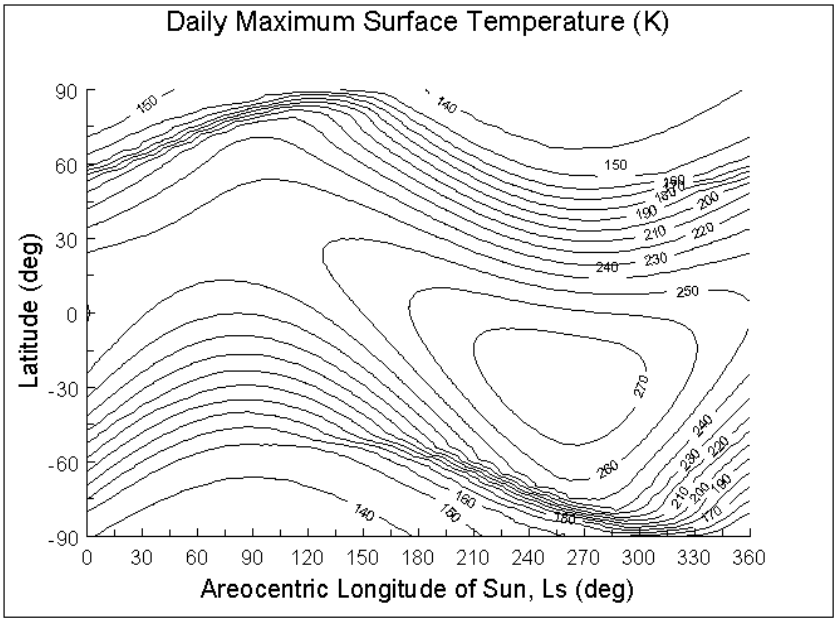

(a)

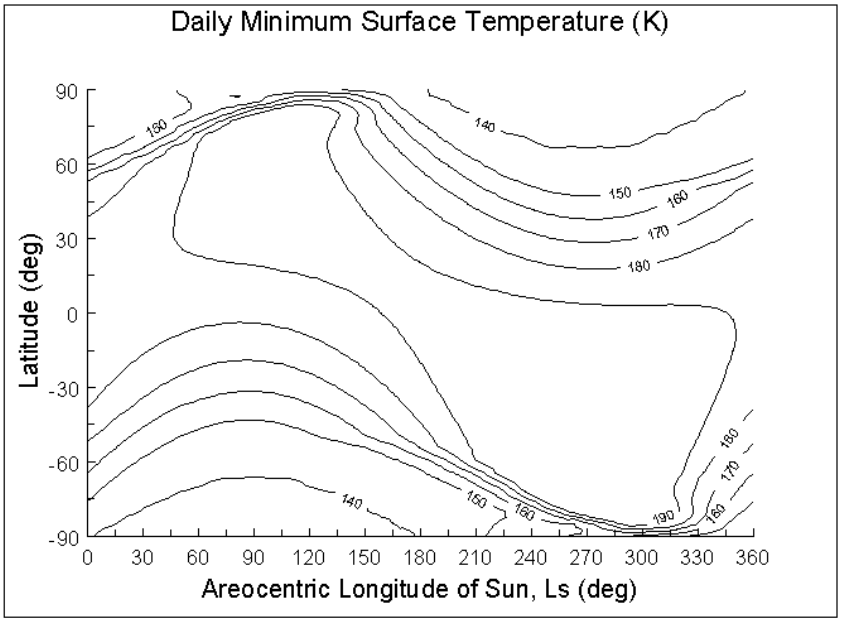

(b)

Figure 3-5. Daily maximum (a) and daily minimum (b) surface air temperature as a function of latitude and season. Season on Mars is measured by angle L_s, with 0 = spring equinox, 90° = summer solstice, 180° = fall equinox, and 270 ° = winter solstice (in the Northern Hemisphere).

3.2.2 Dust Storm Effects

Dust storms occur frequently on Mars and significantly affect surface temperature. Figure 3-6 shows time history of daily maximum, minimum and average surface air temperature measured during approximately one Earth year by the Viking 1 lander. The influence of two dust storms is evident (1977a and 1977b, starting near L_s = 210° and 312°, respectively). Since dust blocks incoming sunlight, it lowers average temperature and significantly lowers maximum temperature. Dust also blocks outgoing thermal infrared radiation from the surface and raises minimum surface air temperature.

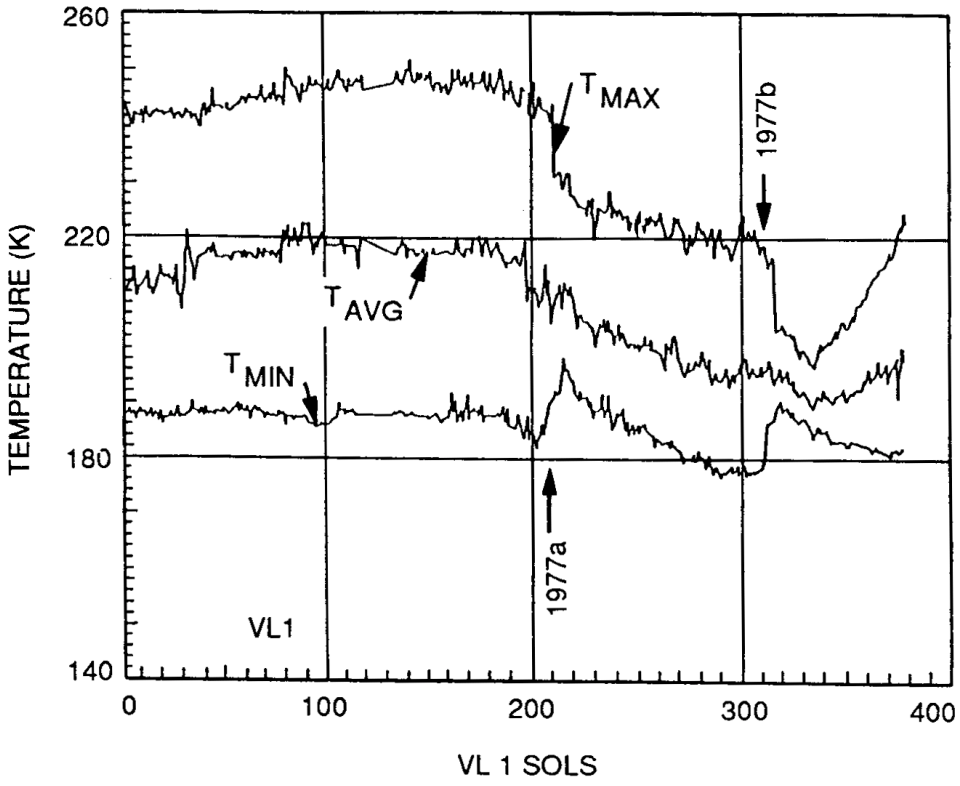

Figure 3-6. Maximum, average, and minimum surface air temperature measured by the Viking 1 lander. Effects of dust storms 1977a and 1977b are evident.[3-7]

3.3 Surface Air Pressure

3.3.1 Dust Storm Effects

Viking 1 and 2 lander measurements of surface pressure are shown for a full Mars year in figure 3-7. Surface air pressure at the reference datum level on Mars (analogous to sea level on Earth) averages about 6 mb (compared to mean sea level pressure of about 1000 mb on Earth). Surface pressure at both Viking lander sites averages higher than 6 mb because both lander sites were well below datum level (see Appendix A). Since surface air pressure is a measure of the weight of the atmospheric column of air above a site, such low surface pressures indicate that the mass of Mars' atmosphere is less than 1 percent that of Earth. Figure 3-7 also shows that the

effect of dust storms is to increase both mean atmospheric pressure and its variability (at least at the latitude of the Viking landers). This is a direct measure of the impact of dust on redistributing the atmospheric mass by perturbations in atmospheric circulation induced by atmospheric heating caused by dust.

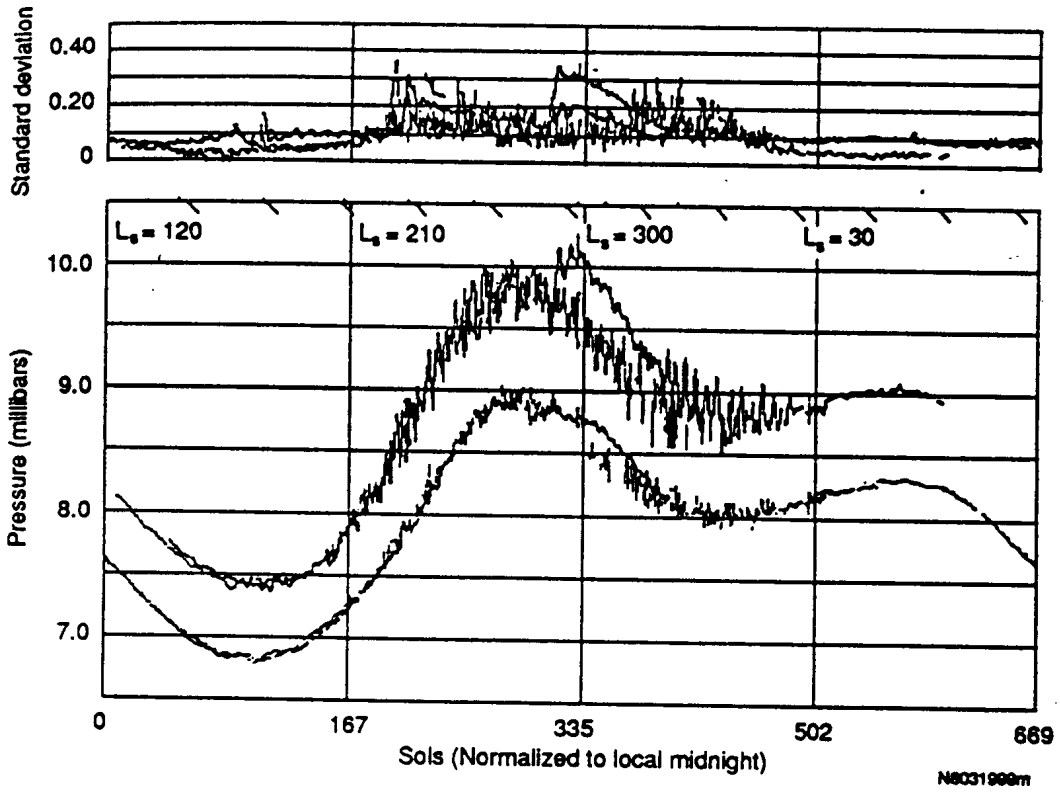

Figure 3-7. Variations of surface air pressure measured by Viking lander 1 (upper curve, lower panel) and Viking lander 2 (lower curve, lower panel).[3-8]

3.3.2 Polar Influence on Seasonal Changes

Large seasonal variations in surface pressure evident in figure 3-7 (maximum more than 40 percent greater than minimum) are due to substantial changes in the mass of Mars' atmosphere during the course of its year (seasonal variations in Earth's surface air pressure are no more than 1 to 2 percent and with essentially no seasonal change in the total mass of Earth's atmosphere). Since surface temperatures during Mars winters get colder than the freezing point of carbon dioxide (CO_2, the major constituent of Mars' atmosphere), part of the atmospheric CO_2 freezes and is precipitated (making snow consisting of particles of "dry ice") and deposited onto the winter polar cap. During summer, substantial amounts of this "dry ice" polar cap sublime back into the atmosphere as CO_2 vapor. Seasonal variations of pressure (atmospheric mass) seen in figure 3-7 are due to differences in CO_2 mass flux onto the winter pole and out of the summer pole and to the results of nonsymmetrical heating of the poles in northern and southern seasons.

3.4 Surface Wind and Dust Storms

3.4.1 Topographic Influence on Wind

Winds measured by the Viking landers were generally light at night (about 2 m/s) and stronger in daytime (6 to 8 m/s). Measured Mars Pathfinder winds were not strong enough to blow significant amounts of dust off the rover and special collector surfaces on the lander. Viking, however, showed that winds are driven to a large extent by strong upslope-downslope effects. Boundary layer models indicate that winds may approach 20 to 30 m/s in areas of significant topographic slope.

3.4.2 Dust Storms and Wind

Surface wind plays an important role in producing dust storms on Mars that can be local, regional, or global in size (see table 3-1). The exact role of surface wind is not yet completely understood. Dust storms have a preference for occurring during the strong solar heating period during Southern Hemisphere summer (between about L_s = 180° and 350°) shown in figure 3-8. Dust storms, especially those of global dimensions, do not occur every Mars year. Therefore, wind must play an additional triggering role in dust storm initiation. Proposed trigger mechanisms include (1) direct wind lifting (saltation) by strong, topographically-forced winds, (2) dust lofted by small "dust devil" circulations, similar to those frequently seen in Earthly deserts during summer (and confirmed to exist on Mars by both Pathfinder lander and Viking orbiter observations), and (3) dust lifting by strong downslope winds blowing off the northern edge of the south polar cap as it melts and retreats in southern summer. Once a dust storm reaches significant size, effects of atmospheric heating caused by the dust itself can cause changes in atmospheric circulation and stability that can allow the storm to grow to regional or global dimensions. Although much less frequent during southern winter than southern summer, local-scale dust storms can occur during all seasons and in both hemispheres (but are much more likely in the Southern Hemisphere) (section 3.5.2).

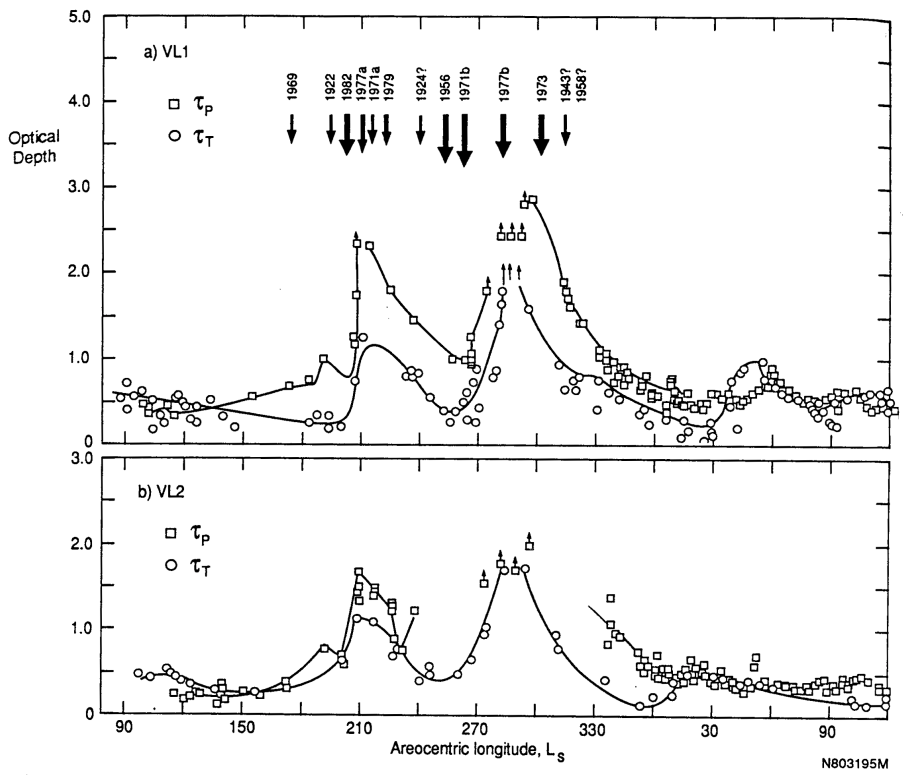

Figure 3-8. Occurrence and magnitude of Mars global dust storms (indicated by arrows) as a function of season (angle L_s), with a plot of dust optical depth measured by Viking landers.[3-9] Circles and squares indicate optical depth measured by two different techniques. Optical depth is a measure of dust-induced atmospheric opacity (optical depth 1 meaning attenuation of sunlight by a factor of 1/e).

3.5 Atmospheric Dust and Effects on Landing and Launch Vehicles

3.5.1 Introduction

Dust is probably ubiquitous on Mars. Annual dust storms introduce into the atmosphere micrometer sized particles that can remain suspended for many months. These particles, and larger ones up to tens of micrometers that precipitate faster, fall over most of the planet, and contribute a dust layer that will in time coat all surfaces if not removed later by wind or lofted again by the impact of larger particles at the surface. Large accumulations of dust over many years are expected in areas sheltered from wind. The classically bright albedo areas of Mars may be such places. Likewise, dark areas signify regions where dust is systematically removed, leaving material of larger size and visually more characteristic of the bedrock.

Generally, a significant amount of orange dust remains in suspension in the atmosphere. The airborne dust particles are estimated at <2 μm[3-10] or ≤ 3 μm.[3-11] Additionally, there is a significant amount of submicrometer size particles in suspension. The smaller particles may be

easily transported by wind or atmospheric circulation. Figure 3-9 provides estimates of the size distribution of atmospherically borne particles. One widely used size distribution is:

$$n(r) = C\, r^2 \exp[-4r/r_m]$$

where n(r) is the number density of particles of radius, r, and the mode radius, r_m, equals 0.4 μm.[3-12] The total column mass loading during a dust storm is typically 10^{-3} g cm^{-2} The single scattering properties of the particles averaged over the solar band[3-12] are the following:

Single Scattering Albedo	Average Scattering Asymmetry Parameter Cos θ	Extinction Efficiency Q_{ext}
0. 86	0. 79	2.74

The shape of the particles is unknown but, generally, it is assumed they are products of ground erosion. The dust composition is also unknown, but is likely produced by aeolian weathering of basaltic rocks similar to terrestrial palagonitic clays.

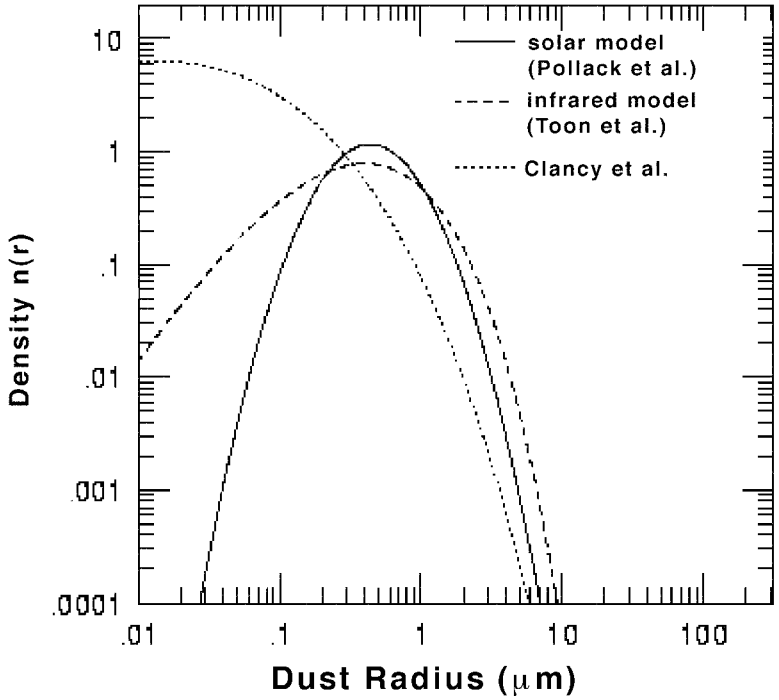

Figure 3-9. Relative Size Distribution of Airborne Dust Particles. Radius of dust particle is in micrometers.[3-12 3-13 3-14] Note the large disagreement for the smallest particles.

The amount of dust particles present in suspension in the atmosphere follows a seasonal cycle (see figure 3-8) with a clear season in northern spring and summer and a heavily dust charged season in northern autumn and winter. The seasonal change in dust occurs due to the frequency of dust storms. These phenomena range in size from dust devils meters in diameter to

hemispheric events that can on rare occasions contribute enough dust to obscure the entire planet. A dust storm "season" occurs roughly from L_s 200° to 330°, corresponding to southern spring - summer, which is also perihelion (L_s is the Sun's position—Areocentric; positive east—from the Northern Vernal Equinox; Southern Summer solstice occurs when L_s=270°). Mars' orbit is more elliptical than the Earth's, and consequently the energy deposition is significantly higher (45 percent increased insolation) during Southern Summer (section 2.4.3). The warmer surface creates stronger atmospheric dynamical behavior, including the winds necessary to raise dust.

During the clear season, the amount of dust is spatially more uniform, with an increase in the low regions and a decrease at higher altitude, due simply to the variation in total atmospheric path. During the dusty season, the space distribution of dust is more uneven, due to greater activity and higher frequency of dust events in the Southern Hemisphere.

Vertical profiles of dust quantities were measured by Mariner 9, Viking, and Mars Global Surveyor. Dust is usually well mixed within the atmosphere: abundance varies with pressure; scale height is about 10 km. Studies indicate that often in the high atmosphere there are one or more layers of thin ice clouds with dust underneath and continuing down to the ground. The top of this layer of dust may vary between 10 km at high latitudes during clear season and up to 80 km at the Equator during dusty season.

The total dust mass in the atmosphere at the peak of the 1977b storm, the largest seen by Viking, was estimated at 4×10^{14} g, based on infrared opacity mapping.[3-15 3-16] This corresponds to 4×10^{-4} g/cm^2 or a layer 1.4 μm thick.

3.5.2 Dust Storm Occurrence

Martian dust storms range greatly in size. Local and regional dust storms (table 3-1 and figure 3-11) were observed mainly in the intertropical regions or in the southern hemisphere during summer. However, storms have been seen near the northern polar cap edge in summer, and dust devils probably occur widely (section 3.4).

Dust storms tend to occur near planetary perihelion (L_S = 251°; figure 3-8). Since perihelion nearly coincides with the southern summer solstice (L_S = 270°), the resulting intense summertime radiation triggers dust storms that may last for several months. At such time, the optical depth can approach a value of five or more, adequate to obscure all surface features as seen from space or to make the Sun invisible from the surface. As many as three local storms per day may be expected in late spring (in either hemisphere) and two per day in early northern summer and midsouthern summer.[3-17] During global dust storms the atmosphere is expected to be warmer and more isothermal (approximately 200 K) to altitudes of 50 to 60 km due to direct absorption of sunlight by the dust (figure 3-15).

Table 3-1. Classification of Martian Dust Storms. Local dust storms are shorter in duration than great dust storms and may not have the "explosive" expansion phase of the great ones. Great dust storms form a continuum that can be subdivided into Type A (large), Type AB (circle globe) and Type B (cover globe).[3-18]

TYPE	Range for Latitude of Origin (deg)	Season of Origin (L_s in deg)	Typical Duration (Earth days)	Typical Extent (km)	Other Remarks
LOCAL	+70° to –75°	All	4 -10	100	No rapid expansion
Type A	+50° to –60°	192° <L_s < 310° (110°, 163° rare)	70	2500	Expansion East-West
Type AB	-20° to –60°	205°	90	20 000	Circle globe
Type B	-20° to -60°	250° < L_s <310°	100	GLOBAL	Cover globe

The global storms over the years do not occur with any regularity. Global storms were observed in 1956, 1971/72, 1973, 1977, 1978, and 1982. Smaller storms were observed in 1922, 1924, 1943, 1958, and 1971 (figure 3-8). Years with two storms and no storms have been observed. After a storm normal conditions resume in 50 to 100 days. The likelihood of a dust storm occurring at a given Mars landing site on a given date cannot be made with any more accuracy than a prediction of a storm for a specific location and time on Earth. However, table 3-2 created for Mars Observer, indicates that it is possible to estimate the probability of a globe-covering storm. Although the truly global storm encountered by Mariner 9 was more severe, the Viking mission encountered the worst dust season on record.[3-18] Should a global storm coincide with a Mars encounter for a manned mission, the impact of the storm on descent control (due to atmospheric changes) may necessitate a delay in the scheduled landing. Some idea of the seasonal and location variation of local type dust storms is provided, respectively, by figures 3-10 and 3-11.

Table 3-2. Predictions of Martian Dust Storms for Mars Observer Mission. See Table 3-1 for explanation of storm types. Storms from 1956 to mid 1988 are used for statistics (1977a is used once for Type A and once for Type B; 1982b is used as a 6th Type B). Local storm predictions are for a mean environment. Predictions of two great storms are an 80% confidence estimate for the period 1956 to 1986 and a 95% confidence estimate for the period 1977 to 1986.[3-18]

Time Interval In MO Mission	Storm Type	Anticipated Number (Range of Dates)	Remarks
Drift Orbit Period + 10 days			
Aug. 13, '93	Local	~20	
to	A	None	7% chance (1 in 15 Mars Yr.)
Dec. 16, '93	B	None	
Mapping Orbit (Mission)			
Dec. 16, '93	Local	~135	
to	A	1 (Dec. 30, '93-	40% chance (6 in 15 Mars Yr.)
Oct. 14, '95	B	1 Jul. 10, '94)	40% chance (6 in 15 Mars Yr.)
	both A and B	1 worst case	20% chance (3 in 15 Mars Yr.)
Beginning of extended Mission			
Oct. 16, '95	Local	~37	
to	A	1 (Nov. 18, '95-	40% chance (6 in 15 Mars Yr.)
May 25, '96	B	1 May 25, '96)	40% chance (6 in 15 Mars Yr.)
	both A and B	1 worst case	20% chance (3 in 15 Mars Yr.)

** 135 is Martian yearly average count of local storms seen from the Earth 1965-1984

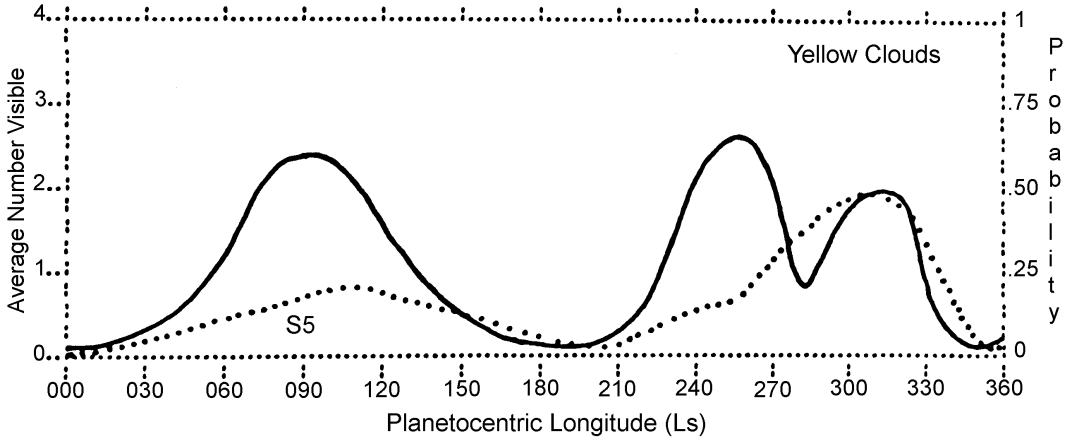

Figure 3-10. Graphs of seasonal indices for Yellow Clouds (solid line; left-hand scale) and probability of observing them (dotted line; right-hand scale). Graphs are based on observations for the opposition years 1969, 1971, 1973, 1975, 1978, 1980, 1982, and 1984. "SS" Indicates Northern Summer Solstice. Yellow Clouds are local dust storms.[3-19]

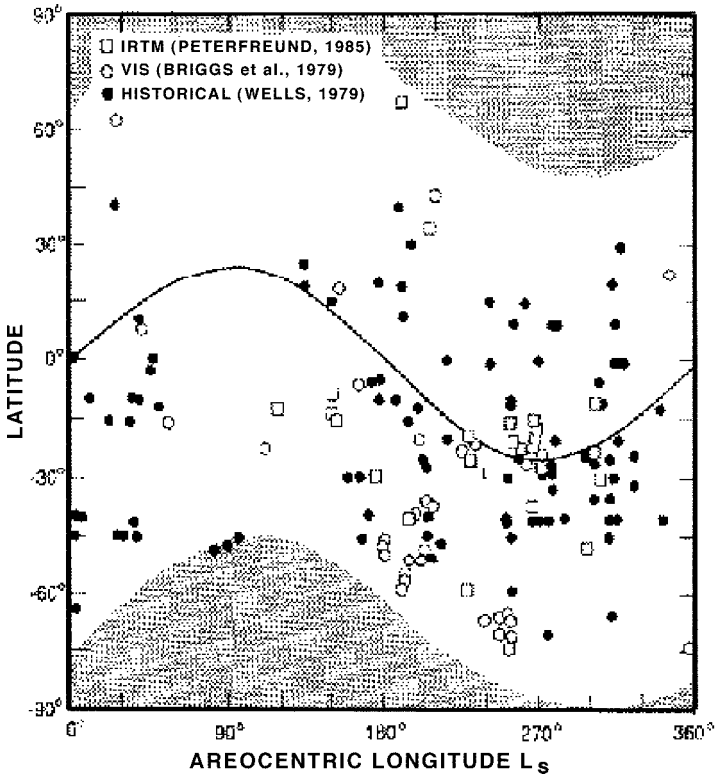

Figure 3-11. Local dust storms detected by the Viking orbiters.[3-19] Latitude and time-of-year occurrence of local dust storms detected by the Viking Orbiters from either infrared or visible imaging observations, and those observed from Earth compiled by reference Wells.[3-20] Solid line represents the sub-solar latitude. (Figures taken from Kahn et al., 1992[3-21] as copied from Peterfreund, 1985.[3-19])

3.5.3 Surface Phenomena

The vast annual dust storms produce little erosion but redistribute fine debris. Produced by very slow erosion rates, a surface layer varying from meters to tens of meters thick has been redistributed around Mars. This layer likely consists of sand and dust size particles entrained and moved by the wind.[3-22] The Viking data indicate a particle size distribution of less than 1 to 10 micrometers.[3-23] Ground operations may also be inhibited by motion of material from local wind activity quite independent of the storms. The wind driven debris zone near the surface is believed to be very thin, ranging from a few millimeters to centimeters.[3-34] Particles in motion should not exceed a few mm in size. If fine dust is present locally, it can be lofted by this process. Creep of sand-sized particles may also be an important consideration.

Martian dust storm fronts are perhaps similar to those in the American southwest. While Martian wind speeds may exceed terrestrial winds, the density of the Martian air at the surface is 100 to 120 times less. The pressure of winds is roughly proportional to air density times wind velocity squared.[3-34] Winds measured by the Viking and Pathfinder landers are unlikely to be worst cases since they were purposefully landed in relatively flat terrain. Nighttime downslope winds in many sloping areas of Mars could be in the 30 to 40 m/s range. Such velocities, with their associated dust-raising capability, are required to explain the abundant streak patterns in the surface albedo.

3.5.4 Engineering Properties

The ability of airborne dust to enter mechanisms and cause wear was studied in the Mars Pathfinder Wheel Abrasion Experiment. Strips of aluminum with metallic coatings of different thickness and hardness were attached to the right central wheel of the Sojourner rover. The dust grain size (diameter) suggested by clogging of dust in a cleated wheel was less than 40 μm and less than 30 μm from abrasive characteristics. Electrostatic charging inferred a dust grain size of <20-36 μm. Abrasion was most pronounced on aluminum—the softest metal sample.[3-24] The fine size of the airborne dust may require special filtration mechanisms. The oxidizing properties of the dust, perhaps due to activation by solar UV, and the liberation of oxygen upon exposure to water, may cause special chemical concerns for dust in contact with seals, filters, optics, and biological materials. Dusty environments pose an added risk upon landing when a radar reflective surface is required to measure closing velocity. A very dusty landing area could raise a dust plume that would coat instruments and hardware.[3-25]

3.5.5 Electric Power Generation

One significant impact of atmospheric aerosols (e.g., dust) on a manned mission to Mars is the potential effect on solar panels. The Mars Pathfinder lander successfully demonstrated the use of photovoltaic arrays on the Martian surface. The significantly smaller Sun - Mars distance at perihelion with its advantage for solar power, is offset by the typically greater dust abundance of the atmosphere at that time.

Figure 3-12 shows that the atmosphere of Mars carries a significant amount of suspended dust—the amount varying with the occurrence of dust storms. The light color of the sky in this image is due to scattering of sunlight by dust particles suspended in the atmosphere. Dust reduces the intensity of sunlight reaching the surface. A reduction of the blue light component may influence the optimum choice of solar cell materials.

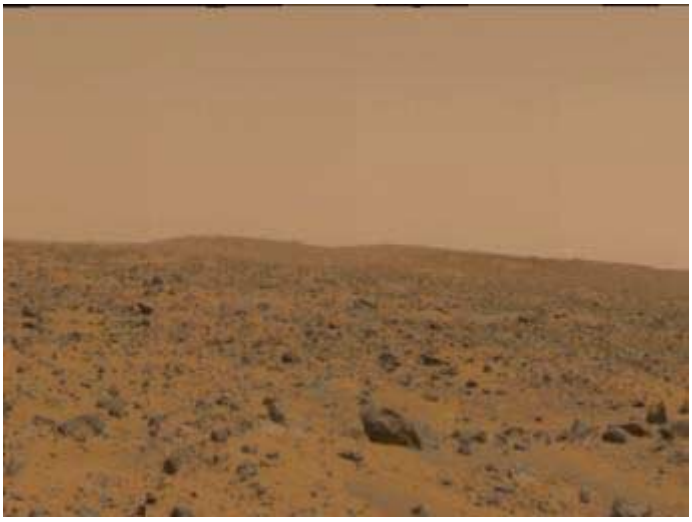

Figure 3-12. Martian Landscape as Viewed by the Mars Pathfinder Lander. For a color version of this figure, contact *jere.justus@msfc.nasa.gov* to get a portable data format (PDF) of this report.

The amount of dust in the atmosphere characterized by the optical depth τ (the exponent in the equation $I = I_0 \exp^{-\tau}$, where I is the intensity compared to the above-atmosphere value I_0),

can vary from less than 0.4 to values greater than 5, depending on the season, latitude, and presence of dust storms. Passage of light through the dust layer also affects the spectrum of light at the surface. Dust provides the greatest attenuation of light at short wavelengths. Figure 3-13 shows the spectral transmission of the atmosphere calculated using a simplified model of dust properties. Note that UV intensity may not be reduced as much as the blue (section 4.6).

Reduction in the blue light content may favor use of solar cell materials that respond better to the red and infrared, i.e., lower bandgap semiconductors which are also more suitable to lower-than-Earth-normal temperatures. Also, the best choice of solar cell for producing power during the seasonal global dust storm may be quite different from the optimum technology during clear periods.[3-26 3-27] During a relatively clear day (optical depth is low) most of the total sunlight reaching the surface is direct, allowing the use of light concentration devices.[3-28] With high dust opacities, virtually all the light is diffuse and a concentrator has no advantage. A solar power source designed for use at the poles would benefit from around-the-clock daylight during the summer months.

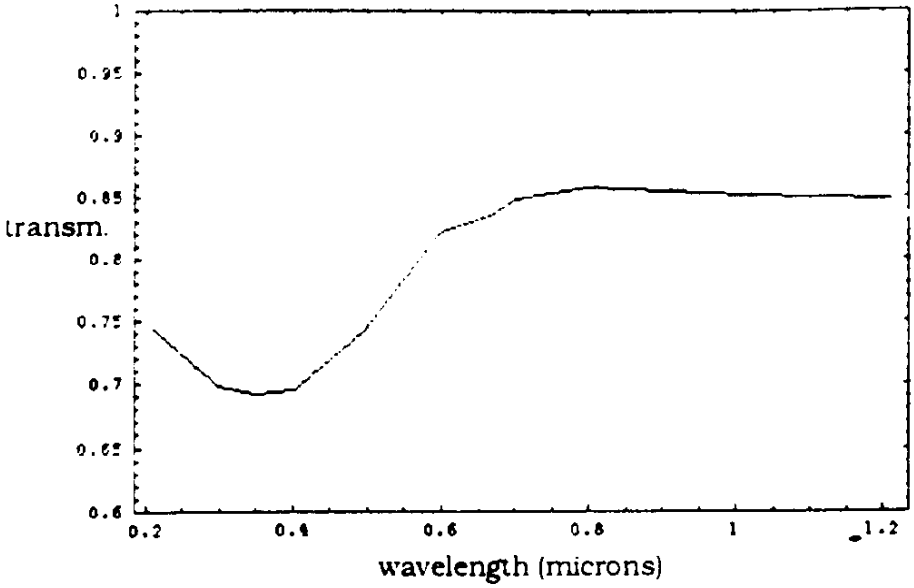

Figure 3-13. Transmission of the Mars Atmosphere From 0.2 to 1.2 Micrometers. Transmission calculated at zenith angle of 0 (sun directly overhead) for $\tau = 1$.[3-28]

Atmospheric dust on Mars can take months to settle out of the atmosphere and deposit onto horizontal surfaces. This potentially limits the operating lifetime of a solar array on Mars unless a technique is developed to remove the dust periodically. The Mars Pathfinder mission (figure 3-14) indicated a dust coverage rate that lead to a 0.3 percent power loss per day. This is consistent with calculated values for dust deposition based on the available dust properties measured from Viking and Mariner.[3-28]

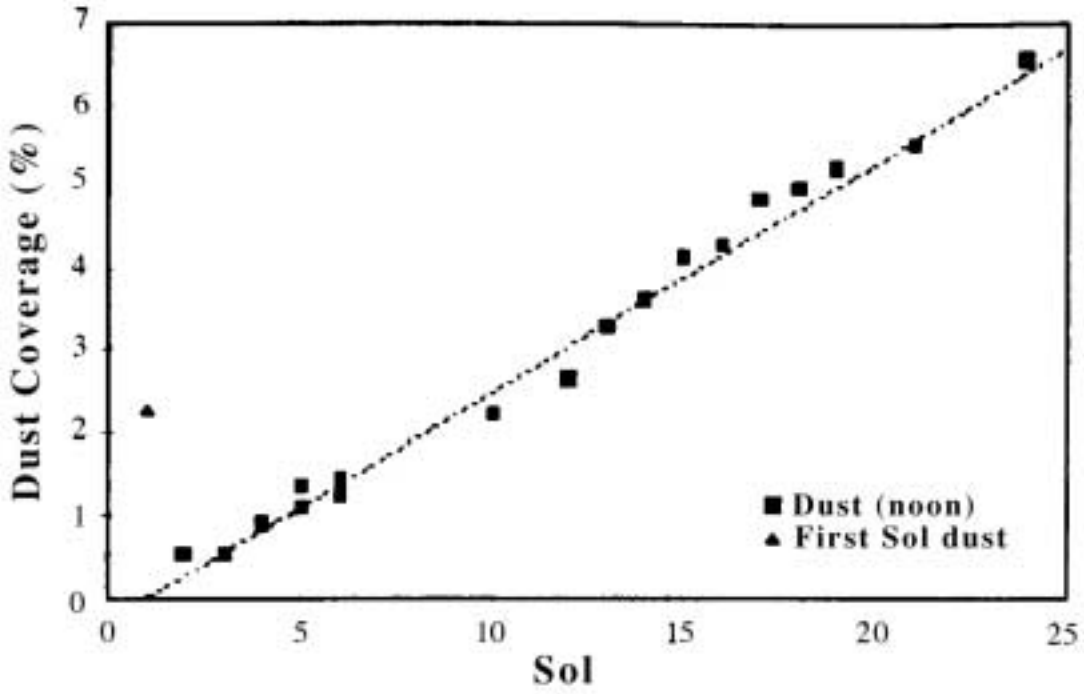

Figure 3-14. Dust Coverage of the Sojourner Rover Solar Array. Data measured from the MAE experiment on the Rover.[3-28]

3.6 Dust Effects on Temperature and Density

3.6.1 Temperature and Winds

Vertical variation of temperature is controlled by the adiabatic lapse rate, $\Gamma = g/C_p$, where g is gravity and C_p is specific heat. Because of lower gravity on Mars, Γ is about half the value for Earth's atmosphere, so temperature decreases less rapidly with altitude on Mars than on Earth. Lacking substantial amounts of ozone, Mars' middle atmosphere does not undergo significant heating, and so lacks a warm middle atmosphere region analogous to the upper stratosphere and lower mesosphere of Earth. Instead, Mars' atmospheric temperature tends to decrease with altitude above the surface until it begins to increase again near 100 to 120 km (the thermosphere, analogous to Earth's thermosphere).

Thermal wind relations are expected to play a large role in determining winds aloft. In zones with large North-South temperature gradients (such as near polar cap edges), winds aloft greater than 100 m/s are inferred[3-29] but have not yet been measured directly. Changes in temperature patterns caused by dust storms are thus expected to have considerable effect on both temperature gradients and winds (section 3.4.2).

3.6.2 Dust Effects on Density

Because of its low density, a given volume of Mars' atmosphere has low inertia, and thus responds more sensitively to mechanical forcing (such as topographic influence on winds) than does Earth's atmosphere. Similarly, low density on Mars means that a given volume of atmosphere has lower heat capacity and responds more readily to given thermal forcing. Strong,

sudden effects of atmospheric warming by a developing regional dust storm are illustrated in figure 3-15 and shows that the 1997 Noachis storm, observed by Mars Global Surveyor (MGS), produced about 10 °C warming at 30 km and 20 °C warming at 50 km (at the same location and time of day) over just four days. Figure 3-16 shows that corresponding changes in atmospheric density, induced by the Noachis storm over four days, range from 25 percent near the surface to over 125 percent at 70 km.

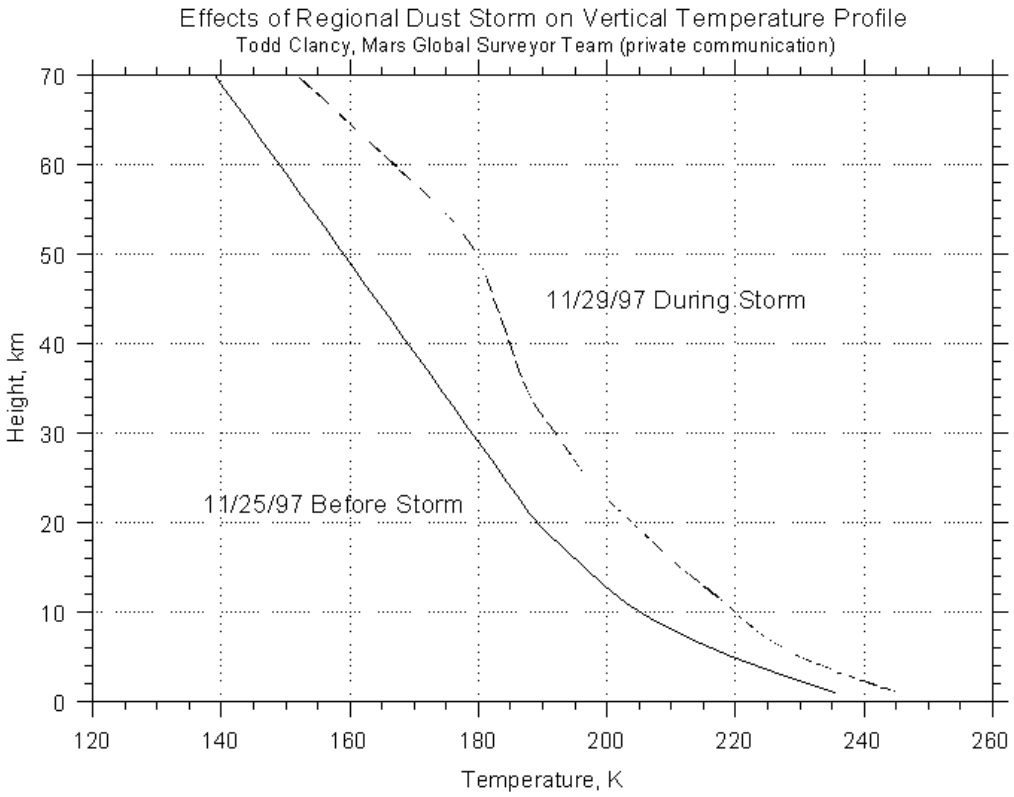

Figure 3-15. Effects of the regional-scale Noachis dust storm on temperature over a four-day period, measured by ground-based microwave techniques (Todd Clancy, private communication).

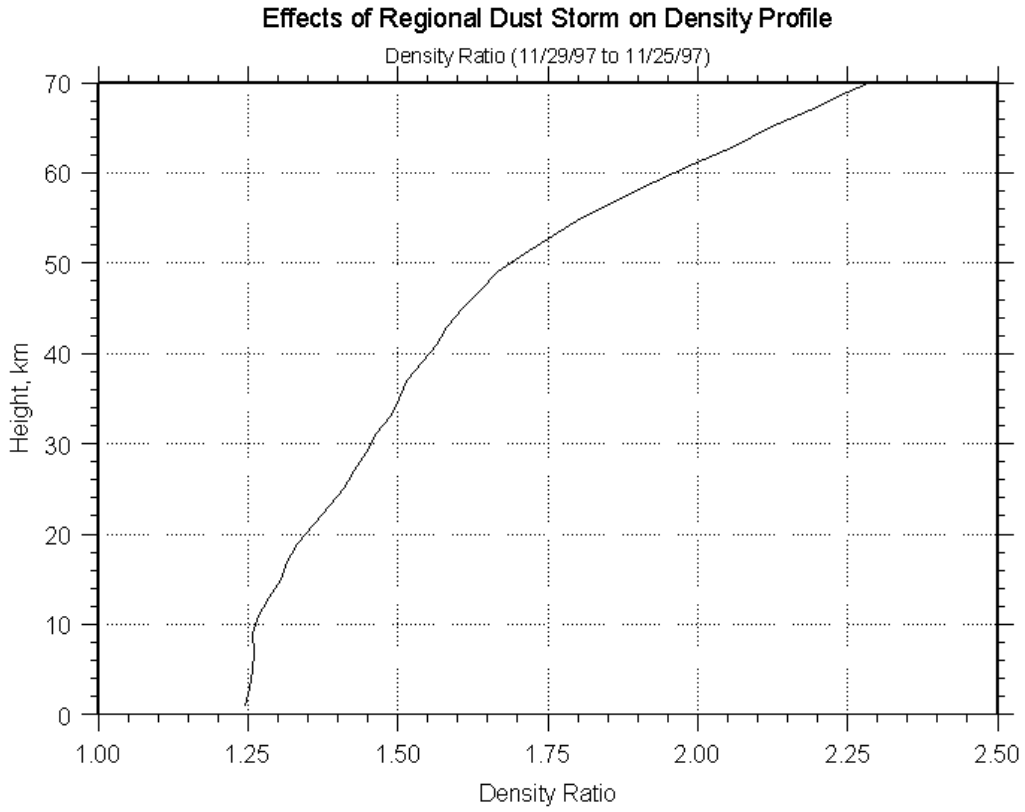

Figure 3-16. Dust-storm-induced changes in atmospheric density over the same period in Figure 3-15 (Todd Clancy, private communication).

Despite the fact that the Noachis storm remained only regional in size (primary enhanced atmospheric dust was confined to middle southern latitudes), dust effects were observed by MGS at essentially all latitudes and altitudes. Figure 3-17 shows that increases in atmospheric pressure (and density) observed by the MGS accelerometer instrument[3-30] were even larger at 126 km and at middle northern latitudes than those observed in Clancy's ground-based microwave data for 61-km altitude in middle southern latitudes. Large density effects were seen to at least 160-km altitude by MGS accelerometer measurements.

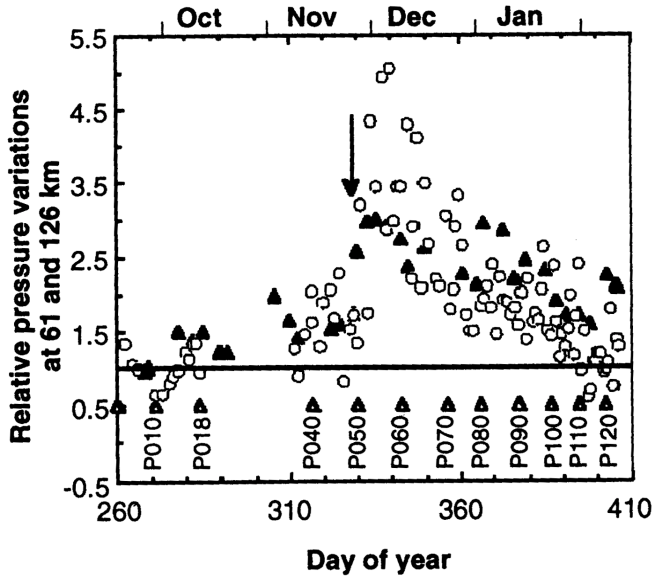

Figure 3-17. Effects of the Noachis dust storm on atmospheric pressure at 61-km altitude (ground-based microwave data; triangles) and at 126 km (MGS accelerometer data, circles).

Even in the absence of major amounts of dust, large variations in atmospheric density occur, especially at 75 km and above, over various seasons and times of day. Figure 3-18 shows as much as a factor of five change in density between Mars Pathfinder entry and density measured by Mars Global Surveyor during aerobraking operations.

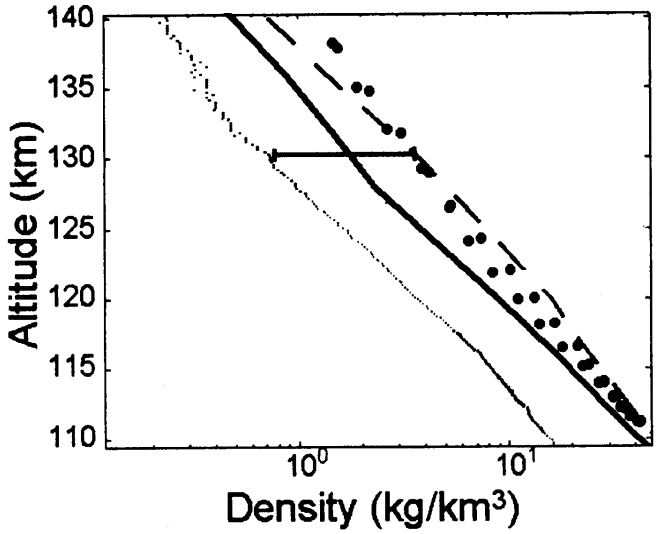

Figure 3-18. Atmospheric densities measured at various times of day and seasons by Viking 1 (dashed line), Viking 2 (solid line), Pathfinder (dotted line), and Mars Global Surveyor (circles) under relatively dust-free conditions.

3.7 Density Waves at Aerobraking Altitudes

Mars Global Surveyor (MGS) used aerobraking to lower periapsis altitude of its initial, highly-elliptical, capture orbit into a nearly-circular, operational, mapping orbit. Having a sun-synchronous orbit, the spacecraft returns to nearly the same local time and latitude on each periapsis pass. However, longitude of periapsis varies significantly from orbit to orbit. An unexpected longitude dependence in atmospheric density was observed by an accelerometer onboard MGS.[3-30] Figure 3-19 shows atmospheric density relative to Mars-GRAM[3-6] model value for MGS orbits 946 to 997. Density values (at essentially the same latitude and local time) varied more than a factor of three as longitude varied during this observing period. At this time and latitude region, the longitude-dependent waves were dominated by a wave-2 pattern (2 wave peaks over 0 to 360 longitude range). At other periods during its aerobraking operations, MGS-observed longitude-dependent waves were predominantly wave-3 pattern.

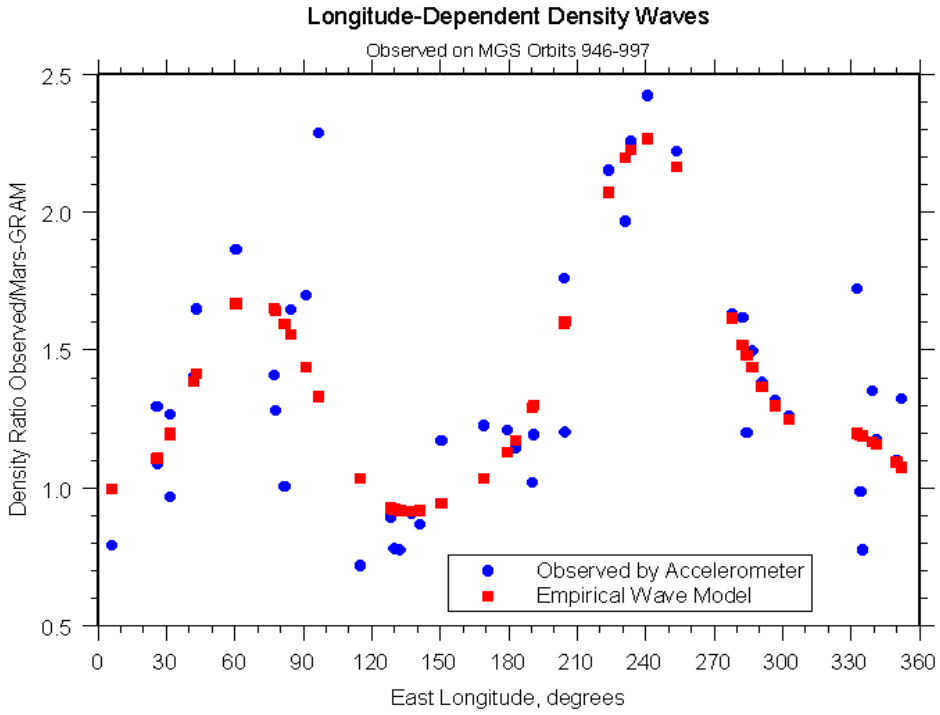

Figure 3-19. Longitude-dependent waves of atmospheric density observed by Mars Global Surveyor on successive periapsis passes for orbits 946-997. Density is plotted as ratio of observed value to Mars-GRAM[3-6] model expected value at periapsis.

3.8 Solar Influence on Mars Atmosphere

3.8.1 Solar Wind

Since Mars has no appreciable planetary magnetic field,[3-31] interaction of the solar wind with Mars is much like that for Venus or an active comet. The ionosphere and neutral atmosphere of Mars act as an obstacle to flow of the solar wind stream and produce a bow shock (figure 3-20). Location of this bow shock appears to be independent of upstream dynamic pressure. Although there is speculation that its position may depend on solar Extreme Ultraviolet (EUV), no distinct dependence on solar activity has been discerned. With no planetary magnetic

field, there is no "focusing" of solar wind charged particles into polar regions (hence no auroras on Mars). As a consequence, many of the observed complexities of Earth's polar ionosphere and thermosphere are not expected on Mars.

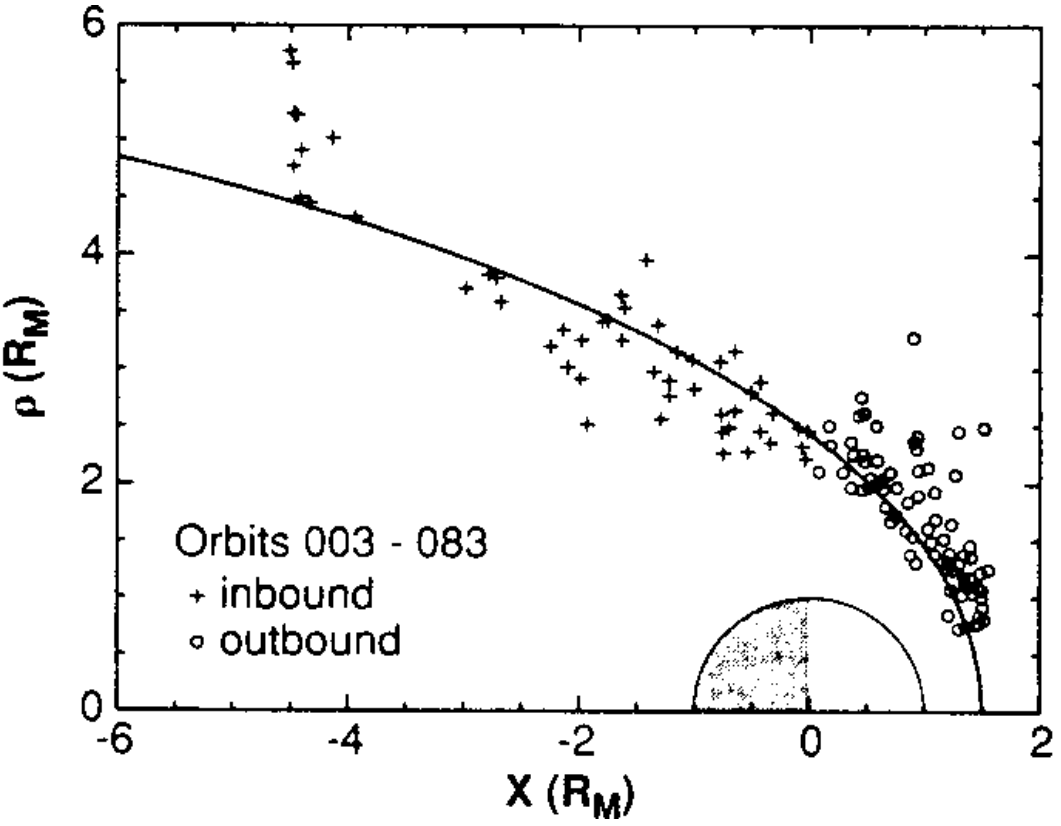

Figure 3-20. Location of Mars bow shock observed by Mars Global Surveyor.[3-31]

3.8.2 Extreme Ultraviolet (EUV)

As with Earth, the primary mechanism for heating the thermosphere of Mars (above about 120 km) is absorption of solar EUV and X-rays. Since there are no regular observations of interplanetary EUV or X-ray flux, effects of this radiation are usually parameterized in terms of dependence on the flux of 10.7 cm solar radio noise ($F_{10.7}$). Figure 3-21 shows observed dependence of Mars exospheric temperature (temperature at the upper levels of the thermosphere) on $F_{10.7}$. Whereas, exospheric temperature on Mars varies between about 150 K and 400 K, Earth's exospheric temperature varies from about 600 K to 1200 K over the range of solar flux encountered.

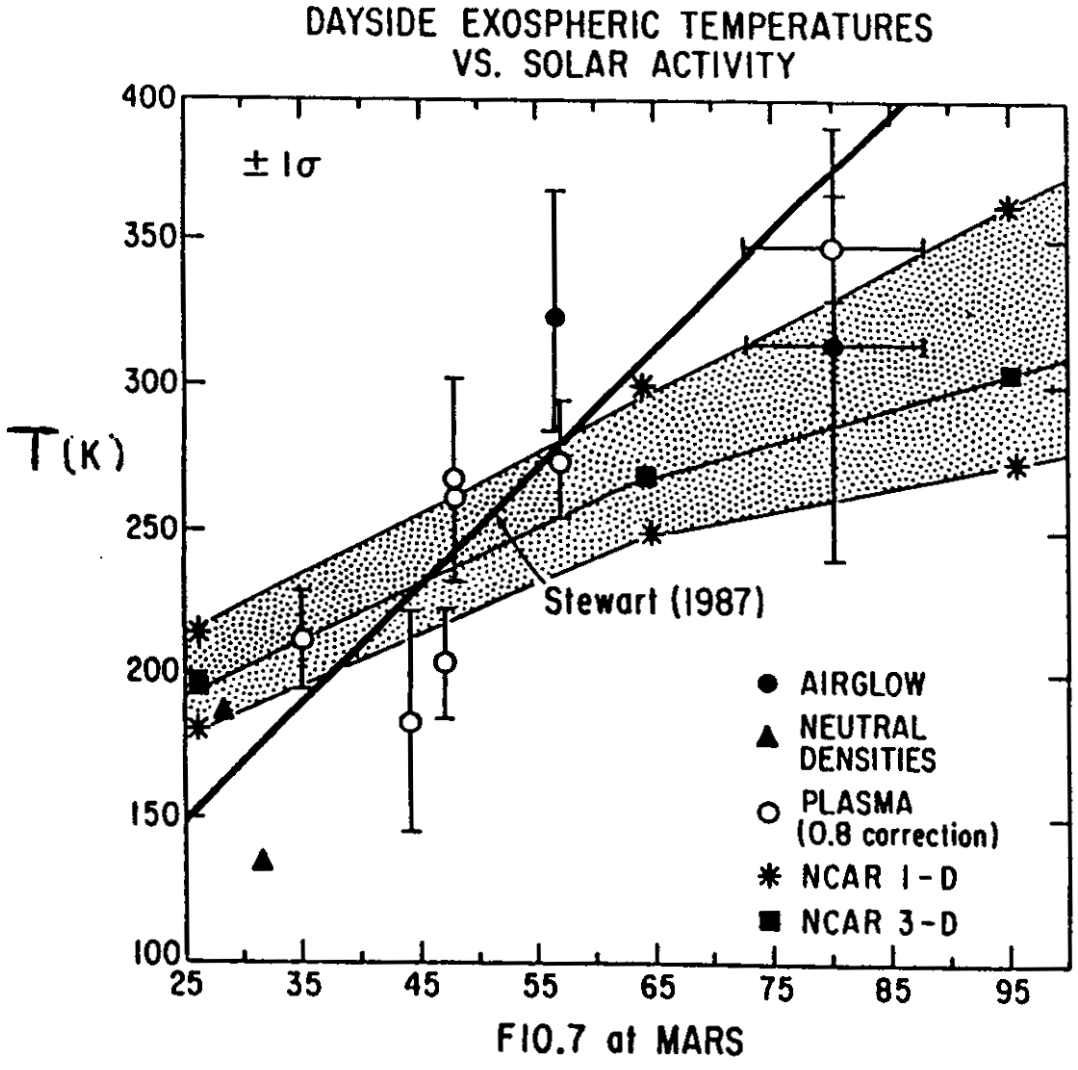

Figure 3-21. Exospheric temperature for Mars versus 10.7 cm solar radio noise flux adjusted to Mars orbital position.[3-32]

3.8.3 Ionosphere

Both ions and electrons in the Mars ionosphere have their peak concentration near 130-km altitude (figure 3-22). There is no clear evidence that the altitude of the electron peak has any dependence on EUV (or $F_{10.7}$). However, it does depend on orbital position of Mars from the Sun (electron peak is at lower altitude when Mars is further from the Sun).

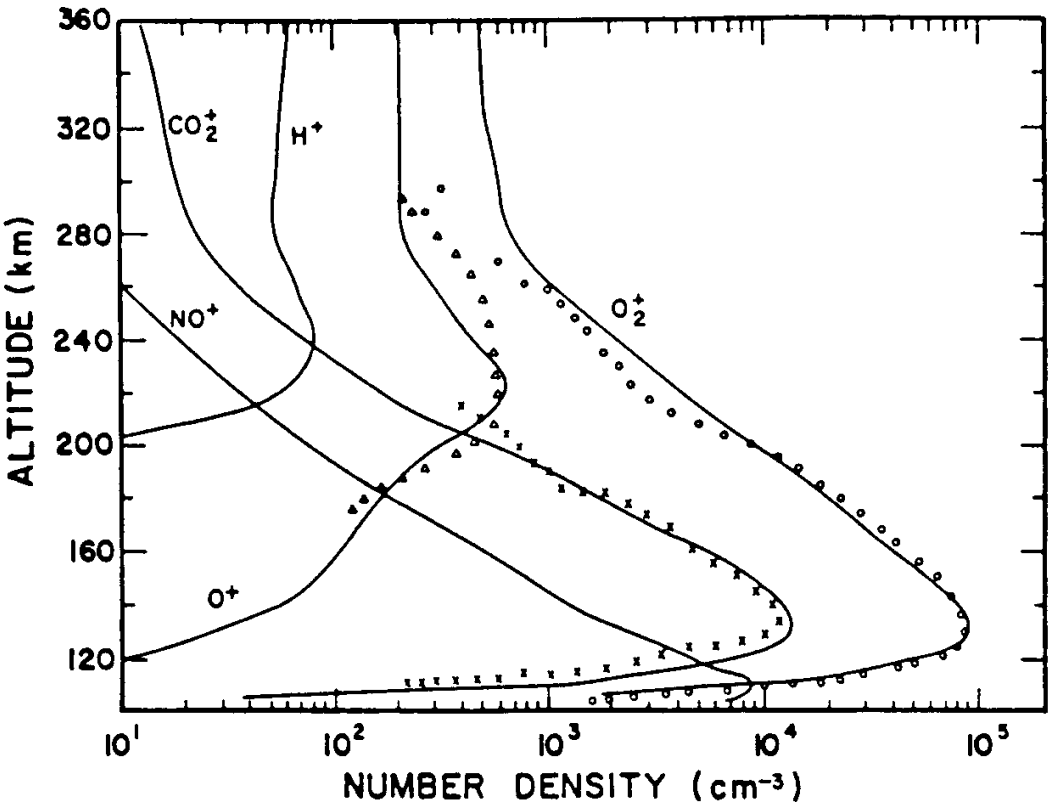

Figure 3-22. Ion density profiles in Mars dayside ionosphere.[3-33] Solid lines are modeled values. Symbols are Viking orbiter data.

3.9 References

3-1 Golombek, M. P., Cook, R. A., Moore, H. J., and Parker, T. J.: "Selection of the Mars Pathfinder landing site." *J. Geophys. Res*, Vol. 102, No. E2, pp. 3967-3988, 1997.

3-2 Zurek, R.W., Barnes, J.R., Haberle, R.M., Pollack, J.B., Tillman, J.E., and Leovy, C.B.: "Dynamics of the Atmosphere of Mars" in Mars, Kieffer, H. H., Jakosky, B. M., Synder, C. W., Mathews, M. S. (eds): Univ. of Arizona Press, Tucson, pp. 835-933, 1992.

3-3 Michaux, C. M. and Newburn, Jr., R. L.: "Mars Scientific Model." JPL Document 606-1, NASA Jet Propulsion Laboratory, Pasadena, CA, 1972.

3-4 Carr, M.H.: The Surface of Mars. Yale University Press, New Haven, p. 19, 1981

3-5 Schofield, J. T., Barnes, J. R., Crisp, D., Haberle, R. M., Larsen, S., Malgalhaes, J. A., Murphy, J. R., Seiff, A., and Wilson, G.: "The Mars Pathfinder Atmospheric Structure Investigation/Meteorology (ASI/MET) Experiment." *Science*, Vol. 278, pp. 1752-1758, 1997.

3-6 Justus, C. G.: "Mars Global Reference Atmospheric Model for Mission Planning and Analysis." *J. Spacecraft and Rockets*, Vol. 28, No. 2, pp. 216-221, 1991.

3-7 Ryan, J.A. and Henry, R. M.: "Mars Atmospheric Phenomena During Major Dust Storms as Measured at the Surface." *J. Geophys. Res.*, Vol. 84, pp. 2821-2819, 1979.

3-8 Tillman, J. E.: "Mars Temperature Overview." University of Washington, at http://mars.ivv.nasa.gov/k12/resources/mars_datainformation/temperature_overview.html.

3-9 Zurek, R. W.: "Martian Great Dust Storms: An Update." *Icarus*, Vol. 50, pp. 288-310, 1982.

3-10 Pollack, J. B., Ockert-Bell, M. E., and Shepard, M. K.: "Viking Lander Image Analysis of Martian Atmospheric Dust." *J. Geophys. Res*., Vol. 100, pp.5235-5250, 1995.

3-11 Bell, J. F. and Ockert-Bell, M. E.: "Physical, Compositional, and Radiative Properties of Martian Dust." Eos Trans, AGU 79(45) Fall Meet. Suppl., F527, 1998.

3-12 Pollack , J. B., Colburn, D. S., Flasar, F. M., Kahn, R., Carlston, C. E., and Pidek, D.: "Properties and Effects of Dust Particles Suspended in the Martian Atmosphere." *J. Geophys. Res.*, Vol. 84, pp. 2929- 2945, 1979.

3-13 Toon, O. B., Pollack, J. B., and Sagan, C.: "Physical Properties of the Particles Composing the Martian Dust Storm of 1971-1972." *Icarus*, Vol. 30, pp. 663-696, 1977.

3-14 Clancy, R. T., Lee, S. W., Gladstone, G. R., McMillan, W. W., and Rousch, T.: "A New Model for Mars Atmospheric Dust Based Upon Analysis of Ultraviolet Through Infrared Observations from Mariner 9, Viking, and Phobos." *J. Geophys. Res*., Vol. 100, No. E3, pp. 5251-5263, 1995.

3-15 Martin, T. Z. and Richardson, M.: "New Dust Opacity Mapping from Viking IR Thermal Mapper Data." *JGR Planets*, Vol. 98, p. 10941, 1993.

3-16 Martin, T. Z.: "Mass of Dust in the Mars Atmosphere." *JGR Planets*, Vol. 100, p. 7509, 1995.

3-17 Beish, J., et al.: "Exploring Mars in 1988." *Sky and Telescope*, 1988.

3-18 Evans, R.: "Mars Atmosphere Dust-Storm Occurrence Estimate for Mars Observer." NASA Jet Propulsion Laboratory memo No. 5137-87-124, 1988.

3-19 Peterfreund, A. R.: "Contemporary Aeolian Processes on Mars: Local Dust Storms." Arizona State University, Ph.D. thesis, 1985.

3-20 Wells, R. A.: Geophysics of Mars. Amsterdam: Elsevier, 1979.

3-21 Kahn, R., Martin, T., Zurek, R., and Lee, S.: "The Martian Dust Cycle" in Mars Kieffer, H. H., Jakosky, B. M., Snyder, C. W., and Matthews, M. S. (eds.): Univ. of Arizona Press, Tucson, pp. 1017-1053, 1992.

3-22 Christensen, P. R. and Moore, H. J.: "The Martian Surface Layer" in Mars, Kieffer, H. H., Jakosky, B. M., Synder, C. W., Mathews, M. S. (eds): Univ. of Arizona Press, Tucson, pp. 686-729, 1992.

3-23 Arvidson, R. E., Gooding, J. L., and Moore, H. J.: "The Martian Surface as Imaged, Sampled, and Analyzed by the Viking Landers." *Rev. Geophys. Space Phys.*, Vol. 27, pp. 39-60, 1989.

3-24 Ferguson, D. C., Kolecki, J. C., Siebert, M. W., Wilt, D. M., and Matijevic, J. R.: "Evidence for Martian Electrostatic Charging and Abrasive Wheel Wear from the Wheel Abrasion Experiment on the Pathfinder Sojourner Rover." *J. Geophys. Res.*, Vol. 104, No. E4, pp. 8747-8789, 1999.

3-25 Golombek, M. P., Moore, H. J., Haldemann, A. F. C., Parker, T. J., and Schofield, J. T.: "Assessment of Mars Pathfinder Landing Site Predictions." *J. Geophys. Res.*, Vol. 104, No. E4, pp. 8585-8594, 1999.

3-26 Appelbaum, J. and Landis, G. A.: "Photovoltaic Arrays for Martian Surface Power." *Acta Astronaut*, Vol. 30, pp. 127-142, 1993.

3-27 Matz, E., Appelbaum, J., and Taitel, Y.: "Solar Cell Temperature on Mars." *J. Propul. Power*, Vol. 14, No. 1, pp. 119-125, 1998.

3-28 Landis, G. A.: "Solar Cells on Mars." Proceedings of the 3rd International Workshop on Radiation Effects on Semiconductor Devices for Space Application, 1998.

3-29 Christensen, P. R., Anderson, D. L., Chase, S. C., et al.: "Results from the Mars Global Surveyor Thermal Emission Spectrometer." *Science*, Vol. 279, No. 5357, pp. 1692-1698, 1998.

3-30 Keating, G. M., Bougher, S. W., Zurek, R. W., et al.: "The Structure of the Upper Atmosphere of Mars: In situ Accelerometer Measurements from Mars Global Surveyor." *Science*, Vol. 279, No. 5357, pp. 1672-1676, 1998.

3-31 Acuna, M. H., Connerney, J. E. P., Wasilewski, P., et al.: "Magnetic Field and Plasma Observations at Mars: Initial Results of the Mars Global Surveyor Mission." *Science*, Vol. 279, No. 5357, pp. 1676-1685, 1998.

3-32 Bougher, S. W., Roble, R. G., Ridley, E. C., et al.: "The Mars Thermosphere. II. General Circulation with Coupled Dynamics and Composition." *J. Geophys. Res.*, Vol. 95, pp. 14811-14827, 1990.

3-33 Chen, R. H., Cravens, T. E. and Nagy, A. F.: "The Martian Ionosphere in Light of the Viking Observations." *J. Geophys. Res.*, Vol. 83, pp. 3871-3876, 1978.

3-34 Smith, R. E. and West, G. S., compilers: "Space and Planetary Environment for Use in Space Vehicle Development, 1982 Revision (Volume 1)." NASA TM 82478, 1983.

4.0 MARS SURFACE ENVIRONMENT

4.1 Principal Surface Features

4.1.1 Global Topography

Although Mars is about half the size of Earth, the land surface area of the two planets is nearly equivalent. The Southern Hemisphere of Mars is predominantly ancient cratered highlands somewhat similar to the Moon. In contrast, most of the Northern Hemisphere consists of plains which are much younger and lower in elevation. The global topography of Mars (figure 4-1) shows several large scale features: the Tharsis Bulge (near the equator and 250ºE), the large southern basins of Hellas and Argyre (near 40ºS and longitudes 70ºE and 320ºE, respectively), and the huge equatorial canyons comprising Valles Marineris (longitudes 260ºE to 330ºE) just east of the Tharsis summit. The distribution of craters is asymmetrical over the planet. The northern third is relatively lightly cratered; the southern two-thirds is heavily cratered. Light cratering of the north implies it is a younger region with a different crustal type or thickness.

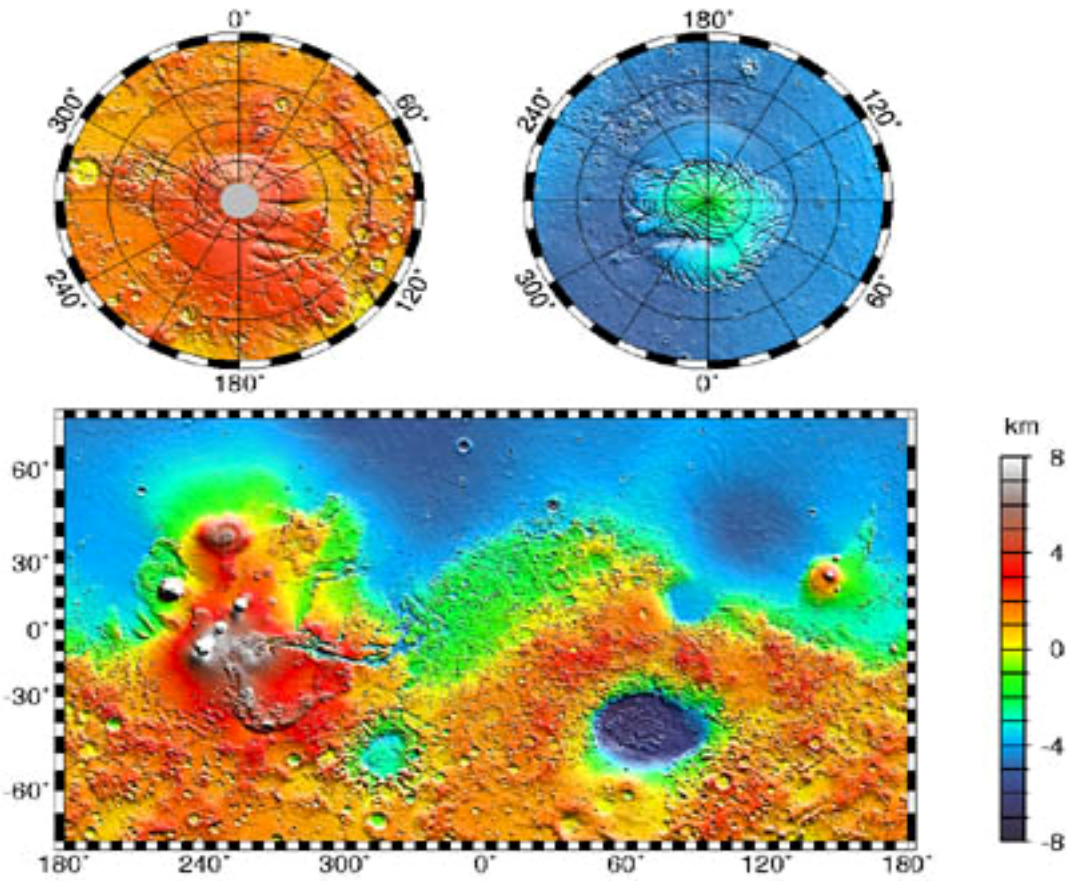

Figure 4-1. Mars Topography from MGS MOLA Experiment.[4-1] For a color version of this figure, contact *jere.justus@msfc.nasa.gov* to get a portable data format (PDF) of this report.

Surprisingly, we now know more about the topography of Mars than about many continental regions on Earth. Mars Global Surveyor (MGS) provided high resolution elevation maps with precise details on potential landing and exploration sites. The Mars Orbiter Laser

Altimeter (MOLA) on MGS provides topographic data with a vertical resolution up to approximately 30 centimeters with along-track spatial resolution of 300 to 400 meters.[4-2] The MOLA database with its tens of millions of elevation measurements reduced substantially the level of topographic uncertainty. Characterization of Martian surface features is expected to improve as these data are analyzed.

Martian topography plays an important role in determining a landing site. In particular, the capabilities of a spacecraft's entry, descent, and landing subsystem (aeroshell, parachute, etc.) constrain the maximum elevation of a landing site. As an example, the Mars Pathfinder spacecraft used accelerometers and a special-purpose algorithm to determine when to deploy the parachute. Since the lander descended about four kilometers after deployment before the backshell separated, the maximum ground elevation had to be less than zero kilometers (with respect to reference datum level) to give adequate performance margin in worst-case conditions.[4-3] In general, during a landing approach a radar altimeter might trigger retro-rockets too early or too late for a safe landing when the spacecraft's horizontal drift carries it to a steep drop-off or a steep rise. For a three-legged lander design such as the Mars Surveyor, surface slope cannot exceed 16 degrees, or a maximum of 10 degrees when allowing for a 6 degrees tilt during maximum leg crush during lander impact.[4-3]

4.1.2 Geomorphology

Like Mercury and the Moon, Mars appears at present to lack active plate tectonics. There is no evidence of recent horizontal motion of the surface such as the folded mountains so common on Earth. With no lateral plate motion, hot spots under the crust stay in a fixed position relative to the surface. This may account for the Tharsis bulge and its enormous volcanoes. There is, however, no evidence of current volcanic activity. Very clear evidence exists of ancient erosion on Mars in the form of valley networks caused by fluid flow and outflow channels.

4.1.3 Surface Topography and Gravity

Data from Viking was sufficient to produce reasonably accurate estimates of surface topography (figure 4-2) and its effect on surface gravity (figure 4-3). Precision orbital observations from Mars Global Surveyor and its laser altimeter instrument are improving this information. One presently unknown effect of topography and gravity is its influence on large topographically-fixed atmospheric density variations seen by the aerobraking Mars Global Surveyor.[4-4] (section 3.7)

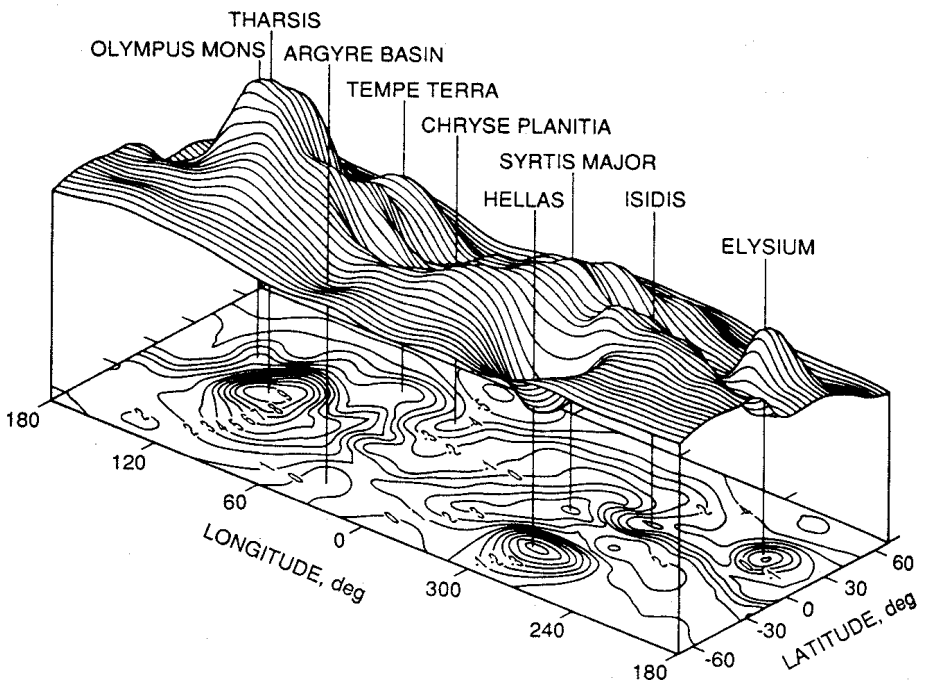

Figure 4-2. Mars topography represented by the 16 × 16 field of Bills and Ferrari (1978).[4-5]

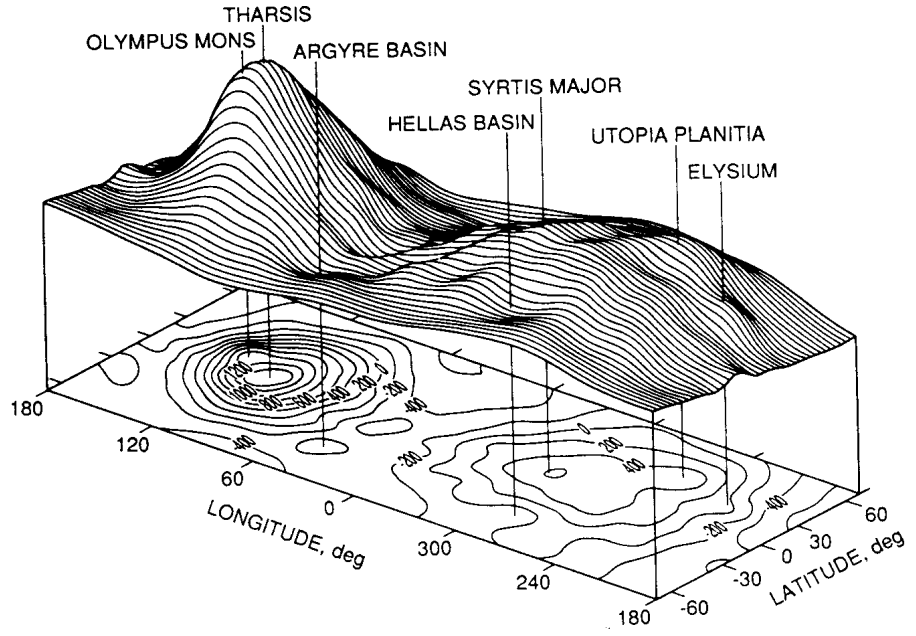

Figure 4-3. Mars geoid deduced from the gravity model of Balmino et al. (1982)[4-6] truncated to 16 × 16.

4.2 Regolith Composition and Characteristics

4.2.1 Martian Terrain

Martian soil is the upper-most, fine-grained, and porous part of the regolith.[4-7] A thick permafrost (mean annual temperature of less than 273°K) is believed to cover the entire planet and extend to a depth of about one kilometer at the equator and several kilometers at the pole. Within 40 degrees latitude of the Equator, however, the ground is permanently dehydrated to depths of at least one meter. Depending on the permeability of the regolith, there may be water ice below this depth.[4-8] (section 4.2.7)

Extensive dune fields exist over large areas, particularly in a belt around the North Pole and within large craters around the South Pole. The dunes form a pattern suggesting a constant wind direction and strength. Such dunes may fail to provide the load-bearing surface required for landing and pose a potential hazard. Whether the dune-forming processes are active or inactive is unknown.

Information on the Martian surface is largely based on remote sensing observation and image analysis. Observations at the two Viking and one Mars Pathfinder landing sites are not necessarily typical of the Martian surface. Both Viking sites are very rocky compared to averages and the Pathfinder site features an even rockier terrain. Additionally, the Pathfinder site exhibits features consistent with formation involving sand-sized particles (particles 62 to 2000 micrometers in diameter).[4-9]

4.2.2 Crater Density

One of the most ubiquitous features of the Mars surface is the large number of craters of various sizes. Depending on region of the planet, the number density of 1-km diameter craters ranges from less than 160 to about 4800 per million km^2, whereas in some areas there can be as many as 200 or more craters per million km^2 of diameter 15 km or larger (figure 4-4).

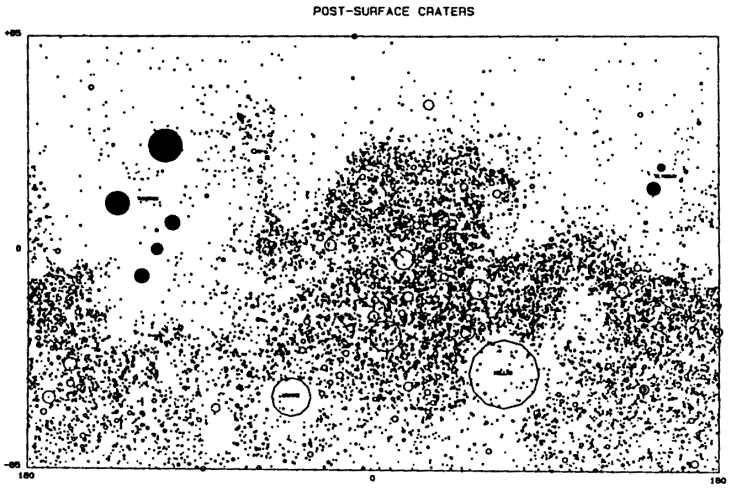

Figure 4-4. Distribution of Martian craters with diameters greater than 15 km. Large volcanoes in the Tharsis and Elysium regions and the Hellas and Argyre impact basins are also included for reference.[4-10]

4.2.3 Soil Properties

To date the Martian regolith at the three landing sites has been characterized as a soil-like material covered with rocks and very fine dust. For reference, rocks covered an area ranging from 8 percent to about 16 percent of the surface at the three sites. Drift material appeared to be very fine grained and porous with low cohesion. The mechanical properties of the soil appeared similar to moderately dense soils on Earth, such as clay-like silt with imbedded sands, granules, and pebbles. However, the deposits were not uniform. A Rover wheel produced reflective ruts indicating a fine-grained porous deposit that is compressible. Table 4-1 summarizes the results of the Rover Sojourner experiment to characterize the martian surface. Table 4-2 summarizes the basic characteristics of the martian surface and Table 4-3 lists the properties of various Martian material analogs that might be used in Earth-based simulations. The surface material properties, such as angle of repose, bearing strength, penetration resistance, and tendency to rut and washboard, can then be estimated from the following:

- Acceleration of gravity at the surface (~3.7 m/s^2)
- Material properties such as cohesion, friction angle, bulk density, compressibility, and pore fluid pressure
- Topographical configuration of the surface
- Properties of the structures placed on and in the surface materials.[4-11]

Table 4-1. Characterization of the Martian Surface Deposits by the Mars Pathfinder Rover, Sojourner. The Sojourner wheels acted as a shear test device utilizing the Mohr-Coulomb failure criteria: $S=c+N[\tan\Phi]$ where S is shear or tractive stress, c is cohesion, and N is normal stress, and $\tan\Phi$ is the coefficient of friction. The apparent friction coefficient, $\tan\alpha$, is given by $S/N=(c/N)+\tan\Phi$.[4-12 4-13]

Exp No[1]	Sol[2]	Wheel[3]	Number Of turns[4]	T (°C)	Depth (cm)	Tan(α)[5]	Θ(deg)	c (kPa) if Φ = Θ	Φ(deg)[6]	c(kPa)[6]	Material type	X(m)[7]	Y(m)[7]
1	3	LF	-0.25		0.4	0.850	38.3	0.21	37.0	set to 0	Cloddy	1.5	-1.5
2	4	RR	+1.0	3.1	1.6	0.804	38.3	0.09	34.4	0.31	Cloddy	2.8	-2.5
		RF	+1.0	1.8	0.2						Cloddy	2.8	-2.5
3	13	RR	+1.0	-2.4	1.3	0.866	38.3	0.34	41.5	-0.04	Cloddy	3.3	-1.3
		RF	+1.0	-2.4	0.2						Cloddy	3.3	-1.3
4	13	RR	+1.0	0.3	3.8	0.753	36.8	0.15	33.3	set to 0	Cloddy	3.3	0.0
5	15	RR	+0.25		0.0			Large		large	Consolidated	3.1	1.2
6	18	LF	-1.0								Cloddy	2.6	-1.2
7	18	LF	-1.0								Cloddy	2.6	0.0
8	21	LR	+1.5	-6.7	6.0	0.820	38.3	0.09	42.4	-0.18	Cloddy	3.4	-0.7
9	23	RF	-1.0	-1.2	0.8	0.495	24.0	0.36	26.4	0.53	Compressible	3.4	1.1
10	27	RR	+1.5	-0.9	3.7	0.806	34.0	0.27	37.1	0.08	Mixed	-2.4	4.4
		RR	+0.48		0±1.2	0.773	34.0	0.30	36.9	0.04	Mixed?		
		RR	+1.02		1.2±3.7	0.821	34.0	0.26	41.2	0.08	Cloddy		
11	27	RR	+1.5	3.1	4.3	0.778	34.0	0.19	36.9	0.06	Mixed	-2.9	4.2
		RR	+0.32		0±1.0	0.655	34.0	0.00	28.2	0.18	Drift		
		RR	+1.19		1.0±4.3	0.814	34.0	0.27	41.0	-0.10	Cloddy		
12	29	LR	+1.5	-35	3.2	0.662	32.4	0.40	34.7	0.23	Mixed	-5.6	2.6
		LR	+0.46		0±1.4	0.709	32.4	0.18	35.1	0.01	"Dune"		
		LR	+1.04		1.4±3.2	0.847	32.4	0.43	40.6	-0.02	Cloddy		
	29	RF	-1.0								Mixed?	-5.6	3.0
	29	LR	+1.5	-35	1.5	0.778	32.4	0.26	38.1	-0.04	Mixed?	-6.2	2.5

[1]Experiment number may include several spins of the same or different wheels in the same material at slightly different locations. [2]A sol is a Pathfinder martian event day; sol 1 is the sol of landing. [3]Wheel: first letter--left (L) or right (R); second letter—front (F) or rear (R). [4]The number of full or partial turns; +=forward direction, -=reverse direction. [5]Average apparent friction coefficient. Φ is the friction angle. Θ is the angle of repose. [6]From least squares fits to concurrent values of shear or tractive stress and normal stress; cohesion set to zero (c=0) in two cases. [7]Experiments can be located on Pathfinder maps with these X and Y coordinates.

Table 4-2. Material Properties of the Martian Surface. Note: cohesion is the sheer strength of rock unrelated to interparticle friction. Adhesion is molecular attraction between contiguous surfaces. The angle of internal friction is the portion of the sheer strength of a rock that depends on the magnitude of the normal stress on a potential sheer fracture [after Mendell et. al., 1999].[4-14] See 1) Moore et al.,[4-15]; 2) Rover Team[4-12]; 3) Moore, et al., [4-13].

Parameter	Units	VL Drift	P Drift	VL – Soil	P -- Soil	Rock
Grain size	μm	0.1-10.0	<40 μm	0.1-10.0		$0.1\text{-}10^4$
Density	kg/m^3	1000 ± 150	1200-1300	1400 ± 200	1520	2600-2800
Cohesion	kPa	1.6 ± 1.2	0.53	1.1 ± 0.8	0.120-0.356	$10^3\text{-}10^4$
Adhesion	Pa	0.9-79		0.9-79		
Angle of internal friction	deg	18.0 ± 2.4	26	34.5 ± 4.7	32-41	40-60
Thermal inertia	$W/(m^2 \cdot s^{1/2})$	40-125		210-460		1650-2100
Specific heat	J/(kg·K)	670-840		670-840		670-840
Thermal conductivity	10^{-5}·J/(s·m·K)	$10^3\text{-}10^2$		0.04-0.23		1.25-2.51
Electrical conductivity	S/m	10^{-14}		10^{-12}		10^{-9}

VL: Viking Lander P: Pathfinder

Table 4-3. Properties of Possible Martian Material Analogs [4-14] [4-15] [4-16]

Material	Grain Size (μm)	Density (kg/m^3)	Cohesion (kPa)	Internal Friction (deg)	Thermal Inertia [$J/(m \cdot s^{1/2} \cdot K)$]	Dielectric Constant
Lunar Nominal	1-330	1350-1800	$10^3\text{-}10^4$	30-40	85-2135	2.5-3.8
Lag gravel	1000-530,000	1400-1700	0	34 ± 5	420	3-4
Dune sand	50-1000	1400-1700	$0\text{-}10^3$	35 ± 5	250	2-4
Loess	1-1000	1000-1600	$0\text{-}10^6$	33 ± 8	210	2.3-4
Rock	N/A	2700-3200	$10^8\text{-}10^9$	45 ± 5	840	8-9

4.2.4 Tribology

The estimates of soil friction angles are considered good because they compare with data on common terrestrial soils and lunar-regolith simulants.[4-11] Moore suggests that the friction angle is a function of void ratio, grain shape, and grain mineralogy. Crude estimates of friction angles for soil-like materials at the Viking landing sites range from 18.0 degrees ± 2.4 degrees for drift material, to 34.5 degrees ± 4.7 degrees for crusty to cloddy material.[4-17] [4-18] [4-19] From soil mechanics experiments performed on the Mars Pathfinder mission, additional estimates of the friction angle, Φ, were obtained. Values of Φ cover the range of 15.1 degrees for drift material, 42.2 degrees for cloddy material, and 45.2 degrees for rock.[4-13]

4.2.5 Chemical Composition

The Viking x-ray fluorescence spectrometer measured fine, loose material found at the site. The Pathfinder rover's alpha proton x-ray spectrometer evaluated rock, soil, and drift material. These lander experiments, however, measured only the elemental composition of the materials; the specific mineral composition can only be inferred. The specific chemical properties measured by the three landers are listed in table 4-4.

Table 4-4. Chemical Properties of Martian Materials [after Mendell et al.[4-14]]

	Mars					Earth
	VL-1 Surface Soil	**VL-2 Surface Soil[1]**	**P Surface Soil[2]**	**P Drift[3]**	**P Rock[4]**	**Oceanic Crust**
SiO_2	43.0	43.0	47.9	50.2	62.0	50.7
FeO			17.3	17.1	12.0	9.9
Fe_2O_3	18.5	17.8				
Al_2O_3	7.3	7.0	8.7	8.4	10.6	15.6
SO_3	6.6	8.1	5.6	5.2	0.0	
MgO	6.0	6.0	7.5	7.3	2.0	7.7
CaO	5.9	5.7		6.0	7.3	11.4
Na_2O			2.8	1.3	2.6	
K_2O	<0.15	<0.15		0.5	0.7	0.17
TiO_2	0.66	0.56	0.9	1.3	0.7	1.5

VL: Viking Lander; P: Pathfinder. [1] Viking data[4-20]; Pathfinder data[4-21] [2] Soil data from A-5 sample. [3] Drift data for drift next to Mermaid rock. [4] Rock data calculated based on removing the dust coating.

The Viking experiments suggest the presence of oxidants and reactive inorganic compounds in the soil and a lack of organic material, e.g., oxygen was released when the soil was exposed to a warm and humid environment. The long operational lifespan of the three landers, however, suggests that chemical corrosion was not a major environmental factor. Should solar arrays be exposed to significant amounts of water vapor, such as might be produced as a waste product from an astronaut life-support system, anti-corrosion measures will need to be considered.

4.2.6 Seismic Activity

Although Mars may be seismically active, the Viking seismometers failed to detect any clear signs of seismic activity. Even so, quake protection may need consideration in the design of equipment and structures. Table 4-5 provides information on predicted quake recurrence intervals.

Table 4-5. Predicted Recurrence Interval for Seismic Events on Mars.[4-22]

Terrestrial Magnitude (Moment Magnitude)	Recurrence Interval
6.7	**35.6 years**
5.8	**4.5 years**
4.9	**6.8 months**
4.0	**0.9 month**
3.1	**3.3 days**
2.2	**9.8 hours**
1.3	**1.2 hours**

4.2.7 Sub-Surface Ice and Water

Ground ice can exist in equilibrium with the Mars atmosphere only at latitudes where crustal temperatures are below the frost point of atmospheric water vapor (about 198 K). Ground ice can exist below the surface down to a depth of the melting isotherm (about 273 K). Figure 4-5 shows a latitude cross section of these relevant isotherms. Mariner remote sensing data and more recent observations by the Russian Phobos 2 spacecraft suggest that water in some form (absorbed in the soil, in hydration, or in the form of ice) is ubiquitous in amounts that range from a few tenths of a percent to a few percent. Better determination of ground water character and abundance is very important to future Mars missions for in situ resource utilization.

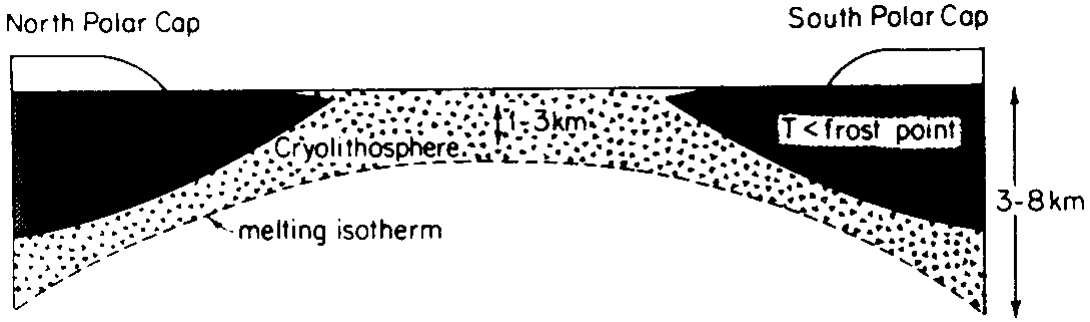

Figure 4-5. Pole-to-pole cross section of the Martian crust showing latitudinal variation in depth of 273 K melting isotherm and 198 K frost point isotherm.

4.3 Surface Physical Characteristics

4.3.1 Rock and Boulder-Size Frequency Distribution

Much of the Martian surface features rocky terrain, including loose rocks and outcrops. Rocks covered 14 percent of the surface at the first Viking landing site, 16 percent at the second Viking site, and about 16 percent at the Pathfinder landing site, neglecting outcrops. Rock sizes ranged from golf ball size to over one meter, with pebbles also found at the Pathfinder site. The Pathfinder rocks appeared to have been transported by massive flooding from Ares Vallis. In fact, the Ares Vallis landing site for Pathfinder was selected primarily for the opportunity to sample a variety of rocks representing ancient crust, ridged plains, and a delta/fan channeled

terrain. For the Pathfinder mission, high rock abundance--with many closely spaced large rocks--was considered desirable for productive science, though unfavorable for operational and safety considerations.

Determining the size-frequency distribution of rocks is critical for determining the potential hazards to a Mars lander. However, it is difficult to predict the size of rocks in the range from 20 centimeters to 1 or 2 meters for different locations on Mars due to the limited data. By fitting remote sensing data to models of rock abundance (tested against Viking lander stereo images), Golombek and Rapp[4-23] determined that most of Mars is rather benign with regard to landing on large rocks. For a total Mars rock coverage of 8 percent, only about 1 percent of the Martian surface is covered by 20 centimeters or higher rocks.[4-23] Figures 4-6 and 4-7 show that the presence of large rocks is proportional to an exponential decrease in their frequency.[4-23]

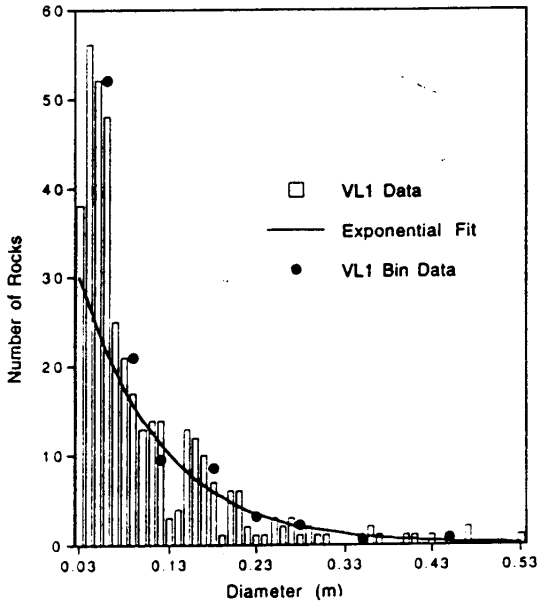

Figure 4-6. Histogram showing number of rocks of each diameter (measured to nearest centimeter) at Viking Lander 1 site.[4-23]

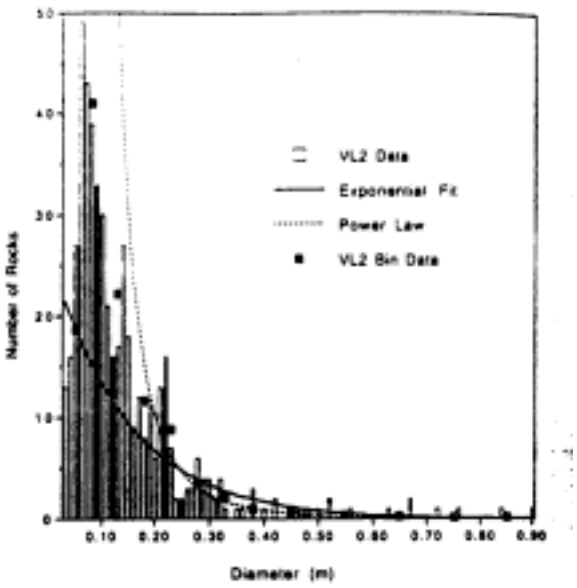

Figure 4-7. Histogram showing number of rocks of each diameter (measured to nearest centimeter) at Viking Lander 2 site.[4-23]

Golombek and Rapp[4-23] concluded that a lander designed to accommodate landing on 0.5-meter high boulders, such as the Mars Pathfinder airbag system, could land on a surface covered by about 20 percent rocks, with approximately 1 percent of the surface covered by rocks 0.5 meters or higher. Based on the rock distribution at the surface, the ability of a lander to successfully cushion the landing impact depends on both the impact velocity vector (speed and direction) and the sizes and shapes of the rocks.[4-23]

Mars Pathfinder provided additional observations for the assessment of landing hazards due to rock size-frequency distributions. Plots of the cumulative fractional area covered by rocks larger than a given diameter or height are depicted in figures 4-8 and 4-9 respectively.[4-24] These plots incorporate data from both Viking sites, the Pathfinder site, and model curves for total rock coverage.

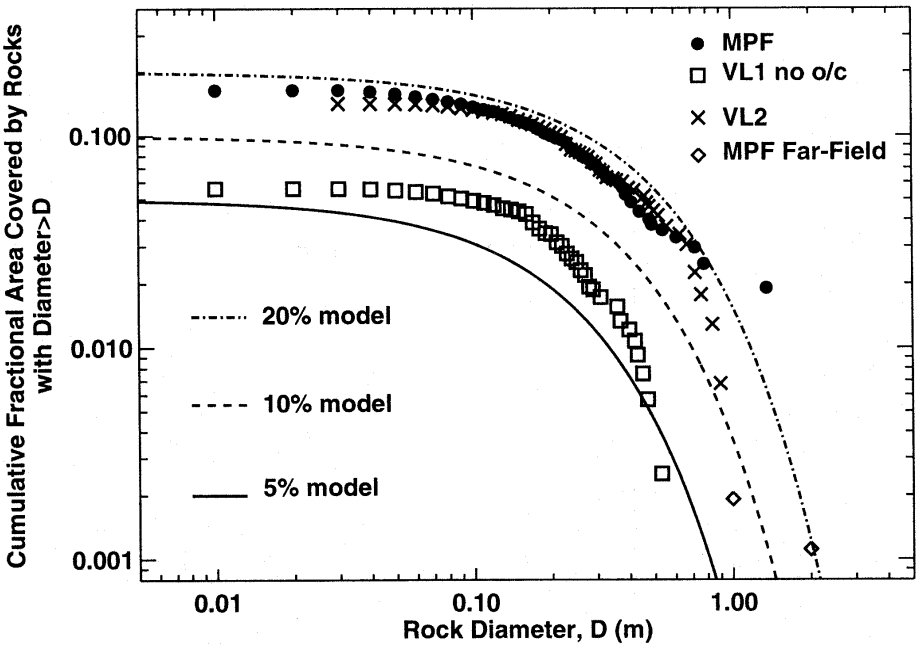

Figure 4-8. Cumulative Fraction of Area Covered by Rocks Versus Rock Diameter at Pathfinder and Viking Landing Sites for Model Predictions. Figure 2 of [Golombek et al.,].[4-24] Data show that the cumulative area covered by rocks greater than 1-m diameter is less than 1% at the Pathfinder landing site, consistent with model predictions.

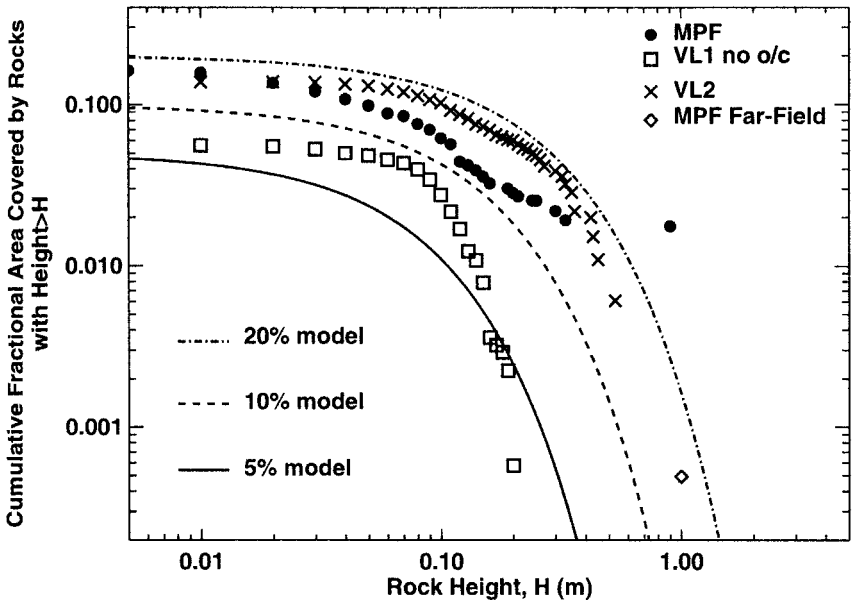

Figure 4-9. Cumulative Fraction of Area Covered by Rocks Versus Rock Height at Pathfinder and Viking Landing Sites for Model Predictions. [Figure 3 in Golombek et al.,].[4-24] Data show that the cumulative area covered by rocks greater than 0.5-m high is less than 1% at the Pathfinder landing site, consistent with model predictions.

4.3.2 Albedo and Thermal Inertia Relation

Albedo is the fraction of radiation received by the surface that is reflected upward. Except for polar ice cap regions, where the albedo can be about 0.6, surface albedo ranges between about 0.1 and 0.4. Albedo, important in determining the solar and infrared radiation balance of the surface, directly affects both soil surface temperature and air temperature immediately above the surface. Surface albedo at ultraviolet wavelengths is not well known. For certain sandy soils on Earth, UV albedo can play an important role in a person's overall exposure to UV radiation.

Thermal inertia (measured in units of 10^{-3} cal cm^{-2} $s^{-1/2}$ K^{-1}; section 4.3.3) also plays an important role in surface energy budget and temperature variations. There are two modal values of thermal inertia at about 2 to 3 units and at about 6 to 7 units. Figure 4-10 shows measured distribution of both albedo and thermal inertia, indicating a significant negative correlation between these two parameters.

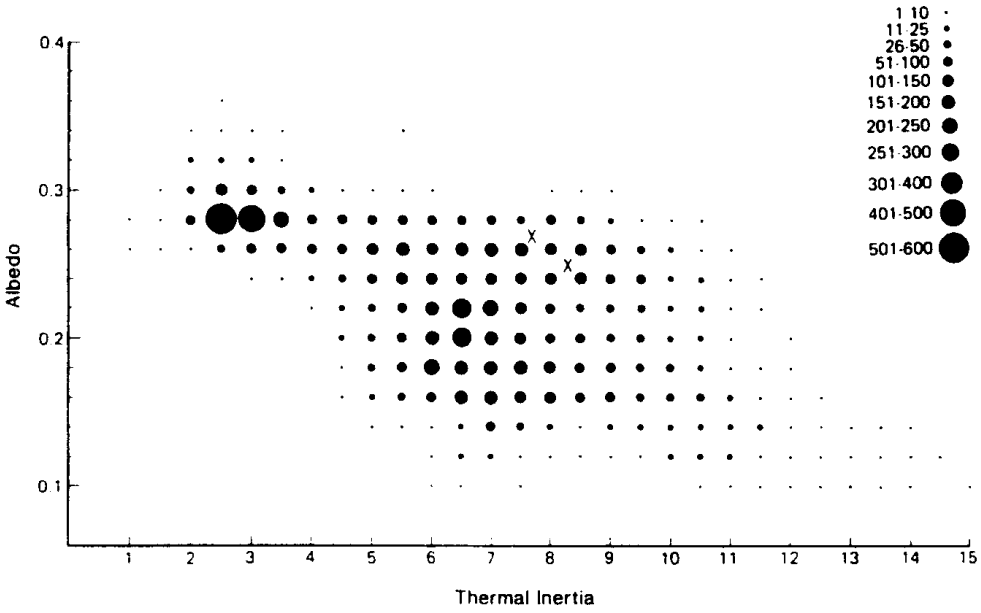

Figure 4-10. Mars surface thermal inertia versus albedo. The size of each dot gives the number of 2° × 2° latitude-longitude bins which have a given combination of albedo and thermal inertia. X's indicate the Viking lander sites.[4-25]

4.3.3 Thermal Inertia

Given the current limitations of remote sensing, the overall rock abundance comes from comparing diurnal behavior of infrared temperatures at several wavelengths and comparing to models. Thermal inertia is the rate at which the surface heats and cools when exposed to the Sun. Loose dust has a very low thermal inertia while large rocks and outcrops have very high thermal inertia.[4-3] Figure 4-11 depicts the relationship of thermal inertia to regolith material; figure 4-12 provides the global distribution.[4-26] [4-27]

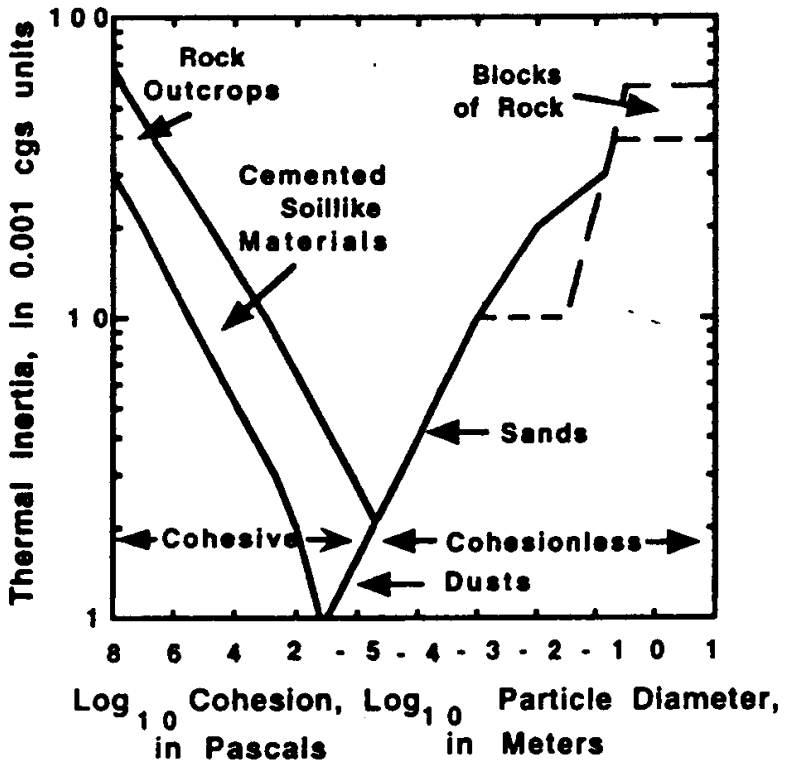

Figure 4-11. Relationship between Thermal Inertia and Size of Cohesionless Particles; Hypothetical Relationship Between Thermal Inertia and Cohesive or Cemented Soil-Like Materials and Rock The scale from 8 to 2 corresponds to the Log_{10}(cohesion) while the –5 to 1 scale corresponds to Log_{10}(particle diameter).[4-3]

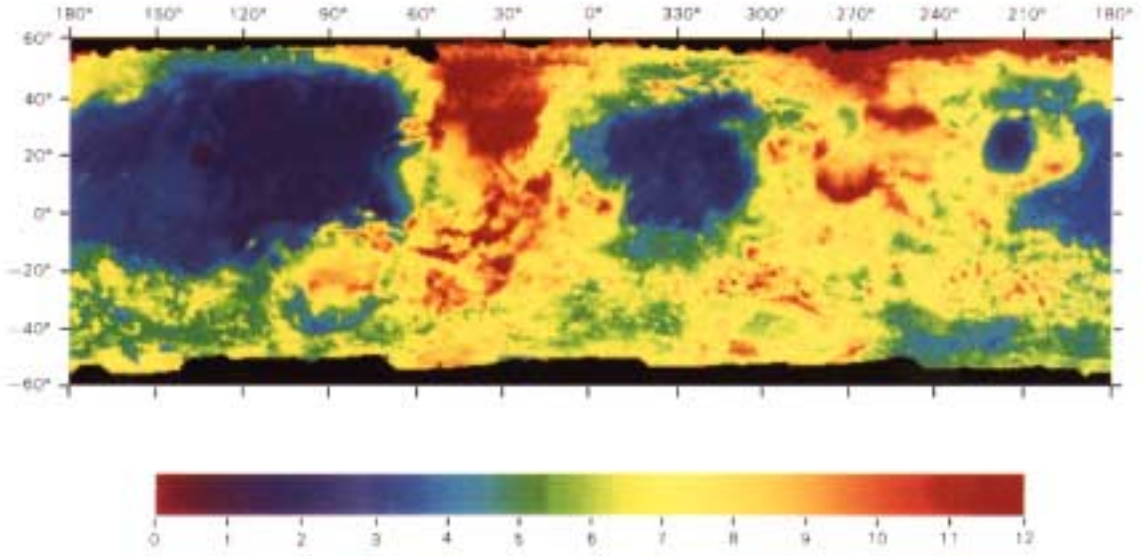

Figure 4-12. Mars Surface Thermal Inertia Map (10^{-3} cal / cm^2 s$^{1/2}$ K). Data were compiled from Viking IRTM sequences.[4-28] For a color version of this figure, contact *jere.justus@msfc.nasa.gov* to get a PDF version of this report.

4.3.4 Albedo

Albedo is a measure of the percentage of incident solar radiation reflected from a given surface. Albedo is inversely correlated with thermal inertia on Mars.[4-25 4-29 4-30] (figure 4-10) Very dark areas are indicative of rock outcroppings or substantial blocks of rock without heavy dust coating. Bright regions tend to have low bulk thermal inertias which may indicate a dusty environment. Hence, areas having high albedos are not attractive as landing sites due to the potential of dust which can coat solar arrays and hinder rover mobility.[4-3]

4.4 Radar Observations

4.4.1 Normal Reflectivity

Landing site evaluations include normal reflectivity because the surface must be sufficiently reflective for detection by a radar altimeter during descent.[4-3] Furthermore, the reflectivity is related to the bulk density of surface materials[4-31 4-32] as indicated by figure 4-13. Low reflectivity coupled with a low thermal inertia may be associated with the presence of loose dust which could coat solar cell arrays and interfere with rover operations. The uppermost few centimeters of surfaces can be assessed by their IR - measured thermal inertia, by Viking IRTM[4-33] and MGS TES. Low thermal inertias imply finer material. Deeper layers can be probed by Earth-based[4-34] and preferably orbital radar. A low albedo is one straightforward clue to the absence of deep dust layers since even a thin layer of dust is light in color. Sites with a moderate reflectivity are considered more suitable than those with low reflectivity because they imply the presence of dense, trafficable material with little loose dust.[4-3]

Landing in conditions of high near-surface saltation (sand motion) may also be problematic to a lander physically, but such windborne millimeter-sized debris is not likely to cause problems for landers using centimeter-wavelength radar altimeters to determine closing velocity and altitude. The saltation zone is unlikely to be deep and the particles are too small to affect the radar return.

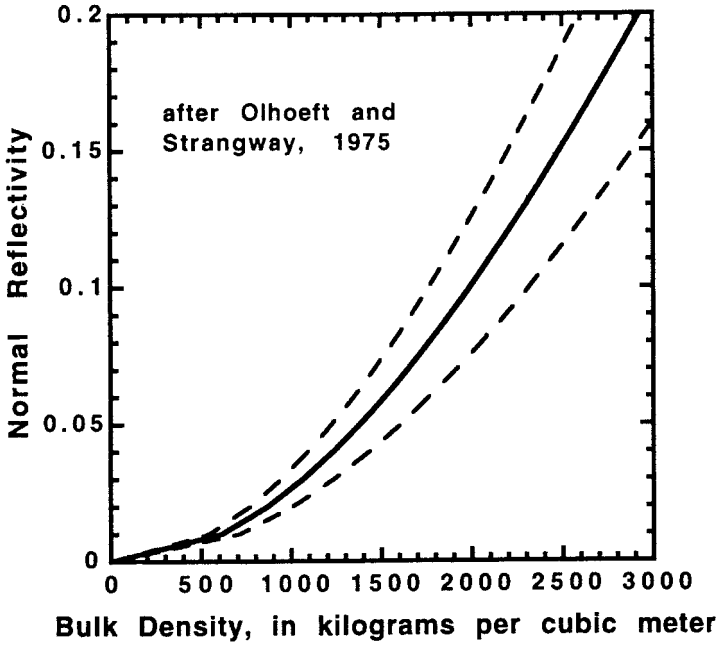

Figure 4-13. Relationship between Normal Reflectivity and Bulk Density of Dry Soillike Materials and Rock Based on Results for Lunar Rocks and Soil. Original data and equation relate dielectric constant with density,[4-32] reflectivity has been calculated using dielectric constant and the Fresnel reflection coefficient.[4-35] Solid line corresponds to fit to data and dashed lines to one standard deviation.[4-3]

4.4.2 Root-Mean-Square Slope

The slope or surface tilt of a potential landing site is greatly important in site evaluation. The slope of the site must be able to accommodate the horizontal velocity of the lander at touch down without tipping the lander. The slope must not be so great that the center-of-mass of the lander extends beyond its base and causes the lander to topple. Finally, the slope must be small enough that the solar panels and instrumentation of the lander are not hindered or compromised. For example, the environmental requirements document for the Mars Surveyor program specified the permissible landing site tilt angle requirement as no more than 10 degrees.

Estimates of surface slopes are obtained from measurements of the dispersion of radar returns in both time and frequency. The root-mean-square (rms) slope is a statistical measure of the probability distribution of surface slopes determined from the quasi-specular component of the radar return.[4-27] Quasi-specular returns arise from surfaces on the scale of radar wavelengths and larger which are oriented for mirror-like reflection. Typical values of rms slopes for Mars are from 2 to 4 degrees which is smoother than the Moon.[4-27] However, in cratered regions (volcanic or impact) the rms slope has been observed from 5 to 10 degrees.

4.5 Mars Surface Ionizing Radiation Environment Definition

Mars transportation vehicles may be required to reside on the Martian surface for long periods of time (up to 2 years) prior to crew arrival. Because crew stays and surface operations can be for several months as well, vehicles must be designed to meet their performance requirements during and after prolonged exposure to the surface ionizing radiation environment. Since no measurements of this environment have been made, modeling is the only way to estimate it. Our knowledge of the surface environment is, thus, theoretically based and suffers from an incomplete understanding of the physical interactions of galactic cosmic rays (GCR) and Solar Particle Events (SPE) with the Martian atmosphere, Martian surface, and intervening shield materials. In these interactions, multiple charged ions are reduced in size and secondary particles are generated, including neutrons. Upon impact with the Martian surface, the character of the interactions changes as a result of the differing nuclear constituents of the surface materials. Among the surface environment are many neutrons diffusing from the Martian surface and especially prominent are energetic neutrons with energies up to a few hundred MeV.

An important component of Mars surface robotic exploration is the opportunity to test our understanding of the Mars surface environment. The Mars 2001 orbiter mission will have the first radiation detectors operating from Martian orbit and will provide a unique opportunity to measure the Mars ionizing radiation environment.

4.5.1 Particle Fluence Spectra

Transportation vehicle designers must know the total integrated dose and linear energy transfer (LET) environments to design robust hardware. To calculate these environments on the surface of Mars the particle energy distributions at the top of the Martian atmosphere must be estimated. This section describes the estimates and transport calculations; the following two sections describe the total dose and LET anticipated on the surface.

The annual fluence spectra at Mars were evaluated assuming a $\sqrt{r}$ radial dependence with distance from the Sun of the diffusion coefficient.[4-36] The functional form of this dependence is not widely agreed upon but some assumption is necessary. The projected Badhwar-O'Neill model[4-37 4-38] for GCR in 1977 (solar minimum, figure 4-14) and 1980 (solar maximum, figure 4-15) and the estimated September 29, 1989 SPE model[4-39] shown in figure 4-16 are used as boundary conditions at the top of the Martian atmosphere. We assume the Martian atmosphere to be CO_2 and distributed according to the COSPAR low-density model.[4-40] The Martian surface is taken as regolith (58.2% SiO2, 23.7% Fe2O3, 10.8% MgO, 7.3% CaO) with minimal differences in transport properties from Martian bedrock.[4-41] The transport code used to describe the interaction of the space environment with the Martian atmosphere and surface is the HZETRN code,[4-42] which has been recently improved in the description of angular dependent neutron transport and corresponding boundary conditions.[4-43]

The HZETRN model solves the Boltzmann transport equations at the interface of the atmosphere and surface. The calculations treat the interaction of all nucleonic and nuclear particles including neutrons. Many new isotopes are produced in the interactions. The calculations presently ignore the pion components, related muons, and electromagnetic cascades. Accuracy of the calculations can be judged by comparisons with shuttle measurements using a tissue equivalent proportional counter (TEPC) shown separately in figure 4-17 for the resolved GCR component and trapped proton component. The fact that the trapped radiations show

greater agreement is in part due to the neglected mesons which are of little importance in the trapped radiation interactions. Added to the surface particle fields are the neutrons which are produced in penetrating the atmosphere and appear as an albedo component produced by interactions in the Martian surface materials. The albedo neutrons from the surface tend to dominate the neutron fields for energies less than 100 to 200 MeV.

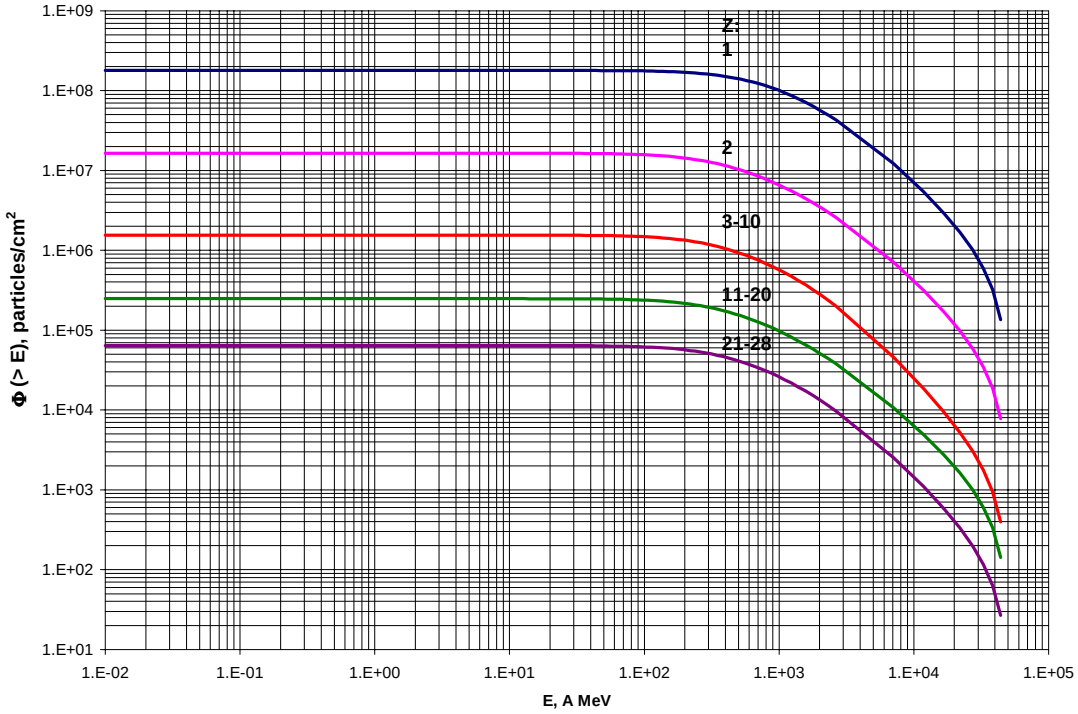

Figure 4-14. The 1977 solar minimum galactic cosmic annual integral fluence spectra for various charge groups.

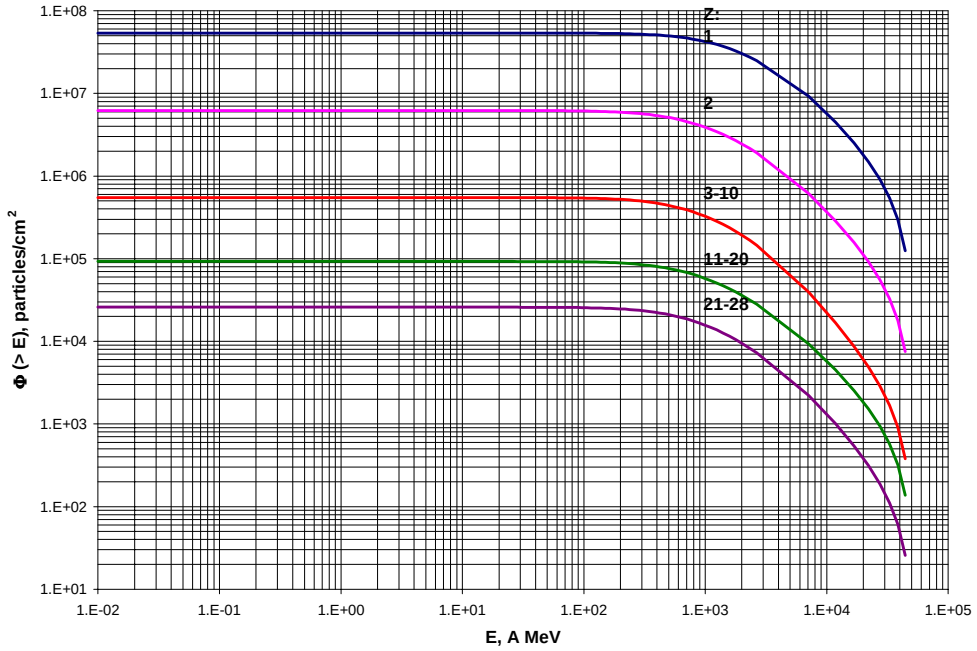

Figure 4-15. The 1980 solar maximum galactic cosmic annual integral fluence spectra for various charge groups.

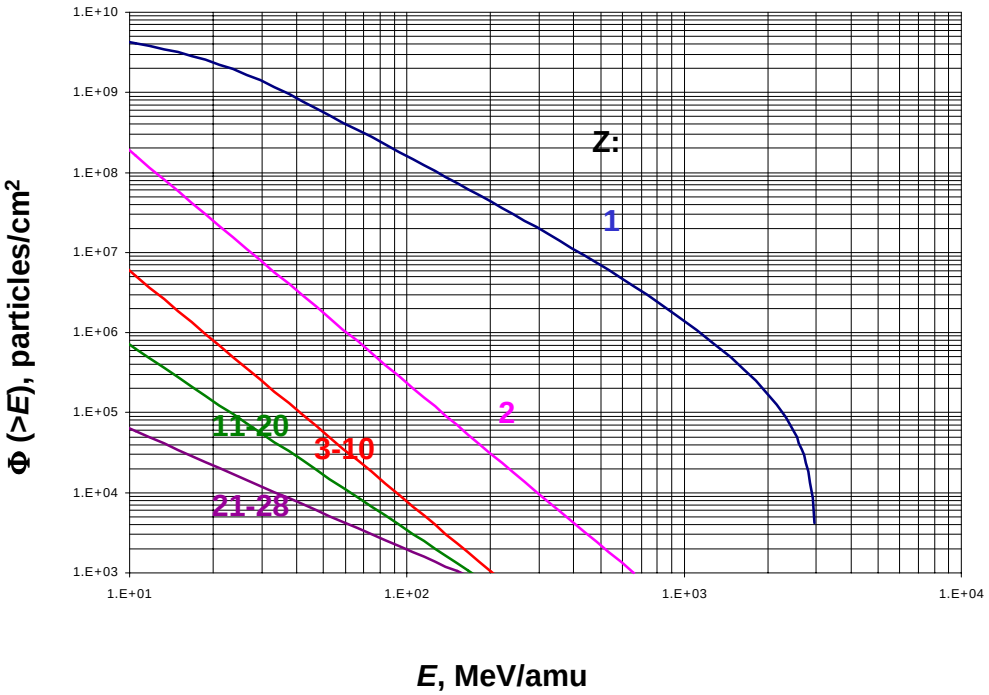

Figure 4-16. The September 29, 1989 solar particle event integral fluence spectra for various charge groups.

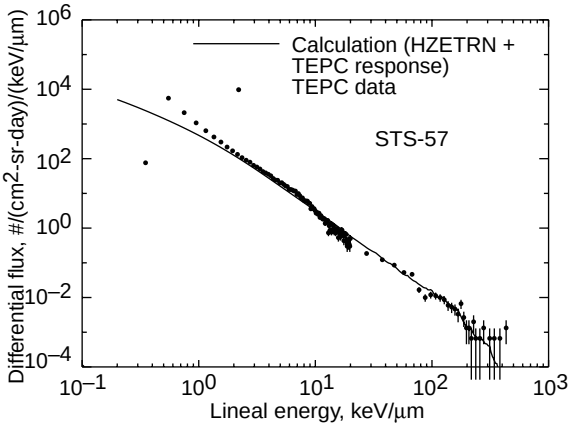

(a) GCR ions

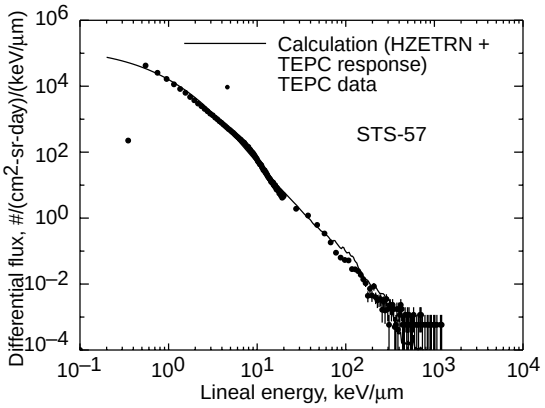

(b) Trapped protons

Figure 4-17. Comparison of HZETRN with measurements with a tissue equivalent proportional counter on STS-57.

The surface environment generated by the GCR for solar minimum and solar maximum is shown, respectively, in figures 4-18 and 4-19, respectively. The highly charged ions are attenuated by the interaction with the Martian atmosphere contributing to the lighter ion fields and neutrons. Impact with the Martian surface generates a backward flux of neutrons extending to a few hundred MeV as seen in the figures. Due to the higher atomic weight elements of the regolith (and bedrock), the backward neutron flux is appreciable compared to the forward propagating component produced in collision with atmospheric components. This effect is also seen in the surface environment generated by a high energy SPE which occurred on September 29, 1989 (figure 4-20).

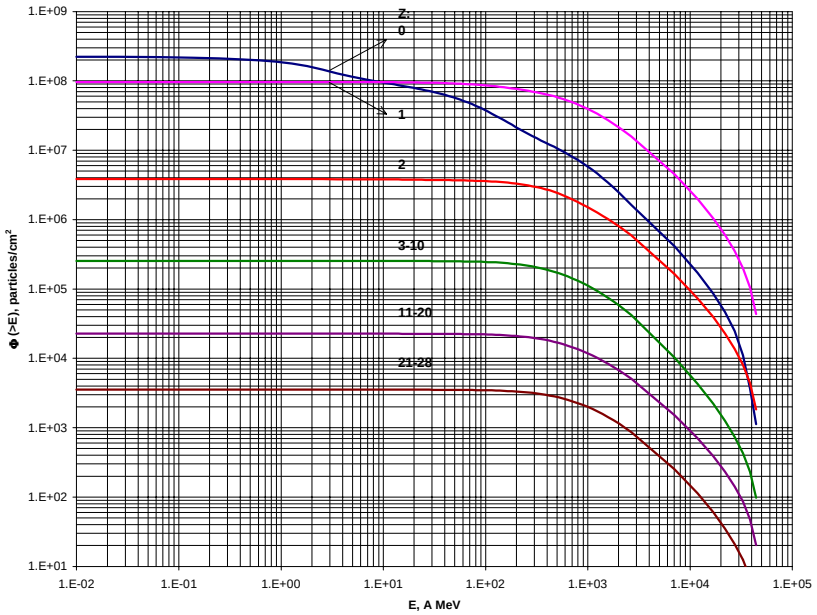

Figure 4-18. Integral spectra of particles on the Martian surface produced by the 1977 solar minimum galactic cosmic rays.

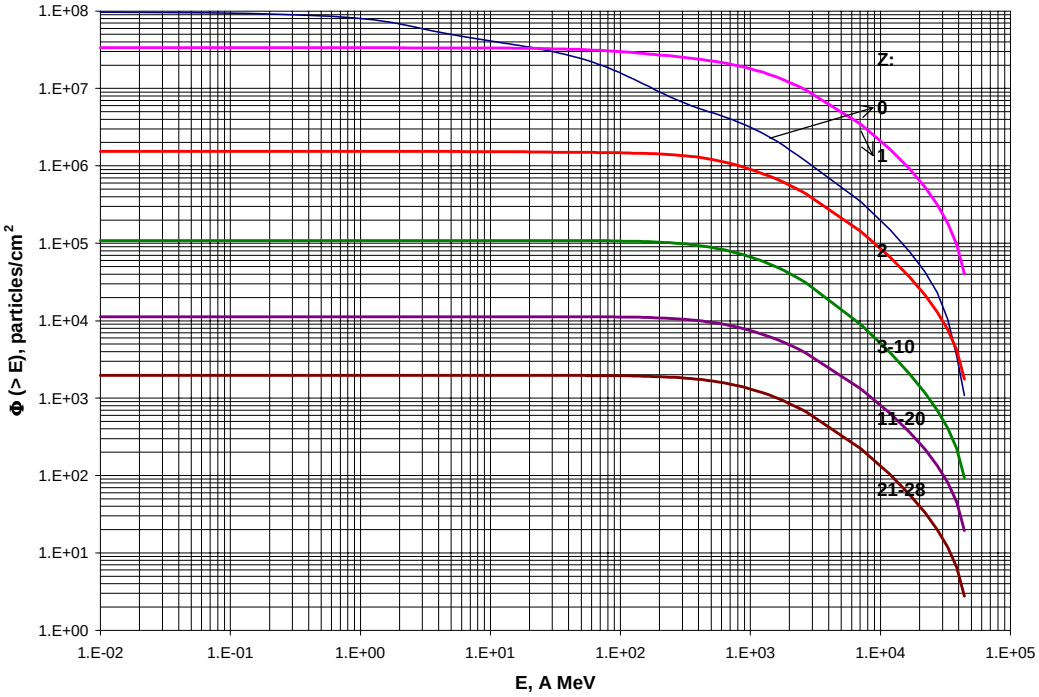

Figure 4-19. Integral spectra of particles on the Martian surface produced by the 1980 solar maximum galactic cosmic rays.

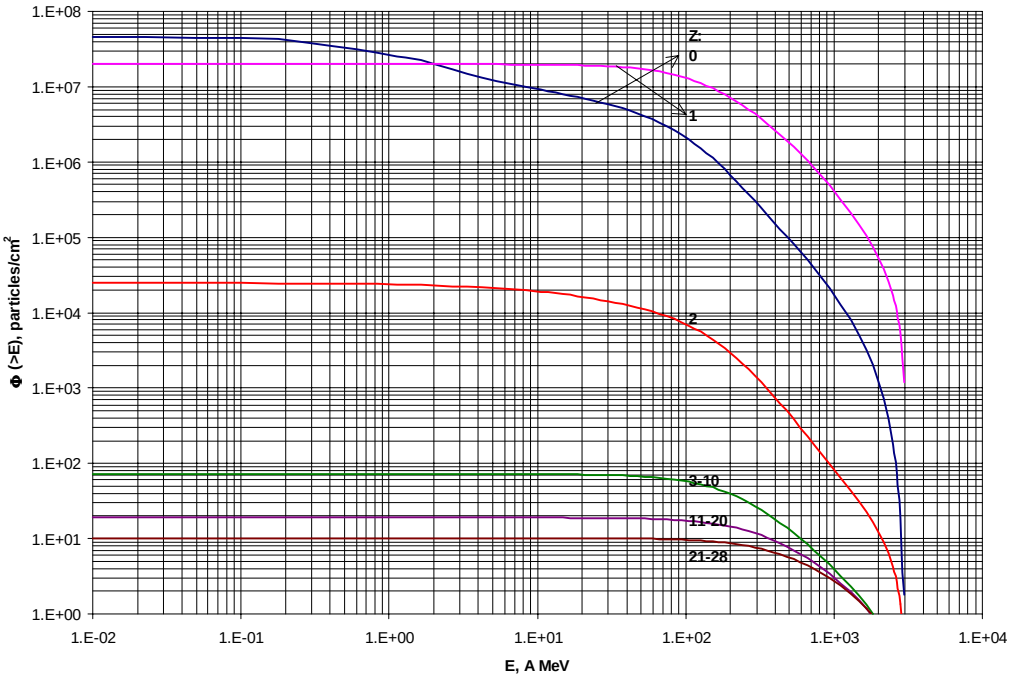

Figure 4-20. Integral spectra of particles on the Martian surface produced by the September 29, 1989 solar particle event.

4.5.2 Dose to Electronic Devices and Surface Coatings

Devices and polymeric materials are sensitive to accumulative charge generated in the device or the total number of chemically active free radicals produced. Both quantities (total charge or total free radicals) are determined by the energy absorbed per unit mass (i.e., dose) by the device or material from the radiation field. Shielding is often used to reduce the dose but its effectiveness depends on the characteristics of the incident radiation and its interaction with the shield material. The absorbed dose depends on the composition of the device or material. Experimental degradation data is usually expressed in terms of the monitored exposure database normally expressed in units of the device to monitor the test, namely a silicon detector. There absorbed dose in silicon is the normal unit of exposure and is traditionally expressed in units of rad-Si equal to 100 ergs per gram or in modern SI units of Gray-Si equal to one joule per kilogram (note 1 rad is equal to 10 mGy or 1 cGy). The shield considered in the present calculation is a spherical shield of equivalent aluminum enclosing the device or material. The annual dose delivered to a device or material protected by a spherical aluminum shield from the surface radiation during the 1977 solar minimum is given in table 4-6. Similar results during the 1980 solar maximum are shown in table 4-7 and for the September 29, 1989 solar particle event in table 4-8.

4.5.3 Single Event Effects Environment

The passage of an energetic charged ion through an element of an electronic device releases electrons from atomic orbitals of the device materials. The number of electrons released is proportional to the ion charge squared and can be very large for multiple charged ions. The resulting electron-hole pairs result in transient currents and other damage mechanisms resulting in possible single event upsets (SEE), latchup, burnout. The distinguishing characteristic of the ion

Table 4-6. Annual dose in silicon inside a spherical shell shield of equivalent aluminum on the Martian surface during the 1977 solar minimum.

Equivalent aluminum thickness, mil	Dose in a spherical shell shield, rads-Si
0	7.46
50 (1.27 mm)	7.55
500 (12.7 mm)	7.51
1000 (25.4 mm)	7.45
2000 (50.8 mm)	7.33
4000 (101.6 mm)	7.06
7000 (177.8 mm)	6.63

Table 4-7. Annual dose in silicon inside a spherical shell shield of equivalent aluminum on the Martian surface during the 1980 solar maximum.

Equivalent aluminum thickness, mil	Dose in a spherical shell shield, rads-Si
0	2.64
50 (1.27 mm)	2.68
500 (12.7 mm)	2.71
1000 (25.4 mm)	2.72
2000 (50.8 mm)	2.73
4000 (101.6 mm)	2.72
7000 (177.8 mm)	2.65

Table 4-8. Dose in silicon inside a spherical shell shield of equivalent aluminum on the Martian surface during the September 29, 1989 solar particle event.

Equivalent aluminum thickness, mil	Dose in a spherical shell shield, rads-Si
0	2.18
50 (1.27 mm)	2.14
500 (12.7 mm)	1.76
1000 (25.4 mm)	1.46
2000 (50.8 mm)	1.08
4000 (101.6 mm)	0.68
7000 (177.8 mm)	0.41

is its rate of linear energy transfer (LET) to the medium characterized by the energy lost by the ion per unit pathlength. The number of such SEE occurrences is related to the number of particles whose LET is above some threshold value for the effect to occur. The integral LET spectra are evaluated herein for silicon devices and, therefore, expressed as LET in Si. The integral LET spectrum within various aluminum spherical shell shields of given thickness is given for the 1977 solar minimum in table 4-9 and shown in figure 4-21. The corresponding values for the 1980 solar maximum and the September 29, 1989 solar particle event are given in tables 4-10 and 4-11. A graphical presentation is shown in figures 4-22 and 4-23.

Table 4-9. Annual fluence spectra of LET in silicon within spherical shells of equivalent aluminum shielding on the Martian surface during 1977 solar minimum.

LET, MeV-cm^2/mg	Annual fluence (particles/cm^2) with > LET within equivalent aluminum shield of-						
	0	50 mil (1.27 mm)	500 mil (12.7 mm)	1000 mil (25.4 mm)	2000 mil (50.8 mm)	4000 mil (101.6 mm)	7000 mil (177.8 mm)
1.235E-03	1.006E+08	1.007E+08	1.003E+08	9.958E+07	9.783E+07	9.345E+07	8.590E+07
1.525E-03	1.006E+08	1.007E+08	1.003E+08	9.958E+07	9.783E+07	9.345E+07	8.590E+07
1.884E-03	6.147E+07	6.161E+07	6.189E+07	6.196E+07	6.170E+07	6.021E+07	5.671E+07
2.326E-03	4.069E+07	4.086E+07	4.137E+07	4.170E+07	4.198E+07	4.161E+07	3.984E+07
2.873E-03	3.132E+07	3.149E+07	3.199E+07	3.232E+07	3.265E+07	3.249E+07	3.122E+07
3.548E-03	2.478E+07	2.494E+07	2.535E+07	2.561E+07	2.585E+07	2.569E+07	2.466E+07
4.382E-03	1.979E+07	1.993E+07	2.023E+07	2.038E+07	2.049E+07	2.023E+07	1.932E+07
5.412E-03	1.587E+07	1.600E+07	1.618E+07	1.623E+07	1.620E+07	1.583E+07	1.499E+07
6.683E-03	1.284E+07	1.296E+07	1.303E+07	1.299E+07	1.284E+07	1.238E+07	1.157E+07
8.254E-03	8.445E+06	8.561E+06	8.650E+06	8.658E+06	8.626E+06	8.442E+06	8.046E+06
1.019E-02	6.033E+06	6.144E+06	6.203E+06	6.197E+06	6.166E+06	6.040E+06	5.776E+06
1.259E-02	4.368E+06	4.471E+06	4.507E+06	4.491E+06	4.459E+06	4.363E+06	4.174E+06
1.555E-02	3.185E+06	3.280E+06	3.298E+06	3.277E+06	3.245E+06	3.166E+06	3.026E+06
1.920E-02	2.321E+06	2.407E+06	2.413E+06	2.391E+06	2.359E+06	2.294E+06	2.189E+06
2.371E-02	1.721E+06	1.797E+06	1.791E+06	1.769E+06	1.738E+06	1.677E+06	1.593E+06
2.929E-02	1.288E+06	1.352E+06	1.341E+06	1.319E+06	1.287E+06	1.232E+06	1.163E+06
3.617E-02	9.812E+05	1.032E+06	1.017E+06	9.950E+05	9.630E+05	9.124E+05	8.535E+05
4.467E-02	7.509E+05	7.894E+05	7.719E+05	7.511E+05	7.205E+05	6.745E+05	6.253E+05
5.517E-02	5.834E+05	6.118E+05	5.927E+05	5.732E+05	5.437E+05	5.011E+05	4.589E+05
6.813E-02	4.363E+05	4.565E+05	4.393E+05	4.229E+05	3.988E+05	3.645E+05	3.324E+05
8.414E-02	3.376E+05	3.520E+05	3.357E+05	3.213E+05	3.001E+05	2.708E+05	2.442E+05
1.039E-01	2.564E+05	2.664E+05	2.525E+05	2.406E+05	2.227E+05	1.988E+05	1.787E+05
1.283E-01	1.809E+05	1.880E+05	1.784E+05	1.700E+05	1.580E+05	1.431E+05	1.301E+05
1.585E-01	1.365E+05	1.415E+05	1.336E+05	1.272E+05	1.181E+05	1.064E+05	9.705E+04
1.957E-01	1.019E+05	1.053E+05	9.922E+04	9.413E+04	8.738E+04	7.869E+04	7.210E+04
2.417E-01	7.768E+04	7.970E+04	7.490E+04	7.104E+04	6.552E+04	5.882E+04	5.414E+04
2.985E-01	5.480E+04	5.591E+04	5.265E+04	5.005E+04	4.619E+04	4.182E+04	3.907E+04
3.687E-01	3.850E+04	3.918E+04	3.679E+04	3.486E+04	3.205E+04	2.958E+04	2.774E+04
4.553E-01	2.692E+04	2.723E+04	2.555E+04	2.398E+04	2.228E+04	2.035E+04	1.916E+04
5.624E-01	1.803E+04	1.799E+04	1.660E+04	1.554E+04	1.411E+04	1.269E+04	1.189E+04
6.945E-01	1.248E+04	1.244E+04	1.138E+04	1.054E+04	9.427E+03	8.315E+03	7.706E+03
8.577E-01	8.340E+03	8.307E+03	7.508E+03	6.851E+03	5.983E+03	5.129E+03	4.674E+03
1.059E+00	5.345E+03	5.326E+03	4.714E+03	4.219E+03	3.555E+03	2.905E+03	2.584E+03
1.308E+00	2.430E+03	2.429E+03	2.135E+03	1.895E+03	1.592E+03	1.305E+03	1.176E+03
1.616E+00	8.193E+02	8.011E+02	6.478E+02	5.136E+02	3.307E+02	1.478E+02	4.994E+01
1.995E+00	4.746E+02	4.652E+02	3.761E+02	2.979E+02	1.916E+02	8.578E+01	2.913E+01
2.464E+00	2.794E+02	2.746E+02	2.220E+02	1.757E+02	1.130E+02	5.057E+01	1.725E+01
3.043E+00	1.653E+02	1.630E+02	1.317E+02	1.043E+02	6.688E+01	2.988E+01	1.012E+01
3.758E+00	9.753E+01	9.655E+01	7.791E+01	6.153E+01	3.948E+01	1.753E+01	5.901E+00
4.642E+00	5.684E+01	5.641E+01	4.552E+01	3.587E+01	2.279E+01	1.006E+01	3.329E+00
5.733E+00	3.259E+01	3.253E+01	2.614E+01	2.056E+01	1.299E+01	5.652E+00	1.821E+00
7.080E+00	1.819E+01	1.816E+01	1.464E+01	1.141E+01	7.175E+00	3.046E+00	9.742E-01
8.743E+00	9.921E+00	9.911E+00	7.908E+00	6.143E+00	3.830E+00	1.604E+00	4.911E-01
1.080E+01	5.217E+00	5.236E+00	4.149E+00	3.211E+00	1.983E+00	8.169E-01	2.424E-01
1.334E+01	2.568E+00	2.588E+00	2.036E+00	1.561E+00	9.554E-01	3.832E-01	1.106E-01
1.647E+01	1.158E+00	1.172E+00	9.198E-01	7.029E-01	4.235E-01	1.666E-01	4.620E-02
2.034E+01	4.587E-01	4.672E-01	3.636E-01	2.758E-01	1.638E-01	6.223E-02	1.650E-02
2.512E+01	1.188E-01	1.229E-01	9.567E-02	7.087E-02	4.071E-02	1.451E-02	3.582E-03
3.102E+01	1.038E-03	1.038E-03	7.744E-04	5.569E-04	3.052E-04	1.001E-04	2.074E-05

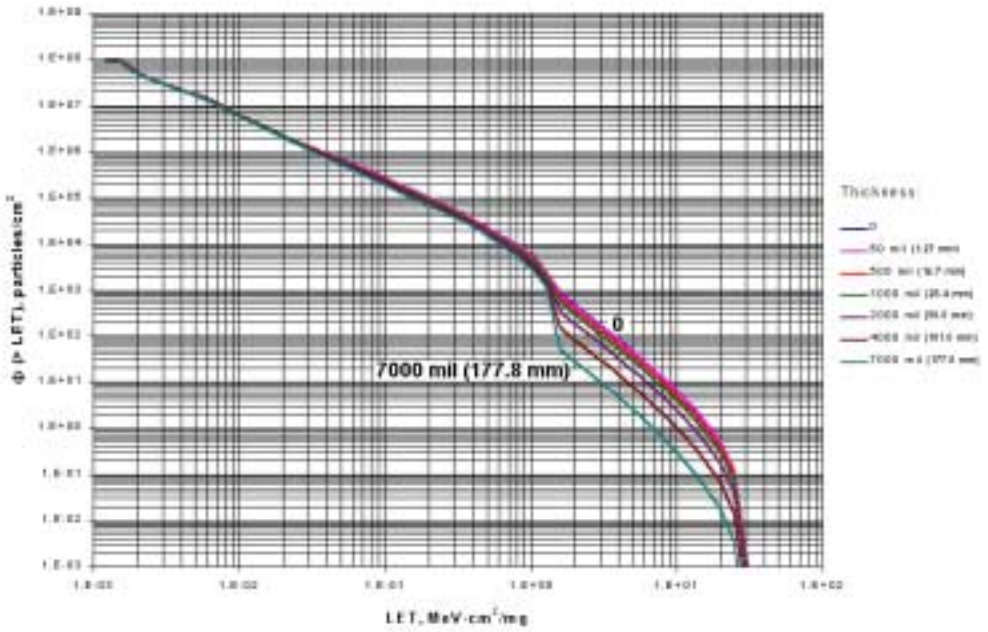

Figure 4-21. Integral LET spectra of particles on the Martian surface produced by the 1977 solar minimum galactic cosmic rays.

Table 4-10. Annual fluence spectra of LET in silicon within spherical shells of equivalent aluminum shielding on the Martian surface during 1980 solar maximum.

LET, MeV-cm^2/mg	Annual fluence (particles/cm^2) with > LET within equivalent aluminum shield of-						
	0	50 mil (1.27 mm)	500 mil (12.7 mm)	1000 mil (25.4 mm)	2000 mil (50.8 mm)	4000 mil (101.6 mm)	7000 mil (177.8 mm)
1.235E-03	3.526E+07	3.533E+07	3.556E+07	3.566E+07	3.567E+07	3.516E+07	3.366E+07
1.525E-03	3.526E+07	3.533E+07	3.556E+07	3.566E+07	3.567E+07	3.516E+07	3.366E+07
1.884E-03	1.928E+07	1.938E+07	1.978E+07	2.009E+07	2.052E+07	2.087E+07	2.069E+07
2.326E-03	1.216E+07	1.226E+07	1.270E+07	1.304E+07	1.355E+07	1.410E+07	1.429E+07
2.873E-03	1.002E+07	1.011E+07	1.049E+07	1.078E+07	1.119E+07	1.162E+07	1.173E+07
3.548E-03	8.363E+06	8.451E+06	8.757E+06	8.979E+06	9.282E+06	9.571E+06	9.598E+06
4.382E-03	6.947E+06	7.026E+06	7.259E+06	7.413E+06	7.608E+06	7.764E+06	7.713E+06
5.412E-03	5.740E+06	5.811E+06	5.977E+06	6.068E+06	6.169E+06	6.211E+06	6.095E+06
6.683E-03	4.752E+06	4.815E+06	4.922E+06	4.962E+06	4.987E+06	4.940E+06	4.774E+06
8.254E-03	2.863E+06	2.927E+06	3.041E+06	3.099E+06	3.175E+06	3.244E+06	3.246E+06
1.019E-02	2.061E+06	2.120E+06	2.205E+06	2.243E+06	2.295E+06	2.347E+06	2.354E+06
1.259E-02	1.519E+06	1.572E+06	1.633E+06	1.655E+06	1.687E+06	1.719E+06	1.721E+06
1.555E-02	1.131E+06	1.179E+06	1.220E+06	1.231E+06	1.249E+06	1.265E+06	1.261E+06
1.920E-02	8.381E+05	8.804E+05	9.073E+05	9.121E+05	9.205E+05	9.266E+05	9.203E+05
2.371E-02	6.341E+05	6.705E+05	6.859E+05	6.866E+05	6.881E+05	6.858E+05	6.755E+05
2.929E-02	4.829E+05	5.130E+05	5.207E+05	5.185E+05	5.157E+05	5.086E+05	4.965E+05
3.617E-02	3.745E+05	3.982E+05	4.006E+05	3.965E+05	3.905E+05	3.803E+05	3.668E+05
4.467E-02	2.897E+05	3.078E+05	3.067E+05	3.016E+05	2.943E+05	2.828E+05	2.698E+05
5.517E-02	2.280E+05	2.412E+05	2.378E+05	2.324E+05	2.241E+05	2.117E+05	1.991E+05
6.813E-02	1.691E+05	1.786E+05	1.749E+05	1.705E+05	1.637E+05	1.536E+05	1.443E+05
8.414E-02	1.328E+05	1.394E+05	1.354E+05	1.311E+05	1.246E+05	1.152E+05	1.067E+05
1.039E-01	1.014E+05	1.061E+05	1.022E+05	9.853E+04	9.289E+04	8.500E+04	7.815E+04
1.283E-01	6.970E+04	7.306E+04	7.065E+04	6.835E+04	6.517E+04	6.066E+04	5.679E+04
1.585E-01	5.364E+04	5.595E+04	5.385E+04	5.197E+04	4.916E+04	4.555E+04	4.253E+04
1.957E-01	4.043E+04	4.202E+04	4.026E+04	3.877E+04	3.659E+04	3.389E+04	3.163E+04
2.417E-01	3.154E+04	3.247E+04	3.093E+04	2.967E+04	2.779E+04	2.551E+04	2.377E+04
2.985E-01	2.192E+04	2.242E+04	2.141E+04	2.054E+04	1.936E+04	1.804E+04	1.712E+04
3.687E-01	1.546E+04	1.576E+04	1.497E+04	1.431E+04	1.341E+04	1.262E+04	1.212E+04
4.553E-01	1.084E+04	1.098E+04	1.045E+04	9.991E+03	9.497E+03	8.767E+03	8.330E+03
5.624E-01	7.417E+03	7.405E+03	6.926E+03	6.549E+03	6.029E+03	5.481E+03	5.184E+03
6.945E-01	5.242E+03	5.230E+03	4.840E+03	4.522E+03	4.082E+03	3.615E+03	3.365E+03
8.577E-01	3.568E+03	3.555E+03	3.249E+03	2.991E+03	2.626E+03	2.246E+03	2.043E+03
1.059E+00	2.322E+03	2.312E+03	2.071E+03	1.865E+03	1.577E+03	1.281E+03	1.130E+03
1.308E+00	9.207E+02	9.230E+02	8.302E+02	7.545E+02	6.515E+02	5.526E+02	5.071E+02
1.616E+00	2.709E+02	2.660E+02	2.239E+02	1.847E+02	1.269E+02	6.214E+01	2.283E+01
1.995E+00	1.528E+02	1.503E+02	1.268E+02	1.048E+02	7.223E+01	3.562E+01	1.319E+01
2.464E+00	8.878E+01	8.765E+01	7.413E+01	6.122E+01	4.228E+01	2.092E+01	7.771E+00
3.043E+00	5.221E+01	5.172E+01	4.382E+01	3.617E+01	2.500E+01	1.236E+01	4.598E+00
3.758E+00	3.089E+01	3.069E+01	2.601E+01	2.147E+01	1.480E+01	7.281E+00	2.702E+00
4.642E+00	1.809E+01	1.808E+01	1.529E+01	1.261E+01	8.629E+00	4.247E+00	1.555E+00
5.733E+00	1.050E+01	1.055E+01	8.914E+00	7.303E+00	5.043E+00	2.442E+00	8.843E-01
7.080E+00	5.957E+00	5.973E+00	5.029E+00	4.131E+00	2.801E+00	1.325E+00	4.713E-01
8.743E+00	3.305E+00	3.329E+00	2.785E+00	2.278E+00	1.530E+00	7.206E-01	2.481E-01
1.080E+01	1.762E+00	1.778E+00	1.490E+00	1.208E+00	8.074E-01	3.744E-01	1.245E-01
1.334E+01	8.797E-01	8.941E-01	7.433E-01	5.998E-01	3.983E-01	1.803E-01	5.808E-02
1.647E+01	4.050E-01	4.116E-01	3.406E-01	2.744E-01	1.797E-01	7.939E-02	2.483E-02
2.034E+01	1.607E-01	1.657E-01	1.352E-01	1.080E-01	6.965E-02	3.004E-02	8.895E-03
2.512E+01	4.194E-02	4.348E-02	3.555E-02	2.779E-02	1.752E-02	7.136E-03	1.943E-03
3.102E+01	3.586E-04	3.891E-04	2.937E-04	2.384E-04	1.335E-04	4.864E-05	1.156E-05

Table 4-11. Fluence spectra of LET in silicon within spherical shells of equivalent aluminum shielding on the Martian surface during the September 29, 1989 solar particle event.

LET, MeV-cm^2/mg	Event fluence (particles/cm^2) with > LET within equivalent aluminum shield of-						
	0	50 mil (1.27 mm)	500 mil (12.7 mm)	1000 mil (25.4 mm)	2000 mil (50.8 mm)	4000 mil (101.6 mm)	7000 mil (177.8 mm)
1.235E-03	1.991E+07	1.956E+07	1.676E+07	1.441E+07	1.112E+07	7.323E+06	4.464E+06
1.525E-03	1.991E+07	1.956E+07	1.676E+07	1.441E+07	1.112E+07	7.323E+06	4.464E+06
1.884E-03	1.937E+07	1.902E+07	1.624E+07	1.392E+07	1.067E+07	6.943E+06	4.171E+06
2.326E-03	1.791E+07	1.757E+07	1.488E+07	1.263E+07	9.522E+06	6.036E+06	3.521E+06
2.873E-03	1.581E+07	1.549E+07	1.295E+07	1.086E+07	8.017E+06	4.928E+06	2.796E+06
3.548E-03	1.323E+07	1.293E+07	1.065E+07	8.799E+06	6.351E+06	3.792E+06	2.108E+06
4.382E-03	1.046E+07	1.021E+07	8.270E+06	6.736E+06	4.762E+06	2.781E+06	1.532E+06
5.412E-03	7.838E+06	7.637E+06	6.095E+06	4.903E+06	3.411E+06	1.967E+06	1.085E+06
6.683E-03	5.616E+06	5.465E+06	4.309E+06	3.434E+06	2.365E+06	1.359E+06	7.570E+05
8.254E-03	3.886E+06	3.780E+06	2.955E+06	2.341E+06	1.605E+06	9.265E+05	5.234E+05
1.019E-02	2.626E+06	2.554E+06	1.986E+06	1.569E+06	1.076E+06	6.271E+05	3.603E+05
1.259E-02	1.746E+06	1.700E+06	1.319E+06	1.042E+06	7.172E+05	4.231E+05	2.475E+05
1.555E-02	1.151E+06	1.123E+06	8.705E+05	6.886E+05	4.770E+05	2.857E+05	1.702E+05
1.920E-02	7.544E+05	7.383E+05	5.731E+05	4.548E+05	3.176E+05	1.932E+05	1.172E+05
2.371E-02	4.937E+05	4.850E+05	3.776E+05	3.009E+05	2.122E+05	1.314E+05	8.120E+04
2.929E-02	3.227E+05	3.189E+05	2.491E+05	1.996E+05	1.423E+05	8.966E+04	5.648E+04
3.617E-02	2.117E+05	2.104E+05	1.650E+05	1.332E+05	9.604E+04	6.158E+04	3.954E+04
4.467E-02	1.394E+05	1.392E+05	1.098E+05	8.930E+04	6.526E+04	4.259E+04	2.789E+04
5.517E-02	9.204E+04	9.262E+04	7.345E+04	6.018E+04	4.458E+04	2.967E+04	1.980E+04
6.813E-02	6.100E+04	6.177E+04	4.929E+04	4.069E+04	3.056E+04	2.076E+04	1.411E+04
8.414E-02	4.049E+04	4.135E+04	3.314E+04	2.759E+04	2.103E+04	1.458E+04	1.010E+04
1.039E-01	2.703E+04	2.775E+04	2.244E+04	1.884E+04	1.456E+04	1.031E+04	7.269E+03
1.283E-01	1.826E+04	1.889E+04	1.536E+04	1.306E+04	1.026E+04	7.414E+03	5.318E+03
1.585E-01	1.242E+04	1.298E+04	1.066E+04	9.137E+03	7.296E+03	5.386E+03	3.950E+03
1.957E-01	8.478E+03	8.977E+03	7.475E+03	6.471E+03	5.257E+03	3.972E+03	2.972E+03
2.417E-01	5.941E+03	6.324E+03	5.294E+03	4.612E+03	3.854E+03	2.958E+03	2.252E+03
2.985E-01	4.226E+03	4.507E+03	3.819E+03	3.358E+03	2.814E+03	2.229E+03	1.703E+03
3.687E-01	3.014E+03	3.208E+03	2.735E+03	2.371E+03	2.010E+03	1.629E+03	1.249E+03
4.553E-01	2.061E+03	2.211E+03	1.846E+03	1.634E+03	1.407E+03	1.143E+03	8.802E+02
5.624E-01	1.212E+03	1.252E+03	1.083E+03	9.813E+02	8.542E+02	7.009E+02	5.550E+02
6.945E-01	8.101E+02	8.344E+02	7.204E+02	6.519E+02	5.661E+02	4.629E+02	3.657E+02
8.577E-01	5.042E+02	5.179E+02	4.462E+02	4.030E+02	3.489E+02	2.843E+02	2.241E+02
1.059E+00	2.842E+02	2.914E+02	2.503E+02	2.254E+02	1.944E+02	1.577E+02	1.240E+02
1.308E+00	1.333E+02	1.367E+02	1.169E+02	1.050E+02	9.010E+01	7.285E+01	5.718E+01
1.616E+00	4.466E+00	4.153E+00	2.867E+00	1.967E+00	1.004E+00	3.187E-01	7.480E-02
1.995E+00	2.719E+00	2.520E+00	1.717E+00	1.164E+00	5.855E-01	1.833E-01	4.283E-02
2.464E+00	1.648E+00	1.525E+00	1.032E+00	6.950E-01	3.466E-01	1.078E-01	2.515E-02
3.043E+00	9.964E-01	9.217E-01	6.209E-01	4.167E-01	2.069E-01	6.408E-02	1.494E-02
3.758E+00	6.001E-01	5.554E-01	3.733E-01	2.500E-01	1.238E-01	3.825E-02	8.899E-03
4.642E+00	3.592E-01	3.327E-01	2.233E-01	1.493E-01	7.380E-02	2.276E-02	5.278E-03
5.733E+00	2.126E-01	1.972E-01	1.323E-01	8.836E-02	4.361E-02	1.341E-02	3.094E-03
7.080E+00	1.233E-01	1.150E-01	7.709E-02	5.146E-02	2.536E-02	7.765E-03	1.778E-03
8.743E+00	6.979E-02	6.546E-02	4.390E-02	2.928E-02	1.440E-02	4.385E-03	9.934E-04
1.080E+01	3.839E-02	3.617E-02	2.423E-02	1.613E-02	7.904E-03	2.386E-03	5.321E-04
1.334E+01	1.997E-02	1.891E-02	1.265E-02	8.406E-03	4.097E-03	1.221E-03	2.668E-04
1.647E+01	9.607E-03	9.156E-03	6.106E-03	4.041E-03	1.953E-03	5.720E-04	1.214E-04
2.034E+01	4.048E-03	3.900E-03	2.583E-03	1.696E-03	8.067E-04	2.289E-04	4.630E-05
2.512E+01	1.198E-03	1.177E-03	7.671E-04	4.963E-04	2.287E-04	6.128E-05	1.137E-05
3.102E+01	1.791E-05	1.839E-05	1.168E-05	7.346E-06	3.248E-06	7.972E-07	1.276E-07

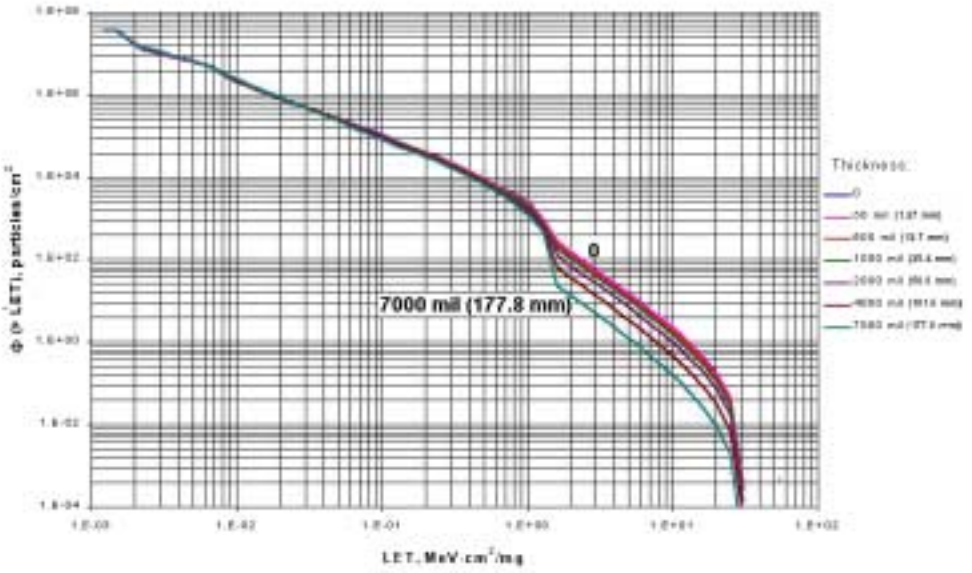

Figure 4-22. Integral LET spectra of particles on the Martian surface produced by the 1980 solar maximum galactic cosmic rays.

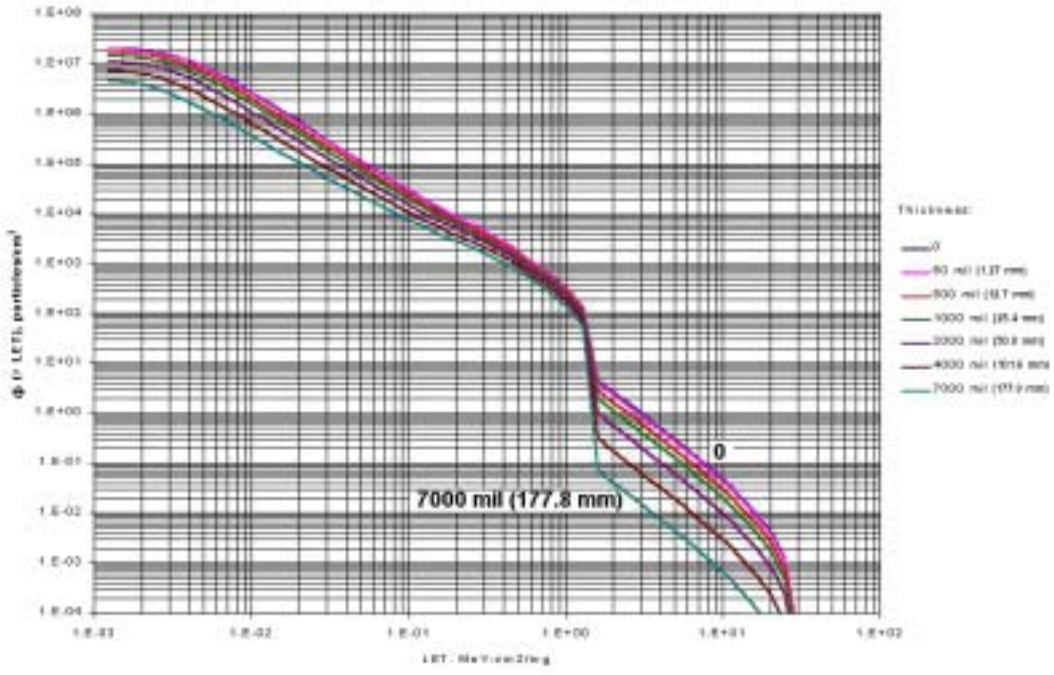

Figure 4-23. Integral LET spectra of particles on the Martian surface produced by the September 29, 1989 solar particle event.

4.6 Solar Radiation at Mars Surface

4.6.1 Ultraviolet (UV) Flux

With no appreciable ozone present (and substantially less massive atmosphere) a considerably larger fraction of top-of-atmosphere UV flux reaches the surface of Mars than on Earth. However, atmospheric carbon dioxide on Mars absorbs essentially all UV at wavelengths shorter than about 2000 Å before it reaches the surface. Figure 4-24 shows variations of UV flux incident at the top of the atmosphere and at the surface with wavelength and season.

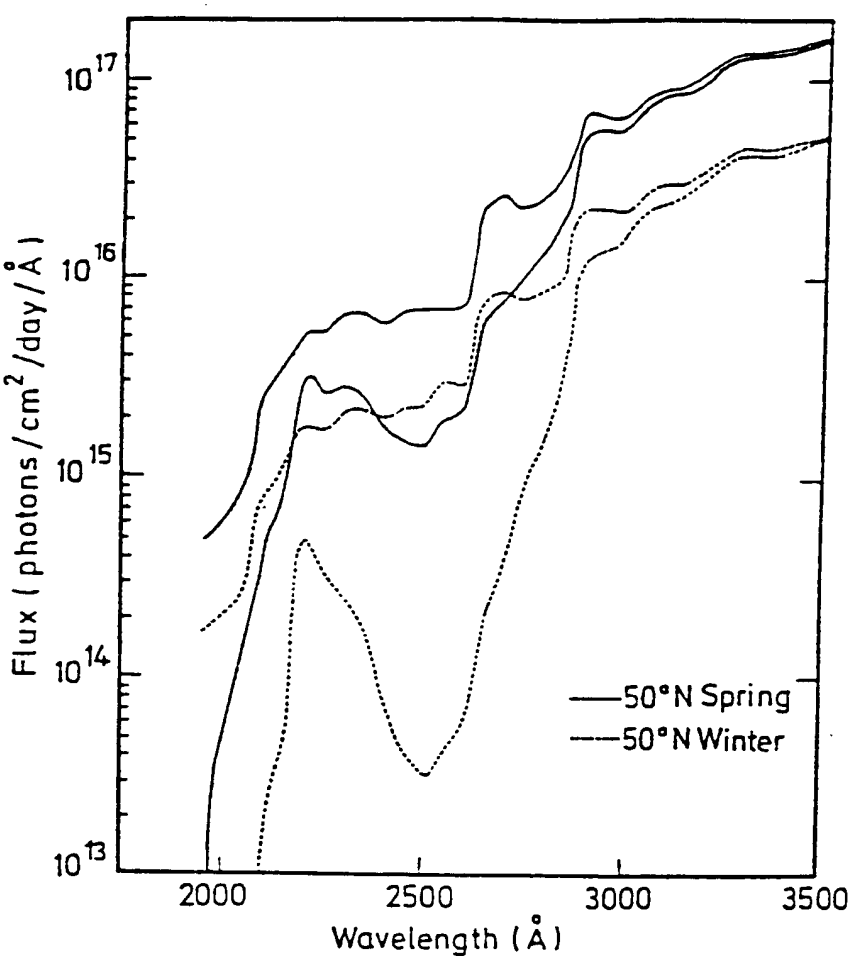

Figure 4-24. UV radiation incident at the top of the Mars atmosphere (upper curve of each latitude pair) and at the surface (lower curve of each latitude pair) versus wavelength and season.[4-44]

4.6.2 Visible and Infrared Radiation

Direct solar irradiance is attenuated by scattering. However, in non-dust-storm conditions the total (direct plus diffuse) radiation received at the surface of Mars is very nearly that received at the top of atmosphere (subject only to the cosine-zenith-angle geometrical effect) (section 3.5.5). Dust storms can cause optical depths in excess of three, blocking essentially all of the direct solar irradiance, and yielding diffuse irradiance at the surface significantly diminished from top-of-atmosphere irradiance. Downwelling infrared radiation at the surface (emitted by the Mars atmosphere) varies from about 25 W/m^2 under relatively clear conditions to about 120 W/m^2 during a major dust storm.

4.7 References

4-1 Smith, D. E., Zuber, M. T., Solomon, S. C., Philips, R. J., Head, J. W., Garvin, J. B., Banerdt, W. B., Muhleman, D. O., Pettengill, G. H., Neumann, G. A., Lemoine, F. G., Abshire, J. B., Aharonson, O., Brown, C. D., Hauck, S. A., Ivanov, A. B., McGovern, P. J., Zwally, H. J., and Duxbury, T. C.: "The Global Topography of Mars and Implications for Surface Evolution." *Science*, Vol. 284, No. 5419, pp. 1495-1503, 1999.

4-2 Smith, D. E., Zuber, M. T., Fray, H. V., et al.: "Topography of the Northern Hemisphere of Mars from the Mars Orbiter Laser Altimeter." *Science*, Vol. 239, No. 5357, pp. 1686-1692, 1998.

4-3 Golombek, M.P. and Cook. R. A., Moore, H. J., and Parker, T. J.: "Selection of the Mars Pathfinder landing site." *J. Geophys. Res*, Vol. 102, No. E2, pp. 3967-3988, 1997.

4-4 Keating, G. M., Bougher, S. W., Zurek, R. W., et al.: "The Structure of the Upper Atmosphere of Mars: In situ Accelerometer Measurements from Mars Global Surveyor." *Science*, Vol. 279, No. 5357, pp. 1672-1676, 1998.

4-5 Bills, B. G. and Ferrari, A. J.: "Mars Topography, Harmonies, and Geophysical Implications." *J. Geophys. Res*., Vol. 83, pp. 3497-3508, 1978.

4-6 Balmino, G., Moynot, G. and Vales, N.: "Gravity Field Model of Mars in Spherical Harmonics." *J. Geophys. Res*., Vol. 87, pp. 9735-9746, 1982.

4-7 Bell III, J. F., McSween Jr., H. Y., Crisp, J. A., et al.: "Mineralogic and Compositional Properties of Martian Soil and Dust: Results From Mars Pathfinder." Submitted to *J. Geophys. Res*, 1999.

4-8 Squyres, S. W., Clifford, S. M., Kuzmin, R. O., Zimbelman, J. R., and Costard, F.M.: "Ice in the Martian Regolith" in Mars, Kieffer, H. H., B. M. Jakosky, C. W. Synder, M. S. Mathews (eds), Univ. of Arizona Press, Tucson, pp. 523-554, 1992.

4-9 Greeley, R., Kraft, M., Sullivan, R., Wilson, G., Bridges, N., Herkenhoff, K., Kuzmin, R.O., Malin, M., and Ward, W.: "Aeolian Features and Processes at the Mars Pathfinder Site." *J. Geophys. Res.*, Vol. 104, No. E4, pp. 8573-8584, 1995.

4-10 Strom, R. G., Croft, S. K. and Barlow, N. G.: "The Martian Impact Cratering Record" in Mars, Kieffer, H. H., B. M. Jakosky, C. W. Synder, M. S. Mathews (eds), Univ. of Arizona Press, Tucson, pp. 383-423, 1992.

4-11 Moore, H. J.: "Estimates of Some Physical/Mechanical Properties of Martian Rocks and Soil-like Materials." USGS Open-File Report 91, 568, 1991.

4-12 Rover Team: "Characterization of the Martian Surface Deposits by the Mars Pathfinder Rover, Sojourner." *Science*, Vol. 278, No. 5344, pp. 1765-1768, 1997.

4-13 Moore, H. J., Bickler, D. B., Crisp J. A., Eisen, H. J., Gensler, J. A., Haldemann, A. F. C., Matijevic, J. R., Reid, L. K., and Pavlics, F.: "Soil-like Deposits Observed by Sojourner, The Pathfinder Rover." *J. Geophys. Res*., Vol. 104, No. E4, pp. 8729-8746, 1999.

4-14 Mendell, W., Plescia, J., and Tribble, A.: "Surface Environments, in Human Space Flight Analysis and Design (Draft)." McGraw-Hill, 1999.

4-15 Moore, H. J., Hutton, R. E., Clow, G. D., and Spitzer, C. R.: "Physical Properties of the Surface Materials at the Viking Landing Sites on Mars." USGS Prof. Paper. 1389, U.S. Gov. Printing Office, Washington, D.C., 222 pp., 1987.

4-16 Rover Team: "Characterization of the Martian Surface Deposits by the Mars Pathfinder Rover, Sojourner." *Science*, Vol. 278, No. 5344, pp.1765-1768, 1997.

4-17 Moore, H. J., Clow, G. D., and Hutton, R. E.: "A Summary of Viking Sample-Trench Analyses for Angles of Internal Friction and Cohesion." *J. Geophys. Res.*, Vol. 87, pp. 10 043 - 10 050, 1982.

4-18 Arvidson, R. E., Gooding, J. L., and Moore, H. J. "The Martian Surface as Imaged, Sampled, and Analyzed by the Viking Landers." *Rev. Geophys. Space Phys.*, Vol. 27, pp. 39-60, 1989.

4-19 Moore, H. J. and Jakosky, B. M. "Viking Landing Sites, Remote Sensing Observations, and Physical Properties of Martian Surface Materials." *Icarus*, Vol. 81, pp. 164-184, 1989.

4-20 Banin, A., Clark, B. C., and Wanke, H.: "Surface Chemistry and Mineralogy" in Mars, Kieffer, H. H., B. M. Jakosky, C. W. Synder, M. S. Mathews (eds), Univ. of Arizona Press, Tucson, pp. 594-625, 1992.

4-21 Rieder, R., Wänke, H., Economou, T., and Turkevich, A. "Determination of the Chemical Composition of Martian Soil and Rocks: The Alpha Proton X-ray Spectrometer." *J. Geophys. Res*, Vol. 102, pp. 4027-4044, 1997.

4-22 Golombek, M. P., Banerdt, W. B., Tanaka, K. L., and Tralli, D. M.: "A Prediction of Mars Seismicity from Surface Faulting." *Science*, Vol. 258, pp. 979-981, 1992.

4-23 Golombek, M.P. and Rapp, D. "Size-frequency Distributions of Rocks on Mars and Earth Analog Sites: Implications for Future Landed Missions." *J. Geophys. Res*, Vol. 102, No. E2, 1997.

4-24 Golombek, M. P., Moore, H. J., Haldemann, A. F. C., Parker, T. J., and Schofield, J. T.: "Assessment of Mars Pathfinder Landing Site Predictions." *J. Geophys. Res.*, Vol. 104, No. E4, pp. 8585-8594, 1999.

4-25 Jakosky, B. M. and Christensen, P. R.: "Are the Viking Landing Sites Representative of the Surface of Mars." *Icarus*, Vol. 66, pp. 125-133, 1986.

4-26 Kieffer, H. H., Martin, T. Z., Peterfreund, A. R., Jakosky, B. M., Miner, E. D., and Palluconi, F.: "Thermal and Albedo Mapping of Mars During the Viking Primary Mission." *J. Geophys. Res.*, Vol. 82, No. 28, pp. 4249-91, 1977.

4-27 Christensen, P. R. and Moore, H. J.: "The Martian Surface Layer" in Mars, Kieffer, H. H., B. M. Jakosky, C. W. Synder, M. S. Mathews (eds), Univ. of Arizona Press, Tucson, pp. 686-729, 1992.

4-28 Christensen, P. R. and Malin, M. C.: "High Resolution Thermal Imaging of Mars." (abstract) *Lunar and Planet. Sci.*, Vol. XIX, pp. 180-181, 1988.

4-29 Kieffer, H. H., Martin, T. Z., Peterfruend, A. R., Jakosky, B. M., Miner, E. D., and Palluconi, F. D.: "Thermal and Albedo Mappings of Mars During the Viking Primary Mission." *J. Geophys. Res.*, Vol. 82, pp.4249-4291, 1977.

4-30 Palluconi, F. D. and Kieffer, H. H.: "Thermal Inertial Mapping from 60°S to 60°N." *Icarus*, Vol. 45, pp. 415-426, 1981.

4-31 Campbell, M. J. and Ulrichs, J.: "Electrical Properties of Rocks and Their Significance for Lunar Radar Observations." *J. Geophys. Res.*, Vol. 74, pp. 5867-5881, 1969.

4-32 Olhoeft, G. R. and Strangway, D. W.: "Electrical Properties of the Surface Layers of Mars." *Geophysical Research Letters*, Vol. 1, No. 3, pp. 141-143, 1975.

4-33 Christensen, P. R., Anderson, D. L., Chase, S. C., et al.: "Thermal Emission Spectrometer Experiment: Mars Observer Mission." *J. Geophys. Res.*, Vol. 97, No. E5, pp. 7719-7734, 1992.

4-34 Simpson, R. A.: "Spacecraft Studies of Planetary Surfaces Using Bistatic Radar." *IEEE Transactions on Geoscience and Remote Sensing*, Vol. 31, No. 2, pp. 465-482, 1993.

4-35 Simpson, R. A., Harmon, J. K., Zisk, S. H., Thompson, T. W., and Muhleman, D. O.: "Radar Determination of Mars Surface Properties", in Mars, Kieffer, H. H., B. M. Jakosky, C. W. Synder, M. S. Mathews (eds), Univ. of Arizona Press, Tucson, pp. 652-685, 1992.

4-36 Webb, S. and Quenby, J. J.: "Numerical Studies of the Transport of Solar Protons in Interplanetary Space." *Planetary and Space Science*, Vol. 21, No. 1, pp. 23-42, 1973.

4-37 Badhwar, G. D., Cucinotta, F. A. and O'Neill, P. M.: "An Analysis of Interplanetary Space Radiation Exposure for Various Solar Cycles." *Radiat. Res.*, Vol. 138, pp. 201-208, 1994.

4-38 Wilson, J. W., Kim, M. H. Y., Shinn, J. L., Tai, H. and Cucinotta, F. A.: "Solar Cycle Variation and Application to the Space Radiation Environment." NASA/TP-1999-209369, 1999.

4-39 M.-H. Y. Kim et al. (1999): "Contributions of High Charge and Energy (HZE) Ions during Solar-particle Event of September 29, 1989." NASA TP 1999-209320.

4-40 Committee on Space Research (COSPAR): "The Mars Reference Atmosphere." *Advances in Space Research*, Vol. 2, No. 2, pp.1-106, 1982.

4-41 Kim, M.-H. Y. et al.: "Comparison of Martian Meteorites and Martian Regolith as Shield Materials for Galactic Cosmic Rays." NASA TP 1998-208724, 1998.

4-42 Wilson, J. W., Miller, J., Konradi, A. and Cucinotta, F. A., Editors: "Shielding Strategies for Human Space Exploration." NASA CP-3360, 1997.

4-43 S. Clowdsley et al.: "An Improved Elastic and Non-elastic Neutron Transport Algorithm for Space Radiation." NASA TP 1999-3335, 1999.

4-44 Kuhn, W. R., Atreya, S. K., and Postawko, S. E.: "The Influence of Ozone on Martian Atmospheric Temperatures." *J. Geophys. Res.*, Vol. 84, pp. 8341-8342, 1979.

5.0 CONCLUSIONS AND RECOMMENDATIONS

5.1 Interplanetary Environment Effects

Ionizing radiation from Solar Proton Events (sections 2.2.1 and 2.2.2) and from Galactic Cosmic Rays (section 2.2.3) has a potential for producing radiation damage to electronic systems and serve as a threat to astronaut health and safety. Meteoroid impacts (section 2.3) also represent a potential hazard for spacecraft systems and astronauts. Meteor streams (section 2.3.4), associated with debris from comets, have different frequency and timing than on Earth. Since Mars is visited by about twice as many comets as Earth, meteor flux from associated meteor streams is projected to be correspondingly larger for Mars and near-Mars environments than for Earth.

5.2 Atmospheric Environment Effects

Several environmental factors encountered in the atmosphere of Mars, discussed in section 3, have potentially large impacts on spacecraft systems including the following:

- Cold near-surface air temperatures and large daily temperature swings
- Dust deposition in light wind conditions[5-1] (Pathfinder observed a few tenths of a percent solar array performance degradation per sol)
- Potentially high winds with possible wind-blown dust
- Possible magnetic and electrostatic effects of dust[5-2]
- Uncertainties in predicting dust storm onset, growth, and dissipation
- Large atmospheric density uncertainties for aerocapture planning and performance
- Large density and wind uncertainties for precision landing planning and performance
- Large density variations during aerobraking operations

5.3 Mars Surface Environment Effects

General terrain characteristics such as crater density (section 4.2.2) and distribution of rocks and boulders (section 4.3) have been fairly well characterized. Basic soil mechanical properties (e.g., bearing strength for construction of surface facilities, tendency to rut and washboard during rover operations) are also fairly well defined (section 4.2.3). Some chemical characteristics of Martian soil are known (section 4.2.5). However, significant uncertainties remain, such as potential soil toxicity to astronauts, potential for adverse mechanical and electrical effects caused by long-duration operations in a Mars dust environment, and details of radiation shielding potential for Martian soil.

To date, all estimates of ionizing radiation exposure at the surface are based on models (section 4.5). Ability to estimate such exposures is expected to improve dramatically after data is obtained from both orbiting and surface-based radiation detectors now delayed from their original

schedule on the Mars Surveyor Program 2001 mission. Total mass of the Martian atmosphere varies by more than 30 percent during the course of a Mars year (mass is proportional to pressure; figure 3.7 is a plot of annual variation). Capability of the atmosphere to shield from both UV and ionizing radiation exposure at the surface, therefore, is expected to have a similar range of annual variability.

5.4 Recommendations for Future Work

In order to improve the fidelity and completeness of the environment definitions in this document, several areas for further work are recommended.

5.4.1 Meteor Streams

Comet orbits which pass near the interplanetary cruise phase trajectories (Earth to Mars and Mars to Earth) should be computed to determine the likelihood of encountering known meteor streams. A later improvement to these calculations could be made by considering particle ejection from the comets and subsequent planetary and radiation pressure perturbation of the particle orbits over hundreds of years. This type of modeling has led to great improvements in prediction of meteor storms such as the Leonids.

5.4.2 Meteoroid Flux in Mars Atmosphere and at Surface

Ability of the Martian atmosphere to shield surface inhabitants from meteors will differ somewhat from Earth's atmospheric shielding capability. Atmospheric density at 100 km altitude (capable of burning up many smaller meteors) is roughly comparable on the two planets. However, because of lower total atmospheric mass, a larger fraction of interplanetary meteor flux will be able to reach the surface of Mars. Details of this meteoroid flux, and its dependence on meteor size and speed should be quantified. Also the question of whether meteor ion trails near 100 km could be used for radio communication on Mars (as can be on Earth) should be documented.

5.4.3 Mars Surface Ionizing Radiation

The radiation transport calculations through the Martian atmosphere assumed a single atmospheric density model. Future calculations should be performed using the Mars-GRAM model for maximum and minimum atmospheric density. Additionally, calculations should be performed for a range of altitudes in the atmosphere, from the bottom of Valles Marineris to the top of Olympus Mons, to bound the environments to be encountered during surface exploration sorties.

5.4.4 Mars Ionosphere and Radio Propagation

This document contains only a cursory description of the Martian ionosphere. The next update should include a more complete description, including data necessary to assess the use of high frequency (i.e., shortwave) radio propagation for communication between various surface locations.

5.4.5 Triboelectric Charging Effects

Studies of triboelectric charging effects of dust in the Mars atmosphere[5-3 5-4] should be assessed and summarized, including characteristics and potential adverse effects of electric

charging and discharge phenomena. Ability of charged dust to exacerbate mechanical wear and abrasion on surface systems should be examined.[5-5] The possibility and characteristics of lightning on Mars[5-3] should be assessed and summarized. For Mars exploration charging effects could be particularly significant if future plans materialize to use aircraft or balloon-borne sensors.[5-6]

5.4.6 Atmospheric Circulation and Wind Systems

Further details of atmospheric circulation systems and wind regimes on Mars need to be discussed in terms of engineering and system design impacts. Particularly relevant are details of effects of wind-borne dust and winds on possible aircraft or balloon systems, or possible large-scale inflatable structures, such as habitation modules.

5.4.7 Summary and Availability of Mars Environmental Models

An extensive summary is planned for describing available computer models for characterizing environments relevant to Mars missions. These models could include the following:

- Interplanetary ionizing radiation model
- Interplanetary meteoroid flux model
- Quantitative, spherical harmonic model of Mars gravitational field
- Models of Mars atmospheric temperature, pressure, density, winds (surface to thermosphere)
- Model of charge density in Mars ionosphere and its dependence on solar wind and EUV flux
- Quantitative model of Mars dust characteristics (physical and optical)
- Model of ionizing radiation at the surface of Mars
- Model of meteoroid flux within the atmosphere and at the surface of Mars
- Engineering model of Mars soil characteristics relevant to construction or operation of surface-based systems on Mars
- Quantitative model of solar and infrared radiation at the surface of Mars

Model summaries will include a brief description of the capabilities and operating characteristics of each model, contact information for obtaining the model and its operating instructions (for those models available for distribution), or contact information on how to have model evaluations done by the model's developers (for models too complex to be run by "casual users").

5.4.8 Technical Glossary and Index

A glossary of technical terms will be developed, with an index (or cross-reference) to section(s) where details of these terms are discussed in the document.

5.5 References

5-1 Landis, G.: "Dust Obscuration of Solar Arrays." *Acta Astronautica,* Vol. 38, No. 11, pp. 895-891, 1996.

5-2 Hviid, S. F., Madsen, M. B., Ginnlaugsson, H. P., et al.: "Magnetic Properties Experiments on the Mars Pathfinder Lander: Preliminary Results." *Science*, Vol. 278, No. 5344, pp. 1768-1770, 1997.

5-3 Kolecki, J. C. and Landis, G. A.: "Electrical Discharge on the Martian Surface", at http://satori2.lerc.nasa.gov/DOC/marslight.html, 1996.

5-4 Ferguson, D. C., Kolecki, J. C., Siebert, M. W., et al.: "Evidence for Martian Electrostatic Charging and Abrasive Wheel Wear from the Wheel Abrasion Experiment on the Pathfinder Sojourner rover." *J. Geophys. Research*, Vol.104, No. E4, pp.8747-8759, 1999.

5-5 Farrell, W. M., Kaiser, M. L., Desch, M. D., et al.: "Detecting Electrical Activity from Martian Dust Storms." *J. Geophys. Research*, Vol.104, No. E2, pp. 3795-3801, 1999.

5-6 Garg, S. C. and John, T.: "Balloon Gondola Charging and Its Estimation." *Adv. Space Research*, Vol.17, No.11, pp.99-102, 1996.

Appendix A

Basic Physical Data for Mars

The following data were taken from Mars, University of Arizona Press, H.H. Kieffer, et al., Editors, 1992. Notes to specific values are in regular parentheses at the end of each of 11 tables; references are in square brackets and listed at the end of this appendix.

Table A-1. Orbital Characteristics

Heliocentric osculating elements referred to the mean ecliptic and equinox of J2000.0, for Julian Date 2 448 120.5, 1990 Aug 17.

Semimajor axis	1.52366 AU	[A-1]
Perihelion	1.381 AU	
Aphelion	1.666 AU	
Eccentricity	0.0934	[A-1]
Inclination	$1^{\circ}.8504$	[A-1]
Longitude of ascending node	$49^{\circ}.59$	[A-1]
Longitude of perihelion	$335^{\circ}.94$	[A-1]
Mean daily motion	$0^{\circ}.52405$ / day	[A-1]
Mean longitude	$0^{\circ}.89$	[A-1]
Mean orbital velocity around Sun (calculated from mean semimajor axis)	$24.13\ \mathrm{km\ s^{-1}}$	
L_s of perihelion	$250^{\circ}.87$	

Table A-2. Orientation of Polar Axis

Right ascension	$317^{\circ}.61$	[A-1]
Declination	$52^{\circ}.85$	[A-1]
Obliquity relative to orbital plane	$25^{\circ}.19$	[A-1]

Table A-3. Time Properties

Length of sidereal day	24 h, 37 m, 22.663 ± 0.002 s	[A-2]
	88642.663 ± 0.002 s	[A-2]
Mean orbital period (1)	686.98 Earth days 668.60 Mars solar days	
Length of mean solar day (2)	88775.2 s	

Notes:

Table 1976- . Calculated from mean semimajor axis and Kepler's third law.

Table 1976- . Calculated from length of sidereal day and mean orbital period

Table A-4. Geophysical Parameters

Mass			
GM		42 828.3 ± 0.1 km^3s^{-2}	[A-3]
Mass		6.4185×10^{23} kg	[A-4]
Mean radius (radius of sphere of equal volume)		3389.92 ± 0.04 km	[A-5]
Radius and direction of principal axes of 2nd –degree triaxial ellipsoid: (given as radius, latitude, longitude)			[A-5]
3394.5 ± 0.3 km;	0°.7 ± 0.2,	18°.5 ± 0.8W	
3399.2 ± 0.3 km;	−2°.0 ± 0.2,	108°.4 ± 0.8W	
3376.1 ± 0.4 km;	87°.9 ± 0.2,	128°.8 ± 6.3W	
Volume (1)		1.6318×10^{22} m^3	[A-5]
Mean density		3.9335 ± 0.0004 g cm^{-3}	[A-4]
J_2		1960.454×10^{-6}	[A-1]
C/MR^2		0.345-0.365	[A-6, A-7, A-8]
Center of mass/center of figure offset		2.50 ± 0.07 km	[A-4]
cf. Offset in direction of −62°.0 ± 3.7 lat, 87°.7 ± 3.0 (long W)			
Magnetic dipole moment		$< 10^{-4}$ that of Earth $<8 \times 10^{11}$ T m^{-3}	[A-9]
Surface gravity at pole (2)		3.758 m s^{-2}	
Surface gravity at Equator (2)		3.711 m s^{-2}	
Ratio of surface gravity at Equator to Earth surface gravity at Equator		0.3795	
Mean escape velocity (3)		5.027 km s^{-1}	[A-5]
Total surface area (1)		1.4441×10^{14} m^2	[A-5]
Ratio of total surface area to that on Earth		0.2825	[A-10]
Ratio of total surface area to Land surface area on Earth		0.976	[A-10]
Area of perennial polar caps			[A-26]
south polar region		88 000 km^2	
north polar region		837 000 km^2	
Area of polar layered terrain: (4)			[A-26]
south polar region		1 395 000 km^2	
north polar region		395 000 km^2	

Notes:
(1) Calculated from radius of sphere of equal volume.
(2) Given by GM/R^2; equatorial value based on mean equatorial radius.
(3) Given by $\sqrt{2GM / R}$.
(4) Excluding area of perennial polar caps.

Table A-5. Atmospheric Composition (by Volume)

Species	Abundance	Notes
CO_2	0.9532	(1)
N_2	0.027	
Ar	0.016	
O_2	0.0013	
CO	0.0007	
H_2O	0.0003	(2)
Ne	2.5 ppm	
Kr	0.3 ppm	
Xe	0.08 ppm	
O_3	0.04 to 0.2 ppm	(2)

Notes:
(1) Because CO_2 varies seasonally due to condensation at the polar caps, all abundances vary seasonally by as much as about 30%; values are those measured at the Viking landing sites and are relative to a total pressure of 7.5 mbar.
(2) Abundance varies with season and location. Annual global average of H_2O is ~ 10×10^{-3} kg m^{-2} or 0.000 16 by volume. [A-25]

Table A-6. Atmospheric Isotopic Ratios

Ratio	Earth	Mars
$^{12}C/^{13}C$	89	90 ± 5
$^{14}N/^{15}N$	272	170 ± 15
$^{16}O/^{18}O$	489	490 ± 25 (measured in atmospheric CO_2)
$^{36}Ar/^{38}Ar$	5.3	5.5 ± 1.5
$^{40}Ar/^{36}Ar$	296	3000 ± 500
$^{129}Xe/^{132}Xe$	0.97	2.5^{+2}_{-1}
D/H	1.6×10^{-4}	$(9 \pm 4) \times 10^{-4}$

Table A-7. Representative Chemical Composition of Soil

Constituent (1)	Concentration (%)	
SiO_2	43.4	(2)
Fe_2O_3	18.2	(2)
Al_2O_3	7.2	(2)
SO_3	7.2	(2)
MgO	6.0	(2)
CaO	5.8	(2)
Na_2O	1.34	(3)
Cl	0.8	(2)
P_2O_5	0.68	(3)
TiO_2	0.6	(2)
MnO	0.45	(3)

Cr_2O	0.29	(3)
K_2O	0.10	(3)
CO_3	<2	(4)
H_2O	0-1	(5)

Notes:

(1) Based on elemental composition, expressed as oxides.
(2) Based on direct soil analyses from Viking X-ray Fluorescence Spectrometer.
(3) Based on SNC meteorite analyses.
(4) Based on terrestrial simulations of Viking Labelled Release experiment.
(5) Spatially and temporally variable.

Table A-8. Atmospheric Properties

Atmospheric pressure at surface (1)	5.6 mbar or 560 Pa	
Average columnar mass of atmosphere (2)	150 kg m^{-2}	
Average mass of atmosphere (3)	2.17×10^{16} kg	
Mass of seasonal polar cap deposits: (4)		[A-13]
north polar cap	3.5×10^{15} kg	
south polar cap	8.1×10^{15} kg	
Mean atmospheric scale height (at T = 210 K)	10.8 km	[A-14]
Dry adiabatic lapse rate	4.5 K km^{-1}	[A-14]
Mean atmospheric lapse rate (observed)	~ 2.5 K km^{-1}	[A-14]
Atmospheric visible optical depth (5)	0.1-10	[A-14]

Notes:

(1) Seasonally and spatially variable; this value is an estimate of the global annual average.
(2) Calculated from 5.6-mbar surface pressure and global-average gravity.
(3) Calculated from mean global surface pressure of 5.6 mbar.
(4) Based on seasonal variations in atmospheric pressure.
(5) Temporally and spatially variable; values are approximate, integrated over entire visible or infrared spectrum, respectively.

Table A-9. Thermal Properties

Solar constant:		
at 1 AU (1)	1367.6 W m-2	[A-15]
at mean Mars distance from Sun	588.98 W m-2	
Average surface temperature (2)	210.1 K	
Range of surface temperature	~ 140-300 K	[A-16]
Surface bolometric albedo (3)		
mean	0.25	[A-17]
range	0.08-0.40	[A-17]

Surface thermal inertia: (4)

mean	6.5×10^{-3} cal $cm^{-2}s^{-1/2}$ K^{-1}	[A-18]
	272. J $m^{-2}s^{-1/2}$ K^{-1}	
range	$1 - 15 \times 10^{-3}$ cal $cm^{-2}s^{-1/2}$ K^{-1}	[A-18]
	42. - 628 J $m^{-2}s^{-1/2}$ K^{-1}	

Notes:

(1) Mean of measurements from SMM/ACRIM I experiment, 1980-1983.
(2) Equilibrium for a perfectly conducting sphere of albedo = 0.25, emissivity = 1.0 at Mars mean heliocentric distance.
(3) As measured at ~ 60-km spatial scale.
(4) As measured at ~ 100-km spatial scale.

Table A-10. Viking and Pathfinder Landing Site Locations

	VL-1	VL-2	MPF	
Date	7/20/76	9/3/76	7/4/97	
Time	11:53UT	22:58UT	16:57UT	
Local Mars Time	16:13LST	09:49LST	02:58LST	
Latitude (1)	22°.480 ± 0.003	47°.967 ± 0.003	19.17	[A-24]
Longitude (1)	47°.968 ± 0.01	225°.737 ± 0.1	33.21	[A-24]
Radius to surface	3389.32 ± 0.06	3381.86 ± 0.06 km	3389.73	[A-24]
Elevation relative to geoid (2)	-1.54	-2.44 km	-1.62	
Average annual surface pressure	~ 780	~ 870 Pa	-	

Notes :

(1) Areographic coordinates. Longitude depends upon the precise location of Airy-0. Inertial longitude known to +0°.002.
(2) Relative to fourth order and degree datum described in [17], using the radii at sites listed here. The approximate elevations shown on the U.S. Geological Survey (1991) topographic maps I-2160 are –1.9 km and –0.8 km, respectively. The landing sites were not used as part of the vertical control system for these maps.

Table A-11. Satellites

	Phobos	Deimos	Unit	
Radii of triaxial ellipsoid: a:	13.3 ± 0.3	7.6 ± 0.5	km	[A-20]
b:	11.1 ± 0.3	6.2 ± 0.5	km	[A-20]
c:	9.3 ± 0.3	5.4 ± 0.5	km	[A-20]
Volume	5680 ± 250	1052 ± 250	km^3	[A-18, A-19]

Mass:				
GM	$(7.22 \pm 0.05) \times 10^{-4}$	$(1.2 \pm 0.1 \times 10^{-4}$	km^3s^{-2}	[A-22, A-2_]
M	1.08×10^{16}	1.8×10^{15}	kg	
Mean density 1.905	1.905 ± 0.053	1.7 ± 0.5	g cm^{-3}	
Orbital elements:				
Semimajor axis	9378.5	23 458.8	km	[A-22]
Eccentricity	0.0152	0.0002		[A-22]
Inclination	1.03	1.83	deg	[A-22]
Orbital period	0.318 910 23	1.262 440 7	day	[A-1]
Rate of decrease of longitude of ascending node	158.8	6.614	deg yr^{-1}	[A-1]
Length of day	synchronous	synchronous		[A-1]

References cited in preceding tables:

A-1. The Astronomical Almanac for 1990.

A-2. Mayo et al.: "Lander locations, Mars physical ephemeris, and solar system parameters: Determination from Viking Lander tracking data." *J. Geophys. Res.*, Vol. 82, pp. 4298-4303, 1977.

A-3. Null, G. W.: "A Solution for the Mass and Dynamical Oblateness of Mars using Mariner IV Doppler Data." *Bull. Amer. Astron. Soc.*, Vol. 1, pp. 356 (abstract) , 1969.

A-4. Esposito, P. B., et al.: "Gravity and Topography." Chapter 7 of Mars by Kieffer, H. H., et al. Tuscon: University of Arizona Press, pp. 209-248, 1992.

A-5. Bills, B. G. and Ferrari, A. J.: "Mars topography, Harmonics and Geophysical Implications." *J. Geophys. Res.*, Vol. 83, pp. 3498-3508, 1978.

A-6. Bills, B. G.: "The Moments of Inertia of Mars." *Geophys. Res. Lett.*, Vol. 16, pp. 385-388, 1989.

A-7. Bills, B. G.: "Comment on "More About the Moment of Inertia of Mars." *Geophys. Res. Lett.*, Vol. 16, pp. 1337-1338, 1989.

A-8. Kaula, W. M., et al.: "More about the Moment of Inertia of Mars." *J. Geophys. Res.*, Vol. 84, pp. 999-1008, 1989.

A-9. Luhmann, J. G., et al.: "The Intrinsic Magnetic Field and Solar-Wind Interaction of Mars." Chapter 31 of Mars by Kieffer, H. H., et al. Tuscon: University of Arizona Press, pp. 1090-1134, 1992.

A-10. Stacey, F. D.: "Physics of the Earth." 2nd edition (New York: Wiley), 1977.

A-11. Owen, Tobias: "The Composition and Early History of the Atmosphere of Mars." Chapter 25 of Mars by Kieffer, H. H., et al. Tuscon: University of Arizona Press, pp. 818-834, 1992.

A-12. Banin, A., et al.: "Surface Chemistry and Mineralogy." Chapter 18 of Mars by Kieffer, H. H., et al. Tuscon: University of Arizona Press, pp. 594-625, 1992.

A-13. Hess, S. L. et al.: "The Annual Cycle of Pressure of Mars Measured by Viking Landers 1 and 2." *Geophys. Res. Lett.*, Vol. 7, pp. 197-200, 1980.

A-14. Zurek, R. W., et al.: "Dynamics of the Atmosphere of Mars." Chapter 26 of Mars by Kieffer, H. H., et al. Tuscon: University of Arizona Press, pp. 835-933, 1992.

A-15. Willson, R. C.: "Measurements of Solar Total Irradiance and Its Variability." *Space Sci. Rev.*, Vol. 38, pp. 203-242, 1984.

A-16. Kieffer, H. H. et al.: "Thermal and Albedo Mapping on Mars during the Viking Primary Mission." *J. Geophys. Res.*, Vol. 82, pp. 4249-4291, 1977.

A-17. Pleskot, L. K. and Miner, E. D.: "Time Variability of Martian Bolometric Albedo." *Icarus*, Vol. 45, pp. 179-201, 1981.

A-18. Palluconi, F. D. and Kieffer, H. H.: "Thermal Inertia Mapping of Mars for 60°S to 60°N." *Icarus*, Vol. 45, pp. 415-426, 1981.

A-19. Wu, S. S. C.: "A Method of Defining Topographic Datums of Planetary Bodies." *Ann. Geophys.*, 1981, Vol. 1, pp. 147-160.

A-20. Duxbury, T. C., et al.: "Geodesy and Cartography of the Martian Satellites." Chapter 36 of Mars by Kieffer, H. H., et al. Tuscon: University of Arizona Press, pp. 1249-1256, 1992.

A-21. Duxbury, T. C.: "An Analytic Model for the Phobos Surface." *Planet. Space Sci.*, Vol. 39, pp. 355-376, 1991.

A-22. Kolyka, Y. et al.: "International Project PHOBOS Experiment." *Planet. Space Sci.*, Vol. 39, pp. 349-354, 1991.

A-23. Williams, B. et al.: "Improved Determination of Phobos and Deimos Masses from Viking Flybys." *Lunar Planet. Sci.*, Vol. XIX, p. 1274 (abstract), 1988.

A-24. Michael, W. H., Jr.: "Viking Lander Tracking Contributions to Mars Mapping." *Moon and Planets*, Vol. 20, pp. 149-152, 1978.

A-25. Jakosky, B. M. and Farmer, C. B.: "The Seasonal and Global Behavior of Water Vapor in the Mars Atmosphere: Complete Global Results of the Viking Atmospheric Water Detector Experiment." *J. Geophys. Res.*, Vol. 87, pp. 2999-3019, 1982.

A-26. Tanaka, K. L. et al.: "A Synthesis of Digitized, Viking-based Geology." *Proc. Lunar Planet. Sci. Conf.*, Vol. 18, pp. 665-678, 1988.

Appendix B

Tables of Parameters for Earth and Mars

The following information was summarized from "Standard Planetary Information, Formulae, and Constants" (http://atmos.nmsu.edu/jsdap/encyclopediawork.html), from the NASA Planetary Data System at New Mexico State University. Encyclopedia Author: Chris Barnet, HTML Editor-Steve Duran, Webmaster Lyle Huber.

Table B-1. Parameters for Earth and Mars

Table 1976- . **Planet Size Information**

	Area km^2	Volume km^3	Mass grams	Mass $M_\oplus$	density gm/cm^3
Earth	5.1006×10^{8}	1.0832×10^{12}	5.9790×10^{27}	1.000	5.520
Mars	1.4416×10^{8}	1.6275×10^{11}	6.4570×10^{26}	0.108	3.967

Table 1976- . **Planet Rotation Period**

	Hours	hr:mn:secs	day/earth	°/day
Earth	23.933 333 0	23:56: 0.0	0.997 22	361.002 791
Mars	24.633 333 0	24:38: 0.0	1.026 39	350.744 254

Table 1976- . **IOrbital Parameters**

	a(AU)	period(yrs)	inclin(°)	a.node(°)	arg.perih(°)	ecc	L(6430)(°)
Earth	1.0000	1.00	0.00	0.00	102.77	0.016 704	99.372
Mars	1.5237	1.88	1.85	49.45	335.82	0.093 329	195.082

Table 1976- . **Planet Pole**

	<r>(AU)	inclination(°)	RA(°)	DEC(°)
Earth	1.0000	23.40	0.00	90.00
Mars	1.5237	25.20	317.57	57.52

Table 1976- . **Velocity**

	V_{orbit} km/s	V_{escape} km/s	$V_{equator}$ km/s	V_{sound} km/s
Earth	29.786	11.192	0.465	0.320
Mars	24.130	5.045	0.240	0.227

Table 1976- . **Radiatively Effective Atmospheric Parameters (T_{eff},$P_{eff, etc.}$)**

	T_{eff} K	P_{eff} mbar	ρ gm/cm^3	H km	V_{sound} m/s	τ_{rad} years	phase °
Earth	255.0	500.000	$6.8297 \times 10\text{-}^{4}$	7.471	320.2	0.131	39.47
Mars	210.0	6.000	$1.5124 \times 10\text{-}^{5}$	10.605	226.6	0.006	1.17

Table 1976- . **Stratopause Values**

	T K	P mbar	ρ gm/cm^3	H km	V_{sound} m/s	τ_{rad} years	phase °
Earth	270.0	1.000	1.2901×10^{-6}	7.911	329.5	0.000	0.08
Mars	140.0	0.005	1.8905×10^{-8}	7.070	185.0	0.000	0.00

Table 1976- . **Tropopause Values**

	T K	P mbar	ρ gm/cm^3	H km	V_{sound} m/s	τ_{rad} years	phase °
Earth	217.0	100.000	1.6051×10^{-4}	6.358	295.4	0.043	14.96
Mars	140.0	0.010	3.7809×10^{-8}	7.070	185.0	0.000	0.01

Table 1976- . **1 Bar Values**

	T K	P bar	ρ gm/cm^3	H km	V_{sound} m/s	τ_{rad} years	phase °
Earth	288.0	1.000	1.2094×10^{-3}	8.438	340.3	0.182	48.82
Mars	140.0	0.007	2.6466×10^{-5}	7.070	185.0	0.024	4.59

Table 1976- . **Surface (H_2O) Values**

	T K	P bar	ρ gm/cm^3	H km	V_{sound} m/s	τ_{rad} years	phase °
Earth	288.0	1.013	1.2252×10^{-3}	8.438	340.3	0.184	49.19
Mars	214.0	0.007	1.7314×10^{-5}	10.807	228.7	0.007	1.29

Table 1976- . **Lapse Rate**

Dry Adiabatic: $\Gamma_a \equiv g/C_p$ Autoconvective: $\Gamma_{auto} \equiv g/R_g$

	<g> cm/s^2	C_p J/gm/K	Adiabatic Lapse Rate K/km	R_g J/gm/K	Autoconvective Lapse Rate K/km
Earth	979.86	1.0040	9.760	0.28710	34.130
Mars	374.10	0.8312	4.500	0.18892	19.802

Table 1976- . **Gas Constant**

$\kappa \equiv R_g/C_p$ $\gamma \equiv C_p/C_v$

	<mw> gm/mole	R_{gas} J/gm/K	C_p J/gm/K	κ	γ
Earth	28.96	0.28710	1.0040	0.2860	1.4005
Mars	44.01	0.18892	0.8312	0.2273	1.2941

Table 1976- . **Surface Gravity**

	<g> cm/s^2	<g> g_{earth}	g(0) cm/s^2	g(45) cm/s^2	g(90) cm/s^2
Earth	979.86	1.0000	976.81	981.29	987.16
Mars	374.10	0.3818	372.40	374.90	378.10

Table 1976- . **Gravity Field Spherical Harmonic Coefficients**

	$10^6 \times J2$	$10^6 \times J4$	$10^6 \times J6$	$10^6 \times q$
Earth	1082.63	-2.378	0.006	3449.8
Mars	1960.454			

Table 1976- . **Latitude: planeto-graphic and planeto-centric**

Planeto-centric latitude, θ, and the planeto-graphic latitude, φ

$\beta \equiv R_{eq}/R_{pl}$

$\theta = \tan^{-1} [\tan(\varphi)/\beta^2]$

$\varphi = \tan^{-1} [\tan(\theta) \cdot \beta^2]$

$R(\theta) = R_{eq} R_{pl}/\{[R^2_{eq} \cdot \sin^2(\theta) + R^2_{pl} \cdot \cos^2(\theta)]\}^{1/2}$

$f = (R_{eq} - R_{pl})/R_{eq}$

$e = [R^2_{eq} - R^2_{pl}]^{1/2}/R_{eq} = \{[1 - (R_{pl}/R_{eq})^2]\}^{1/2}$

S = total area = $2 \pi \cdot R^2_{eq} + \pi (R^2_{pl}/e) \cdot \log_e [(1 + e)/(1 - e)]$

V = total volume = $(4/3) \pi R^2_{eq} \cdot Rpl$

If $e = 0$ then

$S = 4 \pi \cdot R_{eq} \cdot R_{eq}$

CRC Standard Mathematical Tables 26th edition, pg. 129. The volume of an oblate sphere is equal to a sphere with radius <R>.

$<R> = (R^2_{eq} \cdot R_{pl})^{(1/3)}$

	R_{eq} km	R_{pl} km	R_{eq}/R_{pl}	f	E	<R> km
Earth	6378.5	6356.0	1.003 540	0.003 527	0.083 920	6370.99
Mars	3393.0	3375.0	1.005 333	0.005 305	0.102 869	3386.99

Table B-2. NASA Planetary Missions to Mars

1965

Mariner 4 : 22 low resolution pictures

1969

Mariner 6 : flyby

1969

Mariner 7 : flyby

1971

Mariner 9 : orbiter (resol. = 0.1 to 1 km)

1976

Vikings : 55 000 images, resol. 150 to 300 meters

Viking 1 orbiter (4 yrs)

Viking 1 lander 22.27N 47.97W

July 20, 1976 4:13 pm LMT

T=250 K

Viking 2 orbiter

Viking 2 lander 47.57N 225.74W

September 3, 1976 9:49 am LMT

T=150 K diurnal variation 35 to 50K

1993

Mars Observer

Mars orbit insertion August 22, 1993 (failed)

1997

Pathfinder lander: 19.17N 33.21W

July 4, 1997 2:58 am LMT

Mars Global Surveyor Insertion September 11, 1997

Mapping orbit February 24, 1999

1999

Mars Climate Orbiter

Mars orbit insertion September 23, 1999 (failed)

Mars Polar lander

December 3, 1999 (failed)

REPORT DOCUMENTATION PAGE	Form Approved OMB No. 0704-0188

1. AGENCY USE ONLY (Leave blank)	2. REPORT DATE March 2001	3. REPORT TYPE AND DATES COVERED Technical Memorandum

4. TITLE AND SUBTITLE Mars Transportation Environment Definition Document	5. FUNDING NUMBERS
6. AUTHOR(S) M. Alexander, Editor	
7. PERFORMING ORGANIZATION NAME(S) AND ADDRESS(ES) George C. Marshall Space Flight Center Marshall Space Flight Center, Alabama 35812	8. PERFORMING ORGANIZATION REPORT NUMBER M-1011
9. SPONSORING / MONITORING AGENCY NAME(S) AND ADDRESS(ES) National Aeronautics and Space Administration Washington, DC 20546	10. SPONSORING / MONITORING AGENCY REPORT NUMBER NASA/TM-2001-210935

11. SUPPLEMENTARY NOTES
Prepared by Engineering Systems Department, Engineering Directorate

12a. DISTRIBUTION / AVAILABILITY STATEMENT Subject Category 18 Unclassified – Unlimited	12b. DISTRIBUTION CODE

13. ABSTRACT (*Maximum 200 words*)

This document provides a compilation of environments knowledge about the planet Mars. Information is divided into three categories: (1) interplanetary space environments (environments required by the technical community to travel to and from Mars), (2) atmospheric environments (environments needed to aerocapture, aerobrake, or use aeroassist for precision trajectories down to the surface), and (3) surface environments (environments needed to have robots or explorers survive and work on the surface).

14. SUBJECT TERMS Mars, space environment, atmospheric environment, surface environment, ionizing radiation, meteoroids, atmospheric density, atmospheric temperature, dust storms	15. NUMBER OF PAGES 114
	16. PRICE CODE A03

17. SECURITY	18. SECURITY CLASSIFICATION OF THIS PAGE	19. SECURITY CLASSIFICATION OF ABSTRACT	20. LIMITATION OF ABSTRACT
Unclassified	Unclassified	Unclassified	Unlimited

APPROVAL

Mars Transportation Environment Definition Document

The information in this report has been reviewed for technical content. Review of any information concerning Department of Defense or nuclear energy activities or programs has been made by the MSFC Security Classifications Officer. This report, in its entirety, has been determined to be unclassified.

_____

Dennis A. Kross
Manager, Engineering Systems Department

_____

Stephen D. Rose
Lead, Environments Group

_____

Gwenevere L. Jasper
Lead, Terrestrial and Planetary Environments Team